

THERMAL RADIATION FROM SOLID PROPELLANT ROCKET MOTOR PLUME

A THESIS SUBMITTED TO  
THE GRADUATE SCHOOL OF NATURAL AND APPLIED SCIENCES  
OF  
MIDDLE EAST TECHNICAL UNIVERSITY

BY

GÜZİDE ÖZEN

IN PARTIAL FULFILLMENT OF THE REQUIREMENTS  
FOR  
THE DEGREE OF DOCTOR OF PHILOSOPHY  
IN  
CHEMICAL ENGINEERING

AUGUST 2015



Approval of the thesis:

**THERMAL RADIATION FROM SOLID PROPELLANT ROCKET MOTOR  
PLUME**

submitted by **GÜZİDE ÖZEN** in partial fulfillment of the requirements for the degree  
of **Doctor of Philosophy in Chemical Engineering Department, Middle East  
Technical University** by,

Prof. Dr. Gülbin Dural Ünver  
Dean, Graduate School of **Natural and Applied Sciences** \_\_\_\_\_

Prof. Dr. Halil Kalıpçılar  
Head of Department, **Chemical Engineering** \_\_\_\_\_

Prof. Dr. Nevin Selçuk  
Supervisor, **Chemical Engineering Dept., METU** \_\_\_\_\_

**Examining Committee Members:**

Prof. Dr. İsmail Hakkı Tuncer  
Aerospace Engineering Dept., METU \_\_\_\_\_

Prof. Dr. Nevin Selçuk  
Chemical Engineering Dept., METU \_\_\_\_\_

Assoc. Prof. Dr. Görkem Külâh  
Chemical Engineering Dept., METU \_\_\_\_\_

Assoc. Prof. Dr. İlker Tarı  
Mechanical Engineering Dept., METU \_\_\_\_\_

Assoc. Prof. Dr. Murat Köksal  
Mechanical Engineering Dept., Hacettepe Uni. \_\_\_\_\_

**Date:** 24.08.2015

**I hereby declare that all information in this document has been obtained and presented in accordance with academic rules and ethical conduct. I also declare that, as required by these rules and conduct, I have fully cited and referenced all material and results that are not original to this work.**

Name, Last name : Güzide ÖZEN

Signature :

## **ABSTRACT**

### **THERMAL RADIATION FROM SOLID PROPELLANT ROCKET MOTOR PLUME**

Özen, Güzide

Ph.D., Department of Chemical Engineering

Supervisor: Prof. Dr. Nevin Selçuk

August 2015, 144 pages

Radiation emitted from rocket plumes plays a significant role in quantifying infrared (IR) radiative signature which is essential for identification and tracking of rockets. Prediction of plume radiation necessitates simultaneous solution of conservation equations for mass, momentum, energy, chemical species and radiant energy to provide input data for the radiation code. This is carried out by a Computational Fluid Dynamics (CFD) solver. As CFD solvers are CPU time expensive, an accurate and CPU efficient solution method of radiative transfer equation (RTE) and a less accurate but CPU efficient radiative property estimation technique are usually employed in these solvers. However, radiation code for prediction of plume radiation necessitates an accurate and CPU efficient solution method of RTE as well as a highly accurate wavelength dependent radiative property estimation technique.

Therefore, predictive accuracy and CPU efficiency of RTE solvers and radiative property estimation techniques were first evaluated by applying the code to different 3-D enclosures containing non-grey, absorbing-emitting-scattering media and benchmarking their predictions against reference solutions and measurements. Comparisons reveal that as RTE solver Discrete Ordinates Method (DOM) for both

CFD solver and radiation code and as radiative property estimation techniques Spectral Line-based Weighted Sum of Grey Gases (SLW) and Statistical Narrow-Band Correlated-k (SNBCK) for CFD solver and radiation code, respectively, satisfy the requirements.

This was followed by running the CFD solver, ANSYS FLUENT v.15.0 with and without radiation in order to see the effect of radiation on the input data provided to the radiation code. CFD solver without radiation was found to be accurate and CPU efficient.

Radiation code based on DOM with SNBCK for gas and Mie Theory for particles was developed to predict plume radiation for non-aluminized and aluminized propellants. For non-aluminized propellant, the prediction accuracy and computational efficiency of radiation code was tested by comparing its predictions with measurements available in the literature. Predictions were found to be in good agreement with measured data. Predictions of spectral radiant intensity under aluminized propellant case were found to be higher than those of non-aluminized propellant due to the use of higher temperature profiles and radiative properties of particles under aluminized propellant case.

Key-words: Plume radiation, Discrete Ordinate Method (DOM), Statistical Narrow-Band Correlated-k (SNBCK)

## ÖZ

### KATI YAKITLI ROKET MOTORLARININ EGZOZ GAZININ TERMİK İŞİNİMİ

Özen, Güzide

Doktora, Kimya Mühendisliği Bölümü

Tez Yöneticisi: Prof. Dr. Nevin Selçuk

Ağustos 2015, 144 sayfa

Roket egzozunun yaydığı ışınım, roketi belirlemek ve takip etmek için kullanılan kızılötesi ışınım imzasında önemli rol oynamaktadır. Işınım koduna girdi verilerini sağlaması için, egzoz ışınım tahminin egzoz için madde, hız, enerji, kimyasal tür ve ışınım enerji korunum denklemlerinin eş zamanlı çözülmesi gerekmektedir. Bu da akışkanlar hesaplamalar dinamiğiyle (CFD) elde edilmektedir. CFD çözücülerde hesaplama zamanının fazla olmasından dolayı, doğruluğu yüksek ve hesaplama zamanı olarak verimli ışınım transfer denkleminin çözüm yöntemi ve doğru az fakat hesaplama zamanı olarak verimli ışınım modeli genelde uygulanmaktadır. Fakat, egzoz ışınım tahmininde kullanılacak ışınım kodu için doğru test edilmiş ve hesaplama zamanı olarak verimli ışınım transfer denkleminin çözüm yöntemi ve yüksek doğrulukta spektral ışınım özellik modeli gerekmektedir.

Bu nedenle, ışınım transfer denkleminin çözüm yöntemleri ve ışınım özellik modelleri farklı üç boyutlu spektral soğurma yayılım saçılım yapan ortamlara uygulanmış ve elde edilen sonuçlar kaynak sonuçlar ve deneysel sonuçlarla karşılaştırılarak sonuçların doğruluğu ve hesaplama verimliliği incelenmiştir. CFD çözücüsü ve ışınım kodu için ışınım transfer denklem çözücüsü olarak Belirli Yönler Yönteminin (DOM) ve ışınım özellik modeli olarak CFD çözücüsü için Spektral Çizgilere Dayalı Gri Gazların

Ağırlıklı Toplamı (SLW) modelinin ve ışınım kodu için İstatiksel Dar Bantlı Bağdaşık-k (SNBCK) modelinin bütün isterleri karşıladığı görülmüştür.

Bu çalışmaya takiben, ışınım koduna sağlanacak girdi verilerinde ışınım etkisini incelemek için CFD çözücüsü, ANSYS FLUENT v.15.0, ışınımlı ve ışınımsız çalıştırılmıştır. Işınımsız çalıştırılan CFD çözücüsünün elde ettiği sonuçlar, doğru ve hesaplama zamanı açısından verimli bulunmuştur.

Alüminyumsuz ve alüminyumlu yakıtların egzoz kızılötesi iz tahmini için DOM ile SNBCK ve Mie teoriye dayalı ışınım kodu geliştirilmiştir. Alüminyumsuz yakıt için elde edilen sonuçlar literatürde yer alan sonuçlarla karşılaştırılarak sonuçların doğruluğu ve hesaplama verimliliği incelenmiştir. Elde edilen sonuçlar, deneysel verilerle uyum içinde bulunmuştur. Alüminyumlu yakıtta kullanılan daha yüksek sıcaklık dağılımından ve parçacıkların ışınım özelliklerinden dolayı alüminyumlu yakıt için elde edilen spektral ışınım şiddeti tahminleri alüminyumsuz yakıtın tahminlerine göre daha yüksek bulunmuştur.

Anahtar Kelimeler: Egzoz ışınımı, Belirli Yönler Yöntemi, İstatiksel Dar Bantlı Bağdaşık-k modeli



To my family

## ACKNOWLEDGMENT

I wish to express my deepest gratitude to my supervisor, Prof. Dr. Nevin SELÇUK for her guidance, advice and encouragement throughout the development of this study.

I am also grateful to Prof. Dr. Faruk ARINÇ and Assoc. Prof. Dr. Görkem KÜLAH for their precious discussions and comments during the progress of this work. I also would like to thank Prof. Dr. İsmail Hakkı TUNCER, Assoc. Prof. Dr. İlker TARI and Assoc. Prof. Dr. Murat KÖKSAL for their valuable suggestions and comments.

ROKETSAN Inc. who supported this work is also gratefully acknowledged.

I also thank to Mine YUMUŞAK, Bora KALPAKLI, Emir Bediğ ACAR, Musa Onur ÖZTÜRKMEN for their support during my study.

I would like to thank to my family Fatma & İsa AYDIN, Zeynep Sevim & Ömer Tanju ÖZEN, Azize AYDIN, Aysun ÖZEN for their support and encouragement.

Finally, my warmest thanks go to my husband, Aykut ÖZEN, and my son, Mehmet Kerem ÖZEN, for their understanding, endless support and encouragement throughout this study.

## TABLE OF CONTENTS

ABSTRACT .....	v
ÖZ .....	VII
ACKNOWLEDGMENT.....	X
TABLE OF CONTENTS .....	XI
LIST OF TABLES .....	XIV
LIST OF FIGURES .....	XVI
LIST OF SYMBOLS .....	XX
CHAPTERS	
1 INTRODUCTION .....	1
1.1 SOLID ROCKET MOTOR .....	2
1.2 ROCKET EXHAUST PLUME.....	4
1.3 PLUME RADIATION.....	5
1.3.1 RTE Solution Techniques .....	6
1.3.2 Radiative Property Estimation for Gases .....	9
1.3.3 Radiative Property Estimation for Al <sub>2</sub> O <sub>3</sub> .....	11
1.3.4 Previous Studies of Plume Radiation for Solid Rocket Motor .....	14
2 RADIATIVE TRANFER EQUATION SOLUTION TECHNIQUES .....	19
2.1 RADIATIVE TRANSFER EQUATION .....	19
2.2 DISCRETE ORDINATES METHOD.....	20
2.2.1 Structure and Operation of the Computer Code DOMSNBCKMIE..	22
2.3 METHOD OF LINES SOLUTION OF DISCRETE ORDINATES METHOD.....	26
2.3.1 Structure and Operation of the Computer Code MOL solution of	

DOM with SNBCK.....	28
2.4 P <sub>1</sub> APPROXIMATION.....	34
2.5 IMPROVED DIFFERENTIAL APPROXIMATION.....	35
2.5.1 Structure and Operation of the Computer Code IDA .....	37
2.6 ANGULAR DISCRETIZATION .....	42
3 ESTIMATION OF RADIATIVE PROPERTIES.....	47
3.1 GREY GAS MODEL .....	47
3.2 SPECTRAL LINE-BASED WEIGHTED SUM OF GREY GASES MODEL.....	48
3.3 STATISTICAL NARROW-BAND CORRELATED-K MODEL.....	49
3.3.1 Structure and Operation of the Computer Code SNBCK .....	52
3.4 MIE THEORY .....	55
3.4.1 Structure and Operation of the Computer Code BHMIE.....	57
4 RESULTS .....	61
4.1 SELECTION OF RTE SOLUTION TECHNIQUE .....	61
4.1.1 Purely Isotropically Scattering Medium and Non-Symmetric Boundary Conditions .....	62
4.1.2 Absorbing-Emitting-Scattering Medium and Non-Symmetric Boundary Conditions .....	64
4.1.3 Absorbing-Emitting-Isotropically Scattering Medium and Symmetric Boundary Conditions.....	65
4.1.4 Purely Linearly Anisotropically Scattering Medium and Symmetric Boundary Conditions.....	69
4.2 SELECTION OF RADIATIVE PROPERTY ESTIMATION TECHNIQUE .....	71
4.2.1 Description of Test Rig.....	71
4.2.2 Treatment of Freeboard.....	75
4.2.3 Comparisons between Model Predictions and Measurements.....	78
4.3 VALIDATION OF ANSYS FLUENT WITH SLW .....	81
4.3.1 Isothermal and Homogenous Medium of H <sub>2</sub> O .....	83

4.3.2 Isothermal and Non-Homogenous Medium of H <sub>2</sub> O .....	86
4.3.3 Isothermal and Homogenous Medium of H <sub>2</sub> O-CO <sub>2</sub> Mixture .....	87
4.4 VALIDATION OF THE RADIATION CODE .....	89
4.4.1 Absorbing-Emitting Gaseous Medium .....	90
4.4.2 Absorbing-Emitting Gaseous / Non-absorbing-Non-emitting- Scattering Particle Medium.....	93
4.5 EXHAUST PLUME SIMULATION FOR NON-ALUMINIZED PROPELLANT CASE...	97
4.5.1 Plume Flow Field .....	99
4.5.2 Plume IR Radiation .....	111
4.6 EXHAUST PLUME SIMULATION FOR ALUMINIZED PROPELLANT CASE.....	115
4.6.1 Plume Flow Field .....	116
4.6.2 Plume IR Radiation .....	121
5 CONCLUSIONS.....	123
5.1 FUTURE WORKS .....	126
REFERENCES.....	127
APPENDICES	
A. ORDINATES AND WEIGHTS FOR S <sub>N</sub> AND T <sub>N</sub> APPROXIMATIONS .....	139
CURRICULUM VITAE .....	143

## LIST OF TABLES

### TABLES

Table 1.1. Previous studies of plume radiation for solid rocket motor.....	16
Table 2.1. Number of ordinates for $S_N$ and $T_N$ quadratures in 3-D systems.....	44
Table 3.1. The 7-point Gauss-Labatto quadrature scheme .....	52
Table 4.1. Average percentage errors in the radiative heat flux predictions along the centerline of the enclosure with CPU times for different angular quadrature schemes...	64
Table 4.2. Average percentage errors in the radiative heat flux predictions along the centerline of a wall with CPU times for different extinction coefficients and uniform grid resolutions.....	68
Table 4.3. Average percentage errors in the radiative heat flux predictions along AB Line, BC Line and CD Line with CPU times for different uniform grid resolutions .....	70
Table 4.4. Operating conditions of the 0.3 MWt ABFBC .....	74
Table 4.5. Polynomials for temperature profiles .....	75
Table 4.6. Radiative properties of fly ash particles in the freeboard .....	77
Table 4.7. Comparison between predicted and measured incident heat fluxes with CPU times for Run 1.....	79
Table 4.8. Comparison between predicted and measured incident heat fluxes with CPU times for Run 2.....	80
Table 4.9. Number of ordinates used for quadratures.....	83
Table 4.10. Absorption coefficients ( $\kappa_j$ ) and their associated weights ( $a_j$ ) obtained from FLUENT and MOL solution of DOM for test case 1 .....	84
Table 4.11. Absorption coefficients ( $\kappa_j$ ) and their associated weights ( $a_j$ ) obtained from FLUENT and MOL solution of DOM for test case 1 .....	85

Table 4.12. Maximum and average absolute percentage errors in the incident heat flux predictions along the centerline ( $x = 2\text{m}$ , $y = 1\text{m}$ , $z$ ) and ( $x$ , $y = 1\text{m}$ , $z=4\text{m}$ ) for test case 2 .....	87
Table 4.13. Absorption coefficients ( $\kappa_j$ ) and their associated weights ( $a_j$ ) obtained from FLUENT and MOL solution of DOM for test case 3 .....	89
Table 4.14. Pressure, temperature and chemical compositions for non-aluminized propellant case [27] .....	98
Table 4.15. Freestream Conditions .....	99
Table 4.16. ANSYS FLUENT solver parameters used in the present study .....	100
Table 4.17. Boundary types used in the present study .....	101
Table 4.18. Chemical reactions with reaction chemistry parameters.....	101
Table 4.19. CPU times for all three runs.....	111
Table 4.20. Average percentage errors in radiant intensity integrated over $1.5\ \mu\text{m}$ - $5.5\ \mu\text{m}$ of wavelength with CPU times for non-aluminized propellant .....	114
Table 4.21. Pressure,temperature and chemical compositions for aluminized propellant case .....	116
Table A.1 Discrete ordinates for the $S_N$ approximation for 3-D geometry.....	140
Table A.2 Discrete ordinates for the $T_4$ approximation for 3-D geometry .....	141

## LIST OF FIGURES

### FIGURES

Figure 1.1. Schematic representation of plume signature.....	2
Figure 1.2. Typical rocket motor [3].....	3
Figure 1.3. Schematic diagrams of a low altitude exhaust plume. Upper sketch displays full plume and lower sketch illustrates the near field of the plume [3] .....	6
Figure 1.4. Real part of complex reflective index for $Al_2O_3$ a) at 300 K, b) at 1773 K, c) 2319 K, d) at 2320 K and e) 3000 K.....	12
Figure 1.5. Imaginary part of complex reflective index for $Al_2O_3$ a) at 300 K, b) at 1773 K, c) 2319 K, d) at 2320 K and e) 3000 K.....	13
Figure 2.1. Flowchart of DOMSNBCKMIE.....	25
Figure 2.2. Algorithm of the subroutine SWEEP .....	26
Figure 2.3. Flowchart of MOL solution of DOM with SNBCK.....	32
Figure 2.4. Algorithm of the subroutine DERV .....	33
Figure 2.5 Flowchart for IDA .....	40
Figure 2.6 Algorithm of the subroutine $P_1$ Approximation .....	41
Figure 2.7 Orders of approximation for $S_N$ .....	42
Figure 2.8. Orders of approximation for $T_4$ (a) Tessellation of basal equilateral triangle (b) sphere triangles [54] .....	43
Figure 2.9. Angular Coordinate System used in ANSYS FLUENT [55].....	45
Figure 3.1. Flowchart of SNBCK .....	54
Figure 3.2. Flowchart of BHMIE.....	59
Figure 4.1. Schematic representation of the system under consideration.....	62
Figure 4.2. Effect of angular discretization on the radiative heat flux predictions along the centerline of the enclosure for DOM and IDA. ....	63



Figure 4.3. Comparison between the radiative heat flux predictions along the centreline of the enclosure for DOM $S_8$ , $P_1$ and IDA $T_4$ .....	65
Figure 4.4. Comparison between the radiative heat flux predictions of DOM $S_8$ , $P_1$ and IDA $T_4$ for different extinction coefficients.....	67
Figure 4.5. Comparison between the radiative heat flux predictions (a) $q_z$ along AB Line (b) $q_x$ along BC Line of DOM $S_8$ and IDA $T_4$ for grid resolution $45 \times 45 \times 45$ . ....	70
Figure 4.6. Particle size distributions for runs with and without recycle.....	74
Figure 4.7. Treatment of freeboard for radiation model .....	77
Figure 4.8. Comparisons between model predictions and measurements results of experimental studies for a) Run 1 and b) Run 2.....	79
Figure 4.9. Comparisons between the source term distribution predictions of GG, SLW, and SNBCK along the centerline of the freeboard for a) Run 1 and b) Run 2 .....	81
Figure 4.10. Comparison between incident heat flux predictions of present study and MOL solution of DOM with SLW and RT with SNB for test case 1 : (a) along ( $x = 2m$ , $y = 1m$ , $z$ ) and (b) along ( $x, y = 1m, z = 4m$ ).....	85
Figure 4.11. Comparison between incident heat flux predictions of present study and MOL solution of DOM with SLW and RT with SNB for test case 1 : (a) along ( $x = 2m$ , $y = 1m, z$ ) and (b) along ( $x, y = 1m, z = 4m$ ).....	86
Figure 4.12. Comparison between incident heat flux predictions of present study and MOL solution of DOM with SLW for test case 3: (a) along ( $x = 2m, y = 1m, z$ ) and (b) along ( $x, y = 1m, z = 4m$ ).....	88
Figure 4.13. Narrowband integrated radiation intensity at $x = 1 m$ , $y = 1 m$ and $z = 7.9 m$ and along the direction of 0.0990147, 0.0990147 and 0.990147 for the isothermal absorbing-emitting case. ....	91
Figure 4.14. Narrowband integrated radiation intensity at $x = 1 m$ , $y = 1 m$ and $z = 7.9 m$ and along the direction of 0.0990147, 0.0990147 and 0.990147 for the non-isothermal absorbing-emitting case. ....	93

Figure 4.15. Narrowband integrated radiation intensity at $x = 1$ m, $y = 1$ m and $z = 7.9$ m and along the direction of 0.0990147, 0.0990147 and 0.990147 for the isothermal absorbing-emitting-scattering case. ....	95
Figure 4.16. Narrowband integrated radiation intensity at $x = 1$ m, $y = 1$ m and $z = 7.9$ m and along the direction of 0.0990147, 0.0990147 and 0.990147 for the non-isothermal absorbing-emitting-scattering case. ....	97
Figure 4.17. Grid resolution used in non-aluminized/aluminized propellant cases.....	100
Figure 4.18. Profiles along centerline from nozzle exit for non-aluminized propellant case (a) temperature (b) axial velocity (c) Mach number (d) H <sub>2</sub> O mole fraction (e) CO <sub>2</sub> mole fraction (f) CO mole fraction .....	103
Figure 4.19. Radial temperature profile at 0.1 m from nozzle exit ( $z = 0.1$ m) and 0.6 m from nozzle exit ( $z = 0.6$ m) non-aluminized propellant case .....	104
Figure 4.20. Radial axial velocity profile along centerline at 0.1 m from nozzle exit ( $z = 0.1$ m) and 0.6 m from nozzle exit ( $z = 0.6$ m) non-aluminized propellant case.....	104
Figure 4.21. Radial Mach number profile along centerline at 0.1 m from nozzle exit ( $z = 0.1$ m) and 0.6 m from nozzle exit ( $z = 0.6$ m) non-aluminized propellant case .....	105
Figure 4.22. Radial H <sub>2</sub> O mole fraction profile along centerline at 0.1 m from nozzle exit ( $z = 0.1$ m) and 0.6 m from nozzle exit ( $z = 0.6$ m) non-aluminized propellant case....	105
Figure 4.23. Radial CO <sub>2</sub> mole fraction profile along centerline at 0.1 m from nozzle exit ( $z = 0.1$ m) and 0.6 m from nozzle exit ( $z = 0.6$ m) non-aluminized propellant case....	106
Figure 4.24. Temperature field of plume non-aluminized propellant case (a) without radiation (b) with grey WSGG (c) with SLW.....	107
Figure 4.25. H <sub>2</sub> O mole fraction field of plume non-aluminized propellant case (a) without radiation (b) with grey WSGG (c) with SLW .....	108
Figure 4.26. CO <sub>2</sub> mole fraction field of plume non-aluminized propellant case (a) without radiation (b) with grey WSGG (c) with SLW .....	109
Figure 4.27. CO mole fraction field of plume non-aluminized propellant case (a) without radiation (b) with grey WSGG (c) with SLW .....	110

Figure 4.28. Source spectral radiant intensity for H<sub>2</sub>O-CO<sub>2</sub>-CO mixture and H<sub>2</sub>O-CO<sub>2</sub> mixture under non-aluminized propellant case ..... 112

Figure 4.29. Source spectral radiant intensity for different angular quadrature and grid discretizations under non-aluminized propellant case ..... 113

Figure 4.30. Source and apparent spectral radiant intensities for non-aluminized propellant case..... 115

Figure 4.31. Profiles along centerline from nozzle exit for non-aluminized and aluminized propellant cases (a) temperature (b) axial velocity (c) Mach number (d) H<sub>2</sub>O mole fraction (e) CO<sub>2</sub> mole fraction (f) CO mole fraction..... 118

Figure 4.32. Temperature field of plume for aluminized propellant case..... 119

Figure 4.33. H<sub>2</sub>O mole fraction field of plume for aluminized propellant case..... 119

Figure 4.34. CO<sub>2</sub> mole fraction field of plume for aluminized propellant case..... 120

Figure 4.35. CO mole fraction field of plume for aluminized propellant case ..... 120

Figure 4.36. Al<sub>2</sub>O<sub>3</sub> concentration field of plume for aluminized propellant case..... 121

Figure 4.37. Source spectral radiant intensity for non-aluminized and aluminized propellant cases ..... 122

## LIST OF SYMBOLS

$a$	radius of the spherical particle
$a$	grey gas weights
$a_n$	Mie scattering coefficient
$A_1$	coefficient of linear anisotropy of scattering (-)
$b_n$	Mie scattering coefficient
$C$	cross-section
$D$	Logarithmic derivative
$D$	diameter of particle
$f$	function
$G$	incident radiation ( $\text{Wm}^{-2}$ )
$g$	cumulative function
$g$	asymmetry factor
$I_b$	blackbody intensity ( $\text{Wm}^{-2}\text{sr}^{-1}$ )
$I$	radiative intensity ( $\text{Wm}^{-2}\text{sr}^{-1}$ )
$J$	radiosity ( $\text{Wm}^{-2}$ )
$k$	$k$ -distribution
$k$	time constant
$k$	imaginary part of complex refractive index (-)
$L$	length (m)
$L_0$	dimension of enclosure (m)

M	Mach number
M	total number of ordinates (-)
m	complex refractive index (-)
m	mass distribution function ( $\text{kg}/\text{m}^3\mu\text{m}$ )
n	real part of complex refractive index (-)
<b>n</b>	unit surface normal (-)
N	molar density, ( $\text{mol}/\text{m}^3$ )
N	number of quadrature (-)
p	pressure (atm)
<b>q</b>	radiative heat flux ( $\text{Wm}^{-2}$ )
Q*	dimensionless radiative heat flux
R	radius of the circular region
r	distance from the plume centerline
<b>r</b>	position in the medium (m)
S	source term ( $\text{Wm}^{-3}\text{sr}^{-1}$ )
T	temperature (K)
x	co-ordinate axis in rectangular geometry (-)
w	quadrature weight (-)
y	co-ordinate axis in rectangular geometry (-)
z	co-ordinate axis in rectangular geometry (-)
<i>x</i>	size parameter
X	mole fraction
$\beta$	extinction coefficient ( $\text{m}^{-1}$ )

$\gamma$	specific heat ratio
$\bar{\gamma}$	mean collision half-width
$\bar{\delta}_v$	equivalent line spacing
$\varepsilon$	emissivity
$\varepsilon$	time step size
$\epsilon$	error tolerance (-)
$\Phi$	scattering phase function ( $\text{sr}^{-1}$ )
$\theta$	polar angle (rad)
$\phi$	azimuthal angle (rad)
$\emptyset$	radiative quantity (-)
$\eta$	direction cosine in y (-)
$\kappa$	absorption coefficient ( $\text{m}^{-1}$ )
$\mu$	direction cosine in x (-)
$\xi$	direction cosine in z (-)
$\xi$	Ricatti-Bessel functions (-)
$\psi$	Ricatti-Bessel functions (-)
$\sigma$	Stefan-Boltzmann constant (-)
$\sigma_s$	scattering coefficients ( $\text{m}^{-1}$ )
$\lambda$	wavelength
$\tau$	optical thickness (-)
$\tau$	gas transmissivity (-)
$\omega$	single scattering albedo (-)

$\Omega$  solid angle

$\Omega$  direction

Subscripts:

abs absorption

c centerline

c carbondioxide

e exit

ext extinction

*g* gas

HG Henvey-Greenstein function

i quadrature point

j grey gas for H<sub>2</sub>O

k grey gas for CO<sub>2</sub>

m mean

max maximum

med medium

p particle

s reference case

t time

sca scattering

w wall

w watervapor

z co-ordinate axis in rectangular geometry (-)

$\nu$  wavenumber ( $\text{cm}^{-1}$ )

Superscripts:

m ordinate index

m' incoming ordinate

\* property computed from  $P_1$

Abbreviations:

ABFCBC Atmospheric Bubbling Fluidized Bed Combustor

AP Ammonium Perchlorate

BET Brunauer, Emmet, Teller Method

CCS Carbon Capture and Storage

CFD Computational Fluid Dynamics

CKFG Correlated-k including Fictitious Gas

CKFG-SMG Correlated-k including Fictitious Gas Single Mixture Gas

CK-SMG Correlated-k Single Mixture Gas

DOM Discrete Ordinates Method

DTM Discrete Transfer Method

EWB Exponential Wide Band

FSK Full-Spectrum k-distribution

IDA Improved Differential Approximation



IDA T <sub>4</sub>	Improved Differential Approximation with T <sub>4</sub> Quadrature
IR	Infrared
HTPB	Hydroxyl-terminated polybutadiene
GG	Grey Gas
LBL	Line-by-line
RTE	Radiative Transfer Equation
MC	Monte Carlo
MDA	Modified Differential Approximation
MOL	Method of Lines
ODA	Ordinary Differential Approximation
ODE	Ordinary Differential Equation
PDE	Partial Differential Equation
RT	Ray Tracing
RITE	Radiative Integral Transfer Equation
SHDOM	Spherical Harmonics Discrete Ordinate Method
SIRRM	Standardized Infrared Radiation Model
SLW	Spectral Line-based Weighted Sum of Grey Gases
SMG	Single Mixture Gas
SNB	Statistical Narrow Band
SNBCK	Statistical Narrow-Band Correlated-k
SRM	Solid Rocket Motor
UDF	User Defined Function
WSGG	Weighted-Sum-of-Grey-Gases



## CHAPTER 1

### INTRODUCTION

Propellant of a solid rocket motor (SRM) consists of the fuel and oxidizer together and cast into a solid material. Solid Propellant developed by the Chinese was used in the rockets over 800 years ago. Military bombardment rockets were utilized in the eighteenth and nineteenth centuries. Nowadays, solid rockets are frequently used on ballistic missiles, space launchers and tactical missiles.

Although solid rockets are less powerful and efficient than liquid rockets, they are generally produced straightforwardly and safer to store. Aluminum powder is added into the fuel and oxidizer mixture which is one of common technique for enhancement of the solid rocket performance. SRM composite propellants generally consist of up to 20 % of aluminum in mass. Aluminum in propellants stabilizes the combustion process due to the micron-size of aluminum particles and raises the rocket specific impulse due to increasing temperature of the combustion chamber. The drawbacks of using aluminum in the propellant are overheating the rocket base due to hot alumina particles in exhaust plume and negative effect on the missile detection due to increasing infrared plume signature [1].

Aluminized SRM necessitates the evaluation of the infrared radiation signature due to radiative heat transfer inside the plume and through the atmosphere and received by a distant sensor for determination of the detecting performance (Figure 1.1). Plume properties of rocket are firstly computed by solving governing equations of mass, momentum, energy, chemical species and radiant energy. Then the RTE is solved in the exhaust plume which is non-homogenous absorbing-emitting-scattering medium and throughout the atmosphere up to the sensor. The spectral resolution must be as small as

$5 \text{ cm}^{-1}$  in order to select the optimal spectral band to maximize the detection probability [1].

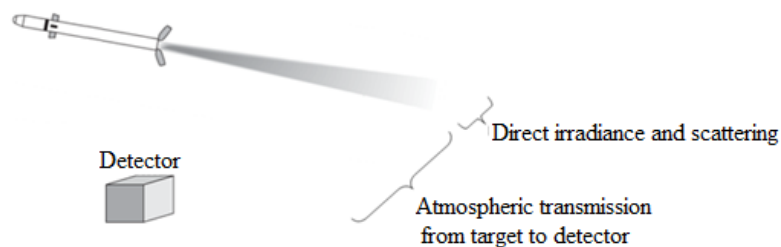


Figure 1.1. Schematic representation of plume signature

## 1.1 Solid Rocket Motor

The solid rocket motor (Figure 1.2) is designed to ensure the combustion under pressure in the combustion chamber. The resulting gases are expanded through the nozzle, whose function is to convert this pressure into supersonic exhaust [2].

Rocket motor is made of five major components:

### *The case*

The case is made either from metal (high-resistance steels) or composite materials produced by filament winding (glass, carbon). It has resistance to the internal pressure, approximately 3-25 MPa, with a sufficient safety coefficient, usually of the order of 1.4 [2].

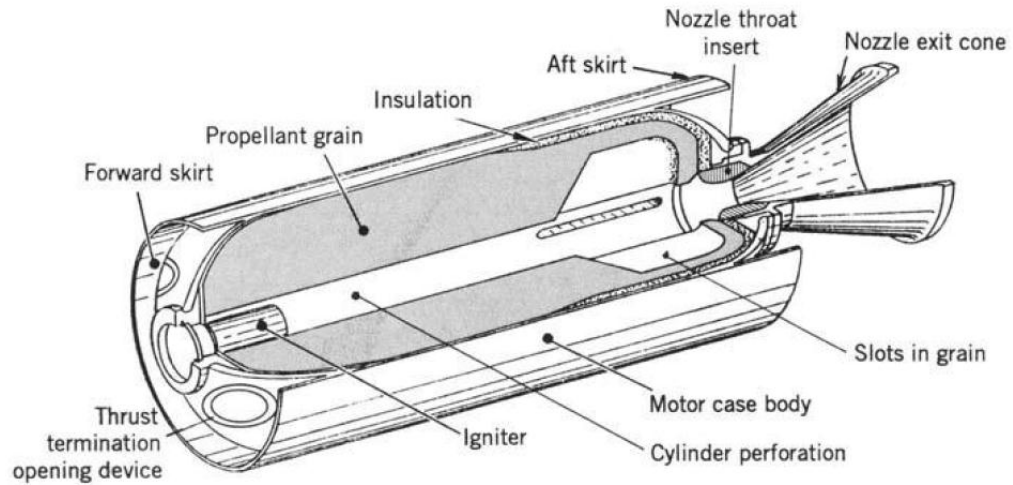


Figure 1.2. Typical rocket motor [3]

### ***Propellant and Its Grain***

The composite propellants have been used as propellant in the past three decades. They are a heterogeneous propellant grain containing oxidizer crystals (i.e. ammonium perchlorate, AP) and powdered fuel (usually aluminum) and binder (i.e. hydroxyl-terminated polybutadiene, HTPB). Conventional composite propellants commonly include 60-72 % AP, up to 22% Al and 8-16 % of elastomeric binder. Moreover, geometrical configuration of the grain which is the shaped mass of processed solid propellant inside the rocket motor affects the characteristics of the motor performance. The propellant grain is a cast, molded or extruded body. When it is ignited, it will burn on all exposed surfaces to produce hot gases which are exhausted through a nozzle [3].

### ***Thermal Insulation***

Inside surface of the case needs protection against the combustion temperature of propellant grains, ranging from 1500 to 3500 K. Materials of insulation may be made of asbestos, silicate and carbon fibers impregnated with heat-proof resin [2].

### ***The Ignition System***

The ignition system brings necessary energy to the surface of the propellant to start burning. There are three stages: initiator (transforming ignition signal into a booster charge), booster charge (transferring the flame from the primer to the main charge) and main charge (igniting the grain of the solid propellant) [2].

### ***The Nozzle***

The nozzle is used to accelerate the hot exhaust gases. It is usually made from graphite and/or an ablative material to absorb the heat and withstand to high temperature and erosion. The shape and complexity of a nozzle depends on the expected level of performance and the field of application of the rocket motor [2].

### **1.2 Rocket Exhaust Plume**

The plume is defined as the moving formation of hot gases and small particles exiting from the rocket nozzle. The plume has non-uniform structure with different flow regions and supersonic shock waves, velocity or concentration. It seems to be as a brilliant flame. Moreover, plumes leave smoke or vapor or toxic exhaust gases [3].

The plume characteristics are subject to the characteristics of the rocket propulsion system with its propellants, the flight conditions, the weather conditions and the configuration of vehicle. Figure 1.3 illustrates plume flow field at a low-altitude (3-10 km). The diameter and length of plume are numerous times larger than those of the rocket. Near field of plume consists of an in-viscid inner core where exhaust gases have not yet mixed with air and an outer mixing layer where the species in the plume reacts with oxygen in the mixing layer. Intensities of the shock wave reduce and most abundant of the plume is mixed with ambient air in the intermediate field of plume. The hot gases are mixed with ambient air and local pressure is nearly the same as that of the air in the far field of plume. All three parts of the plume emit radiation, only near field of the plume interacts with the rocket.

Afterburning or secondary combustion takes place in the mixing layer where exhaust gases are mixed with the air. Mixing layer is a turbulent layer surrounding the core and its thickness increases with distance from the nozzle as well as with altitude.  $H_2$ , CO, NO, or  $C+H_2$  species in the plume which are incompletely oxidized fuel species burn with oxygen in the mixing layer and are converted to  $H_2O$ ,  $CO_2$ , or  $NO_2$ . The temperature and specific volume increases in this region due to combustion.

Particles in the plume influence the plume flow field by transferring mass, momentum and energy between the particle and gas phases. Compared to the gas phase, particles are either solid or liquid in form, have different temperature and velocities to those of gas phase where plume contains large gradients such as near to nozzle or through shocks. The effect of the particles on the turbulence in the gas phase due to velocity gradients is important as it influences mixing layer. [4].

### **1.3 Plume Radiation**

To prevent rocket from detection and recognition, plume radiation becomes important. Exhaust plume emits radiation in wide range of spectrum (infrared, 700 nm-14  $\mu m$ , visible, 400 nm-700 nm, and ultraviolet, 100 nm-400 nm ) [4].

The main radiation emissions from the exhaust gases are in the infrared region of spectrum [3]. Effects of  $CO_2$  and  $H_2O$  molecules on the infrared signature are dominant compared to that of CO, HCl, HF and  $N_2O$  species. Particles in the plume influence radiation in the infrared spectrum and particles dominate radiation emission in the long wave region (8-14  $\mu m$ ) where gas emissions are low.

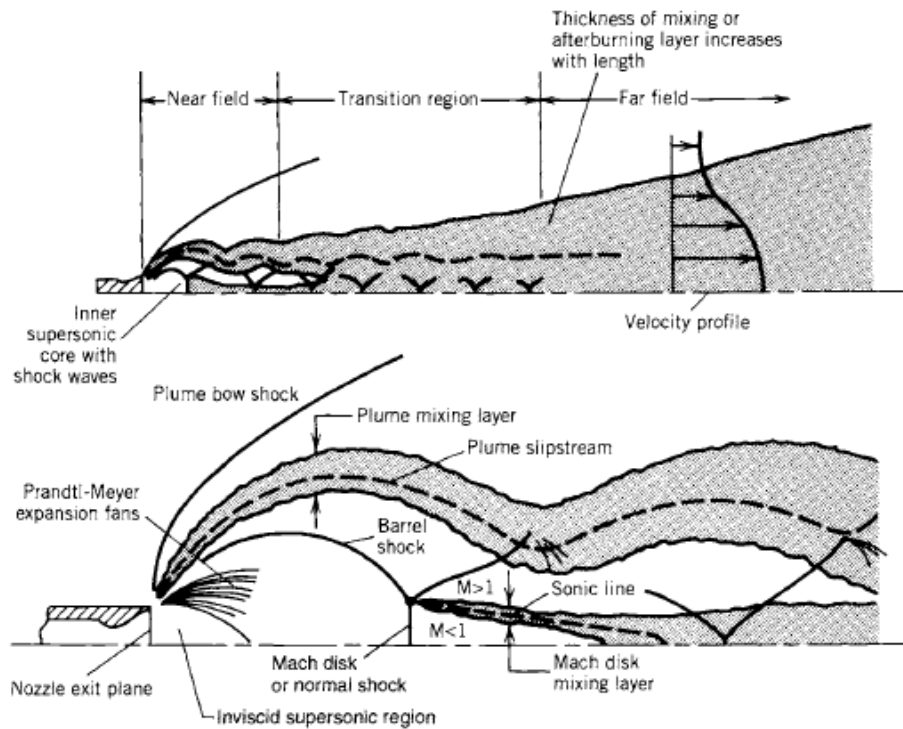


Figure 1.3. Schematic diagrams of a low altitude exhaust plume. Upper sketch displays full plume and lower sketch illustrates the near field of the plume [3]

In this section, RTE solution techniques, radiative property estimation methods for gases and for  $\text{Al}_2\text{O}_3$  particles in plume used to calculate plume radiation are described and previous studies of plume radiation for solid rocket motor are summarized.

### 1.3.1 RTE Solution Techniques

The mathematical formulation of the radiation field at a point within a plume is achieved by considering radiative transfer through a very small volume of gas in a specified direction. As the ray in the chosen direction travels through the volume element, the intensity of radiation is attenuated by absorption in the intervening medium or by scattering away from the specified direction and is enhanced by emission or by scattering into the direction of travel. The radiant energy balance on the gas volume results in an integro-differential equation for the intensity of radiation in the chosen



direction. The complete description of the radiative transfer in a small volume is obtained when the corresponding procedure is applied for each possible direction of travel of rays.

For the bounding surfaces, the radiative exchange at a point along a specified direction is formulated by a radiant energy balance which equates the radiation leaving the point to the sum of emission due to temperature of the surface and radiation reflected along the chosen direction. The procedure is repeated for all possible directions of travel of rays within the solid angle of  $2\pi$  steradians surrounding the point.

When evaluating the radiation transfer at a point, whether within the plume or on the surface, the amount of energy arriving is difficult to determine, as the intensity of arriving radiation is influenced by the geometry and the properties of the bounding surfaces and the radiating medium within the enclosure. The problem of describing the radiation field is further complicated when it is considered that energy is distributed over wide range of wavelength and the surfaces and particle laden gases in a plume generally have radiative properties which are dependent on the wavelength.

The mathematical difficulties in obtaining solutions of the equation of transfer have led to a number of approximations. The Hottel's zone method and Monte Carlo (MC) technique have long been accepted as the most accurate methods. However, these traditional methods have not been extensively used as part of a comprehensive combustion model due to their large computational time and storage requirements. The reason for this is that the equations modeling the radiation field are not in differential form and hence are not well suited to solution simultaneously with the differential equations for flow, reaction and energy. In order to overcome this disadvantage, flux models have been widely employed as alternative, but less accurate models in combustion systems [5]. In the two-flux model, the solid angle surrounding a point is divided into two hemisphere in the positive and negative co-ordinate direction chosen whereas in the six-flux model, two more orthogonal directions are added to two fluxes.

Flux models of radiation fields take the form of partial differential equations which are amenable to solution simultaneously and conveniently with equations governing the transport of mass, momentum, species and energy [6, 7]. Discrete Transfer Method (DTM) is a hybrid method for solution of RTE. This method combines certain features of Hottel's zone, MC and flux-type models. In DTM, rays are represented as traveling through the considered domain in selected directions. Comparisons between predictions of DTM and DOM show that DOM provide more accurate and accurate and CPU efficient solutions [5].

Another solution method of RTE is Spherical Harmonics method ( $P_N$ ) and its variations. This method represents angular variation of intensity at a point by a series of spherical harmonics. The lowest order spherical harmonics method,  $P_1$ , benchmarked against exact solutions [8] in an axisymmetrical cylindrical furnace containing absorbing-emitting medium, was found to underpredict the wall heat fluxes. It was also found inaccurate when tested against benchmark solutions in an optically thin absorbing-emitting-scattering medium of a cold cylinder test problem [9]. This shortcoming has been alleviated by modifying  $P_1$  to yield modified differential approximation (MDA) [9] and improved differential approximation (IDA) [10] methods. Modest [10] investigated the predictive accuracy and computational efficiency of MDA and IDA by applying both methods to multidimensional absorbing-emitting-scattering media and comparing their predictions with MC solutions. Both methods were found to give higher accuracy with IDA providing higher CPU efficiency [10]. Recently, in an attempt to increase the computational efficiency, both MDA and IDA with  $T_4$  quadrature were applied to an absorbing-emitting-scattering medium in a cubic enclosure [11]. Comparison of CPU times of MDA, IDA and MDA, IDA with  $T_4$  quadrature reveals that application of  $T_4$  quadrature to MDA and IDA decreases the CPU times considerably with IDA  $T_4$  yielding higher accuracy [11].

Over the two past decades, DOM has been the most widely used technique for obtaining numerical solutions to RTE for multi-dimensional enclosures containing absorbing,

emitting and scattering media [12, 13]. The DOM is conceptually an extension of flux methods [6-8], which converts integro-differential equation into partial differential equations by discretization of angular variation of radiative intensity. It corrects shortcomings of flux methods by solving the exact RTE for a set of discrete directions spanning the total solid angle of  $4\pi$ . The method has been tested for accuracy in 1-D [12, 14, 15], 2-D [16-17] and 3-D [12, 13, 18, 19] radiative heat transfer problems by comparing its predictions with benchmark solutions and found to be an accurate and computationally efficient method.

Evans [20] developed the spherical harmonics discrete ordinate method (SHDOM), in which spherical harmonics are employed for computing the source function including the scattering integral and discrete ordinate method is used to integrate RTE spatially, and applied this model to multi-dimensional media for atmospheric radiation and found SHDOM to produce accurate and CPU efficient predictions [20,21].

Finite Volume Method (FVM) is another widely used model to solve RTE equation. The angular and spatial domains are divided into a finite number of control angles and control volumes in this method. Assumption of the method is that the magnitude of intensity taken as constant within a control volume, a control angle and control-volume surface but the direction of intensity varies within a control angle. FVM is found to provide less accurate solution in optically thin medium. [22]

### **1.3.2 Radiative Property Estimation for Gases**

The absorption coefficient or the absorption cross-section which is normalized absorption coefficient according to the molar density is the main radiative property of the gases [23]. Absorption coefficient of a gas varies as a function of wavenumber and this is defined as spectrum. Spectrum contains millions of spectral lines formed by the vibrational and rotational transitions in energy level of molecules. Modeling of absorption coefficient is a formidable task due to fact that it strongly depends on wavenumber. Several methods have been developed to estimate the radiative properties

of participating gases. The most accurate radiative estimation technique is Line-by-line (LBL) model [24] which necessitates evaluation of absorption coefficient for millions of vibrational and rotational lines and its computational cost is extremely high. Therefore, LBL model is not suitable for engineering applications. Band models estimate nongrey radiative properties over wavenumber intervals by assuming radiative properties as a constant in each interval. Band models categorized as wide band and narrow band models according to the width of wavenumber intervals. As far as spectrally integrated quantities are concerned, wide band models such as WSGG, SLW and exponential wide band (EWB) models lead to more accurate and computationally efficient results. However, they cannot be utilized to evaluate radiative properties for plume signature application due to fact that these models provide total quantities instead of spectral intensities at low resolution (5–25  $\text{cm}^{-1}$  bandwidth) [25].

Narrow band models such as Elsasser narrow band model [26], narrowband statistical band model (SNB) [27,28], Malkus narrow band [1], the exponential-tailed 1/S random band model [29] have found wider application for the radiative property estimation for hot gas mixture in the plume. Disadvantage of these models is that they provide gas transmissivities as a radiative property instead of absorption coefficients which is necessary to solve RTE. The SNBCK model provides absorption coefficients from band-averaged gas transmissivity by utilizing inverse Laplace transformation and its advantage is that this model is directly applied to accurate and efficient RTE solution technique, DOM. Moreover, Caliot and coworkers [30] evaluated the accuracy of CKFG (correlated-k including fictitious gas), CKFG-SMG (single mixture gas) and CK-SMG models in the remote sensing of a high temperature plume at sea level and at high altitude in the spectral intervals of 2000-2500  $\text{cm}^{-1}$ , 3450-3850  $\text{cm}^{-1}$ , 3850-4150  $\text{cm}^{-1}$  and found that CKFG and CKFG-SMG have identical accuracies in remote sensing application except in the spectral interval of 3450-3850  $\text{cm}^{-1}$  for the high altitude where CKFG gives better results. Following section reviews the studies on radiative property estimation for  $\text{Al}_2\text{O}_3$ .

### 1.3.3 Radiative Property Estimation for Al<sub>2</sub>O<sub>3</sub>

Radiation of Al<sub>2</sub>O<sub>3</sub> particles plays a significant role in the infrared radiation of solid rocket plume. Pseudo-gas approximation was firstly utilized to determine the effects of the particles on the plume radiation. In this approximation, it assumed that the particles are small compared to the wavelength range and they absorb and emit only [31]. However, Al<sub>2</sub>O<sub>3</sub> particles produce multiple scattering effects and therefore, scattering-analysis for signature prediction is required.

Radiative properties of particles are generally calculated by using the Mie theory for spheres with specified size and complex refractive index given by  $m = n - ik$  [26]. The real part of the refractive index  $n$  indicates the refractive properties of material, while the imaginary part  $k$  indicates absorptive properties of material. Although the Mie theory is based on the idealization of homogenous spherical particles, it can be considered as very reasonable first approximation since real plume particles were often found to be solid sphere [32]. The real and imaginary parts of refractive index are obtained from experiments [33]. In this section, complex refractive indexes for Al<sub>2</sub>O<sub>3</sub> particles as functions of wavelength and temperature reported in the literature are summarized.

The real part of the index of refraction for Al<sub>2</sub>O<sub>3</sub> particles as function of wavelength at 300 K, 1773K, 2319 K, 2320 K and 3000 K are illustrated in Figure 1.4. As can be seen from the figure, the data are in good agreement with each other. Moreover, temperature dependency of the data is insignificant.

The imaginary part of the index of refraction for Al<sub>2</sub>O<sub>3</sub> particles as function of wavelength at 300 K, 1773K, 2319 K, 2320 K and 3000 K are shown in Figure 1.5. As can be seen from the figure, the imaginary part varies from  $10^{-9}$  to 1. The scatter between different results can be explained by crystalline phase of alumina and the presence of impurities [26, 33, 34, 35].

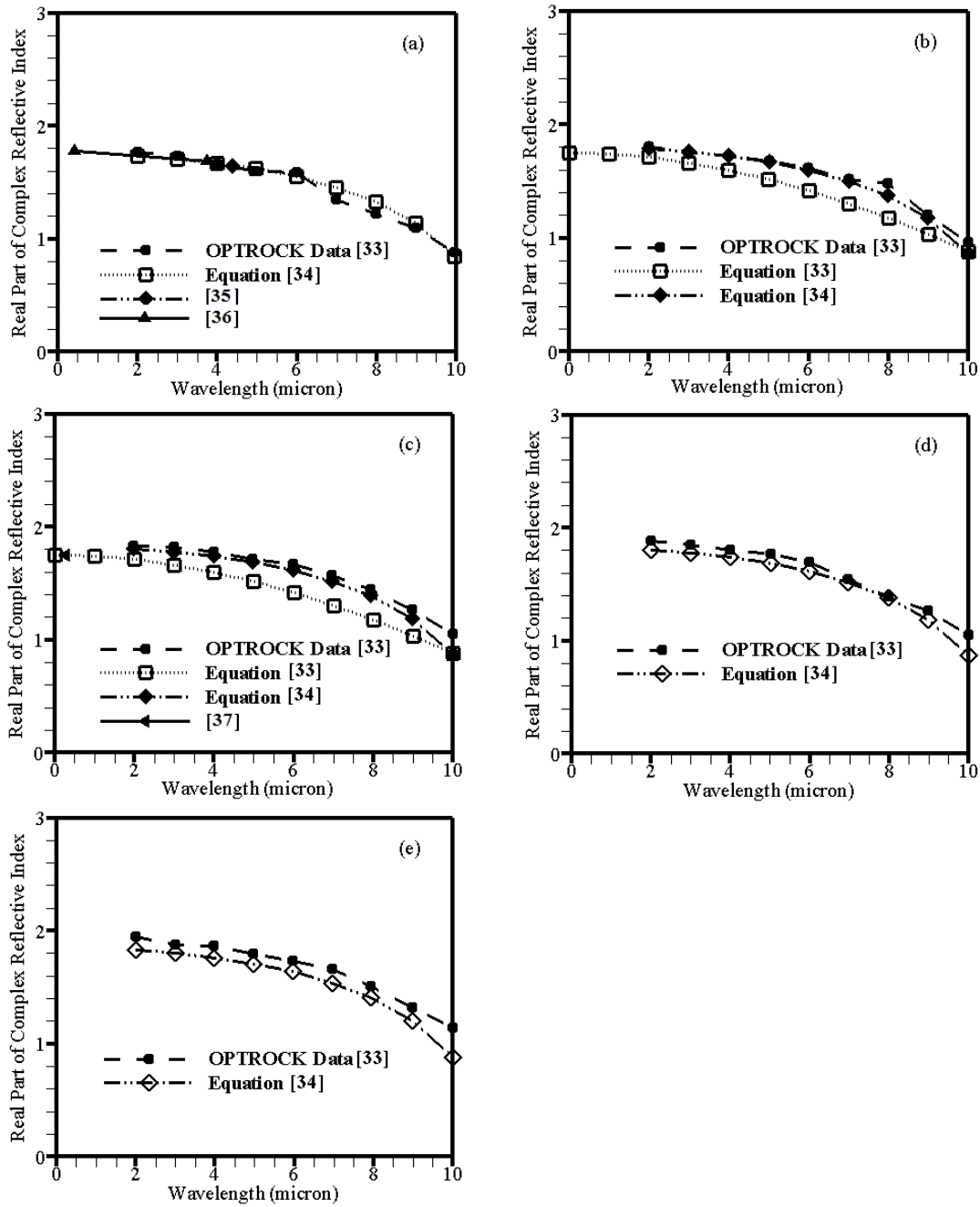


Figure 1.4. Real part of complex reflective index for  $\text{Al}_2\text{O}_3$  a) at 300 K, b) at 1773 K, c) 2319 K, d) at 2320 K and e) 3000 K.

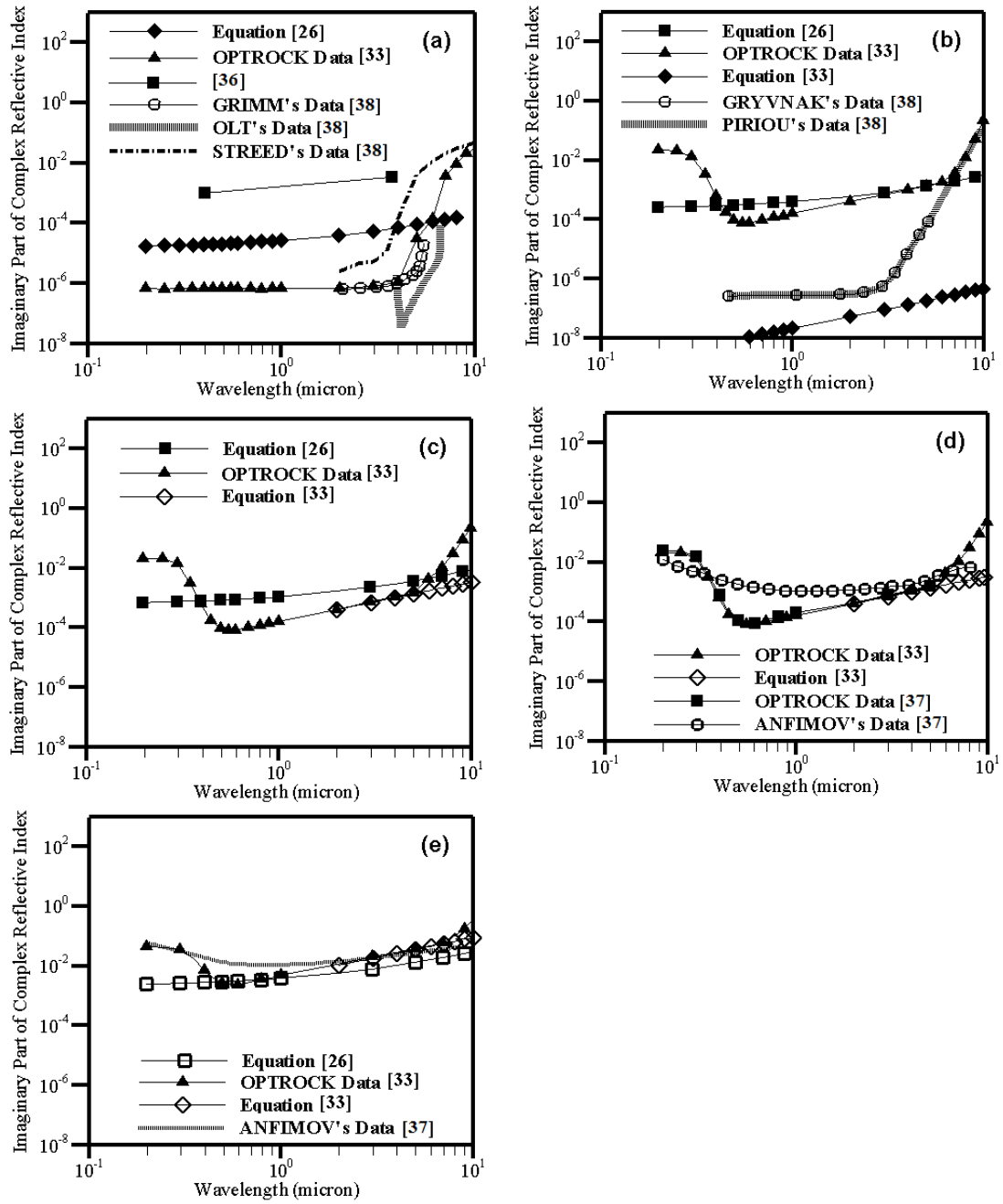


Figure 1.5. Imaginary part of complex reflective index for  $\text{Al}_2\text{O}_3$  a) at 300 K, b) at 1773 K, c) 2319 K, d) at 2320 K and e) 3000 K.

### 1.3.4 Previous Studies of Plume Radiation for Solid Rocket Motor

Table 1.1 summarizes previous studies of plume radiation for solid rocket motor. As can be seen from Table 1.1, plume radiation dominates the infrared signature and its most accurate and CPU efficient predictions necessitate testing of most recently available RTE solution methods and radiative property estimation techniques which is not available in the open literature to date. In addition, the literature reveals that  $\text{Al}_2\text{O}_3$  particles have significant effect on plume radiation.

Therefore, the principal objective of this study has been to develop a radiation code for determining the plume radiation of aluminized solid propellant. In the course of the development of the radiation code, following stages have been followed:

- Investigating the predictive accuracy and computational efficiency of DOM,  $P_1$  and IDA by applying the methods to four cubical test problems and comparing their predictions with benchmark solutions available in the literature to select RTE solution technique for CFD solver (ANSYS FLUENT) and the radiation code.
- Testing the predictive accuracy and computational efficiency of MOL of DOM coupled with different radiative property estimation techniques (GG, SLW, SNBCK models) by applying them to the prediction of incident radiative fluxes along the freeboard walls of a 0.3 MWt ABFBC and comparing their predictions with measurements generated previously from two runs one without and the other with recycle to select radiative property estimation technique for CFD solver and the radiation code.
- Implementation of SLW to ANSYS FLUENT as radiative property estimation technique for gas.
- Development of radiation code based on DOM with SNBCK and Mie Theory for selection of radiative property estimation technique for radiation code, and



validation of the predictions of the code against reference solutions available in the literature.

- Evaluation of plume field for non-aluminized/aluminized solid propellant rocket motors to provide input data for radiation code by using ANSYS FLUENT with and without radiation.
- Calculation of plume radiation by using DOM with SNBCK and Mie Theory for non-aluminized/aluminized solid propellant rocket motors.
- Validation of predictions of the radiation code for non-aluminized propellant against experimental data available in the literature.

Table 1.1. Previous studies of plume radiation for solid rocket motor

Authors	RTE Solver	Radiative property estimation techniques	Comments
Freeman et al. [32]	Six-flux model	Narrow bands for gases and Mie theory for $Al_2O_3$ with wavelength dependent complex reflective index	Accuracy of six-flux model was examined on 2-D test problem by using benchmark solution obtained from MC method which has a reputation as being rather slow for results with good accuracy. A comparison between the forward scattered radiance predicted by the six-flux model and MC method showed agreement within 20%.
Ludwig et al. [39]	Two-flux model Six-flux model	Statistical (Goody) model for gases	Predictions were compared with laboratory data. It was found that two-flux under-predicts the measured data whereas six-flux over-predicts the measured data.
Nelson [29]	Six-flux model	Narrow bands for gases and Mie theory for $Al_2O_3$	The plumes were taken as isothermal cylinders with uniform gas and $Al_2O_3$ concentrations representative of liquid rocket plume and three different kinds of solid rocket plumes. It was found that plume signatures containing $Al_2O_3$ particles are sensitive to the particle size and particle loading.
Farmer et al. [33]	$P_1$ ODA IDA	EWB model for gases Mie theory for $Al_2O_3$ with wavelength dependent complex reflective index	Predicted heat fluxes were compared with measurements. Comparisons show that $P_1$ approximation tends to underestimate the heat flux measurements in the near field of the plume and IDA results generally overestimate the data.

Table.1.1.1. Previous studies of plume radiation for solid rocket motor (cont'd)

Authors	RTE Solver	Radiative property estimation techniques	Comments
Liu et al. [25]	Radiance Splitting Method based on DOM	SNB and Mie theory for $Al_2O_3$ with constant complex reflective index	Representative plume containing isothermal/non-isothermal absorbing-emitting/absorbing-scattering medium were utilized and predictions obtained from the models were compared with those of DOM with SNBCK. Comparison revealed that the splitting method provides accurate solutions for isothermal case and non-isothermal with low to intermediate particle loading and is found to be inaccurate for non-isothermal with high particle loading.
Avital et al. [27]		SNB with wavenumber interval of $20\text{ cm}^{-1}$ for gases	Predictions were compared with the experimental data for non-aluminized solid rocket plume and calculated radiance was found to be in reasonable agreement with the measured radiance.
Boisichot et al. [28]	SHDOM	SNB for gases and Mie theory for $Al_2O_3$ with wavelength dependent complex reflective index	Predictions of intensity were compared with those obtained from measured data with spectrophotometers and the camera and it was found that SHDOM model leads to underestimation in the radiance along the plume axis for both 3.3-3.6 $\mu\text{m}$ and 4.5-4.9 $\mu\text{m}$ spectral bands.
Cai et al. [26]	FVM	Elsasser narrow band model for gases and Mie theory for $Al_2O_3$ with wavelength dependent complex reflective index	Radiative signatures of liquid and solid rocket plumes were investigated. Atmospheric absorption effect was also taken into account by using MODTRAN. Some of their findings were compared with those available in the literature and were found to be in good agreement in most cases. Effect of particles in solid rocket plume was also investigated and it was found that particle emission increase plume radiation and particle scattering increase plume radiation more than particle emission only in infrared waveband.

Table.1.1.1. Previous studies of plume radiation for solid rocket motor (cont'd)

Authors	RTTE Solver	Radiative property estimation techniques	Comments
Pautrizel et al. [1]	Radiance Splitting method based on SHDOM	SNB	The model was applied to multi-layered 1-D configuration to predict the incoming infrared radiance and was compared with those of SHDOM with LBL. It was found that radiance splitting method is accurate for remote sensing problems.
Dombrovsky [40]	P <sub>1</sub>		It was found that scattering leads to decreasing the intensity in the normal direction to jet axis and to expanding the radiation angular dependence in the plane perpendicular to the axis.
Weichen et al. [41]	DOM	Seven spectral bands	Infrared signatures of three kinds of non-aluminized solid propellants were investigated. Plume field calculation and radiative transfer calculation were carried out coupled way. It was found that the energy characteristic of propellant influences plume radiation. Predictions obtained coupled solution for plume calculation was found to be lower than those of decoupled solution for higher energy characteristics of propellants whereas for low energy characteristics of propellants, predictions of coupled solution were found to be the same as those of decoupled solution.

## CHAPTER 2

### RADIATIVE TRANSFER EQUATION SOLUTION TECHNIQUES

In this chapter, DOM, Method of Lines (MOL) solution of DOM, P<sub>1</sub> and IDA are described for mathematical modeling of radiative heat transfer in enclosures. The physical situations to be considered are that of a uniform, radiatively grey/ non-grey, absorbing, emitting, scattering medium surrounded by grey, diffuse walls. Based on this physical problem, equations representing DOM, MOL solution of DOM, P<sub>1</sub> and IDA are derived starting from the RTE for three-dimensional rectangular coordinate system.

#### 2.1 Radiative Transfer Equation

The basis of all methods for the solution of radiation problems is the radiative transfer equation, which is derived by writing a balance equation for radiant energy passing in a specified direction through a small volume element in a uniform, non-grey, absorbing, emitting, scattering medium and can be written in the form

$$\begin{aligned} \boldsymbol{\Omega} \cdot \nabla I_{\nu}(\mathbf{r}, \boldsymbol{\Omega}) = & -(\kappa_{g\nu} + \kappa_{p\nu} + \sigma_{s\nu})I_{\nu}(\mathbf{r}, \boldsymbol{\Omega}) + (\kappa_{g\nu} + \kappa_{p\nu})I_{b\nu}(\mathbf{r}) \\ & + \frac{\sigma_{s\nu}}{4\pi} \int_{4\pi} I_{\nu}(\mathbf{r}, \boldsymbol{\Omega}') \Phi_{\nu}(\boldsymbol{\Omega}', \boldsymbol{\Omega}) d\Omega' \end{aligned} \quad (2.1.1)$$

where,  $I_{\nu}(\mathbf{r}, \boldsymbol{\Omega})$  is the spectral radiation intensity at position  $\mathbf{r}$  in the direction  $\boldsymbol{\Omega}$ .  $\kappa_{g\nu}$ ,  $\kappa_{p\nu}$  and  $\sigma_{s\nu}$  are the gas spectral absorption coefficient, particulate spectral absorption coefficient and particulate scattering coefficients of the medium respectively,  $I_{b\nu}(\mathbf{r})$  is the spectral black-body radiation intensity,  $\Phi_{\nu}(\boldsymbol{\Omega}', \boldsymbol{\Omega})$  is the spectral phase function for scattering which describes the fraction of energy scattered from incoming direction  $\boldsymbol{\Omega}'$  to the outgoing direction  $\boldsymbol{\Omega}$ .  $\Omega$  denotes the unit solid angle. The expression on the left-hand side represents the change of the intensity in the specified

direction  $\Omega$ . The terms on the right-hand side stand for absorption, emission, out-scattering and in-scattering respectively. For the grey, absorbing, emitting, scattering medium, the radiation intensity and radiative properties of the medium is taken as constant ( $I_\nu(\mathbf{r}, \Omega) = I(\mathbf{r}, \Omega)$ ,  $\kappa_{g\nu} = \kappa_g$ ,  $\kappa_{p\nu} = \kappa_p$ ,  $\sigma_{s\nu} = \sigma_s$ ,  $\Phi_\nu(\Omega', \Omega) = \Phi(\Omega', \Omega)$ ).

If the surface bounding the medium is a diffuse, grey wall at specified temperature, then Equation (2.1.1) is subject to the boundary condition

$$I(\mathbf{r}_w, \Omega) = \varepsilon_w I_{b,w} + \frac{(1-\varepsilon_w)}{4\pi} \int_{\mathbf{n} \cdot \Omega' < 0} I(\mathbf{r}, \Omega') |\mathbf{n} \cdot \Omega'| d\Omega' \quad \mathbf{n} \cdot \Omega' > 0 \quad (2.1.2)$$

where  $I(\mathbf{r}_w, \Omega)$  is the radiative intensity leaving the surface at a boundary location,  $\varepsilon_w$  is the surface emissivity,  $I_{b,w}$  is the black-body radiation intensity at the surface temperature,  $\mathbf{n}$  is the local outward surface normal and  $\mathbf{n} \cdot \Omega'$  is the cosine of the angle between incoming direction  $\Omega'$  and the surface normal. The first and second terms on the right-hand side of Equation (2.1.2) stand for the contributions to the leaving intensity due to emission from the surface and reflection of the incoming radiation, respectively.

## 2.2 Discrete Ordinates Method

DOM is based on representation of the continuous angular domain by a discrete set of ordinates with appropriate angular weights, spanning the total solid angle of  $4\pi$  steradians. The RTE is replaced by a discrete set of equations for a finite number of directions and each integral is replaced by a quadrature summed over the ordinate directions [16]. The discrete ordinates representation of RTE for non-grey absorbing-emitting-scattering medium in a rectangular coordinate system takes the following form

$$\begin{aligned} \mu_m \frac{\partial I_\nu^m}{\partial x} + \eta_m \frac{\partial I_\nu^m}{\partial y} + \xi_m \frac{\partial I_\nu^m}{\partial z} = & -(\kappa_{g\nu} + \kappa_{p\nu} + \sigma_{s\nu}) I_\nu^m + (\kappa_{g\nu} + \kappa_{p\nu}) I_{b\nu} \\ & + \frac{\sigma_{s\nu}}{4\pi} \sum_{m'=1}^M I_\nu^m w_{m'} \Phi_\nu(\Omega'_{m'}, \Omega_m) \end{aligned} \quad (2.2.1)$$

where  $I_v^m [\equiv I_v(\mathbf{r}, \boldsymbol{\Omega}_m)]$  is the radiation intensity at position  $\mathbf{r} = (x, y, z)$  in the discrete ordinate direction  $\boldsymbol{\Omega}_m$ ,  $m$  denotes the discrete ordinate ( $m = 1, 2, \dots, M$ ),  $M$  is the total number of ordinates used in the approximation.  $\mu_m, \eta_m$  and  $\xi_m$  are the direction cosines of  $\boldsymbol{\Omega}_m$  with x, y, and z axes, respectively and  $w_{m'}$  is the angular quadrature weight associated with the incoming direction  $\boldsymbol{\Omega}'_{m'}$ .

As the surfaces bounding the medium are diffuse and grey walls at specified temperatures, Equation (2.2.1) is subject to the following boundary conditions at two opposite walls normal to the x-axis

$$\text{at } x = 0, \quad I^m = \varepsilon_w I_{b,w} + \frac{(1-\varepsilon_w)}{4\pi} \sum_{\mu_{m'} < 0} I^{m'} w_{m'} |\mu_{m'}| \quad \mu_{m'} > 0 \quad (2.2.2)$$

$$\text{at } x = L, \quad I^m = \varepsilon_w I_{b,w} + \frac{(1-\varepsilon_w)}{4\pi} \sum_{\mu_{m'} > 0} I^{m'} w_{m'} |\mu_{m'}| \quad \mu_{m'} < 0 \quad (2.2.3)$$

Similar expressions hold for the boundaries in the other coordinate directions. Once the radiation intensities are solved from Equation (2.2.1) together with boundary conditions, the z-component of the radiative heat flux which is the parameter of interest can be obtained from

$$q_z = \sum_{m'}^M I^{m'} w_{m'} \xi_{m'} \quad (2.2.4)$$

In the present work, radiation code based on DOM with GG developed by Selçuk and her coworkers [5,42-43] was used for selection of RTE solution technique for the radiation code. DOM is solved based on finite volume technique with step scheme as the spatial differencing scheme. Further details of DOM with GG code can be found in [5] and [43]. Radiation code based on DOM with SNBCK and Mie Theory (DOMSNBCKMIE) was developed for radiation code by modifying and improving DOM with GG code [5]. SNBCK was utilized for radiative property estimation of gases. Radiative properties of particles are evaluated by using Mie Theory. Further details of

SNBCK and Mie Theory can be found in section of 3.3 and 3.4, respectively. The Henyey-Greenstein function was used to evaluate scattering phase function as [44]

$$\Phi_{HG}(\theta) = \frac{1-g^2}{[1+g^2-2g\cos\theta]^{3/2}} \quad (2.2.5)$$

### 2.2.1 Structure and Operation of the Computer Code DOMSNBCKMIE

Figure 2.1 and Figure 2.2 illustrate the flow diagram of the computer code based on DOM with SNBCK and Mie Theory which is modified and improved from DOM with GG code [5]. The general steps of the computer code are as follows:

1. Define the subdivision of the enclosure, order of approximation, minimum and maximum wavenumber.
2. Read in the input data specifying the physics of the problem which are, the dimensions of the enclosure, wall temperatures and emissivities, and temperature and concentration profiles of the medium, SNBCK data for H<sub>2</sub>O, CO<sub>2</sub> and CO as a function of temperature, wavenumber and 7-point Gauss-Labatto quadrature scheme and scattering cross-section, extinction cross-section and asymmetry factor of particles as a function of wavenumber, temperature, particle diameter.
3. Calculate absorption coefficient of the combustion gases medium as a function of temperature and concentration profiles of the medium by using SNBCK data for H<sub>2</sub>O, CO<sub>2</sub> and CO for each wavenumber.
4. Calculate absorption coefficient and scattering coefficient of particle for each wavenumber.
5. Calculate extinction coefficient and albedo of the particle laden combustion gases for each wavenumber.
6. Specify the direction cosines and corresponding weights.
7. Calculate constants for finite volume.



8. Calculate phase functions for each incoming and outgoing ordinates.
9. Specify a wavenumber
10. Initialize the band averaged intensity at all ordinates at all grid points for the wavenumber.
11. Specify a Gauss-Labatto quadrature point.
12. Calculate the initial source term required for first iteration for the Gauss-Labatto quadrature point.
13. Sweep the enclosure for each ordinate to calculate cell-center intensities and incoming intensities on the walls for given boundary conditions and source terms.

**SWEEP**

14. Select corner
15. Sweep along x-axis (+ or -)
16. Shift to next y-location (+ or -), repeat step 15
17. Repeat step 16 until the x-y plane at the first z- location is sweep at x-y plane at this location is completed.
18. Repeat step 17 until all the enclosure is swept.
19. Collect all information from all sweeps.
20. Check for convergence by comparing the solutions at current step with those at previous step. If current solution is within the specified range of the previous solutions, convergence is established go to step 22.
21. If convergence is not established, save the solution for convergence check.
22. If convergence is established, calculate the parameters of interest.
23. Repeat steps 11-22 for all Gauss-Labatto quadrature points and

24. Calculate band averaged intensity at each wavenumber by using Equation (3.3.13) and print out.
25. Repeat steps 9-22 for all wavenumber.
26. Stop.

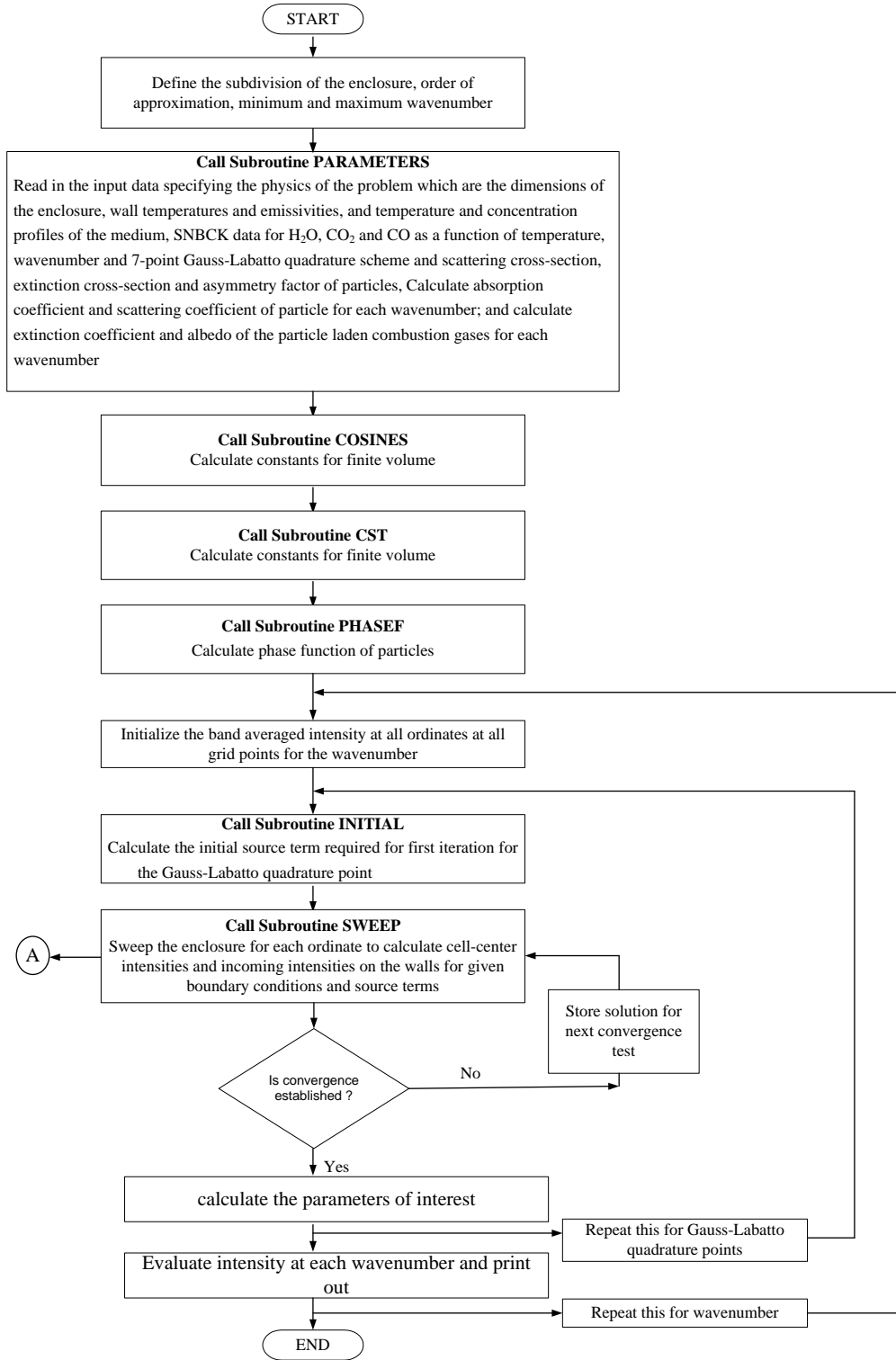


Figure 2.1. Flowchart of DOMSNBCKMIE

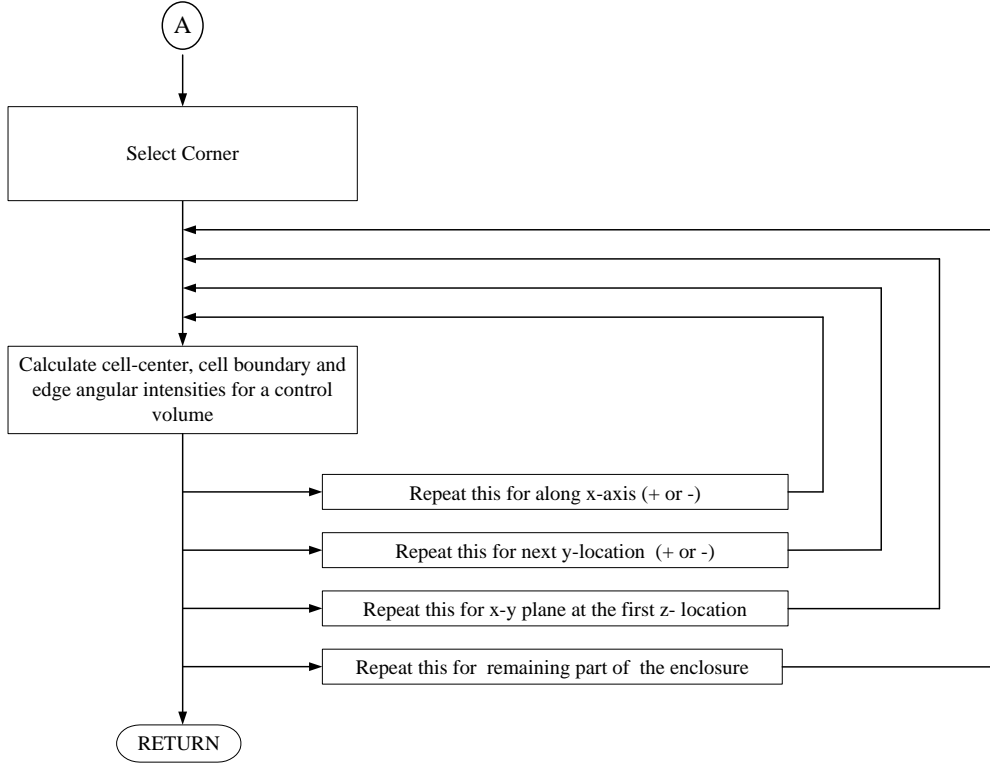


Figure 2.2. Algorithm of the subroutine SWEEP

### 2.3 Method of Lines Solution of Discrete Ordinates Method

MOL solution of DOM provides efficient and flexible computation using various higher-order approximations for temporal and spatial discretization. This approach involves the time derivative addition of intensity into the discrete ordinates equations given by Schiesser [45]. The MOL solution of DOM representation of RTE for non-grey absorbing-emitting-isotropically scattering medium in a rectangular coordinate system takes the following form

$$\begin{aligned}
 k_t \frac{\partial I_v^m}{\partial t} = & - \left( \mu_m \frac{\partial I_v^m}{\partial x} + \eta_m \frac{\partial I_v^m}{\partial y} + \xi_m \frac{\partial I_v^m}{\partial z} \right) + (\kappa_{pv} + \kappa_{gv}) I_{bv} - (\kappa_{pv} + \kappa_{gv} + \sigma_{pv}) I_v^m \\
 & + \frac{\sigma_{pv}}{4\pi} \sum_{m'=1}^M \Phi_v(\boldsymbol{\Omega}_{m'}, \boldsymbol{\Omega}_m) w_{m'} I_v^{m'}
 \end{aligned} \tag{2.3.1}$$

where  $t$  is the pseudo-time variable and  $k_t$  is a time constant with dimension  $[(m/s)^{-1}]$  which is introduced to maintain dimensional consistence in the equation and is taken as unity. Real-time solutions can be obtained by dividing pseudo-time solutions by the speed of light.  $I_v^m [\equiv I_v(\mathbf{r}, \boldsymbol{\Omega}_m)]$  is the radiation intensity at position  $\mathbf{r} = (x, y, z)$  in the discrete ordinate direction  $\boldsymbol{\Omega}_m$ ,  $m$  denotes the discrete ordinate ( $m = 1, 2, \dots, M$ ),  $M$  is the total number of ordinates used in the approximation and  $w_{m'}$  is the angular quadrature weight associated with the incoming direction  $\boldsymbol{\Omega}_{m'}$ .  $\kappa_{gv}$ ,  $\kappa_{pv}$  and  $\sigma_{pv}$  are the gas spectral absorption coefficient, particulate spectral absorption coefficient and particulate spectral scattering coefficients of the medium respectively,  $I_{bv}$  is the spectral black-body radiation intensity and  $\Phi_v(\boldsymbol{\Omega}_{m'}, \boldsymbol{\Omega}_m)$  is the phase function for scattering.

If the boundary of the medium is a diffuse grey wall at a specified temperature, Equation (2.3.1) is subjected to following the boundary conditions at two opposite walls normal to the x-axis

$$\text{at } x = 0, I(\mathbf{r}_w, \boldsymbol{\Omega}) = \varepsilon_w I_{b,w} + \frac{(1-\varepsilon_w)}{4\pi} \sum_{\mu_{m'} < 0} I_v^{m'} w_{m'} |\mu_{m'}|, \quad \mu_m > 0 \quad (2.3.2)$$

$$\text{at } x = L, I(\mathbf{r}_w, \boldsymbol{\Omega}) = \varepsilon_w I_{b,w} + \frac{(1-\varepsilon_w)}{4\pi} \sum_{\mu_{m'} > 0} I_v^{m'} w_{m'} |\mu_{m'}|, \quad \mu_m < 0 \quad (2.3.3)$$

Similar expressions hold for the boundaries in the other coordinate directions.

Following the MOL approach, the system of partial differential equations (PDEs), Equation (2.3.1) is transformed into an ordinary differential equation (ODE) initial-value problem by using finite difference approximations. Starting from an initial condition for radiation intensities in all directions, the resulting ODE system is integrated until steady state by using a powerful ODE solver. The ODE solver takes the burden of time discretization and chooses the time steps in a way that maintains the accuracy and stability of the evolving solution. Any initial condition can be chosen to start the integration, as its effect on the steady-state solution decays to insignificance. In order to stop the integration at the steady state, a convergence criterion is introduced. If

the intensities at all nodes and ordinates for all grey gases satisfy the condition given below, the solution at the time is considered to be the steady-state solution and the integration is terminated [46]. The condition for steady state is

$$\frac{|I_t - I_{t-1}|}{I_{t-1}} < \epsilon \quad (2.3.4)$$

where  $\epsilon$  is the error tolerance and the subscript  $t$  and  $t-1$  denote the solutions at current time and at previous time, respectively. Therefore, the steady-state intensities at all grid points for all wavenumbers can be evaluated by solving Equations (2.3.1)-(2.3.3).

In the present work, radiation code based on MOL solution of DOM with GG developed by Selçuk and her coworkers [42,43,47] and radiation code based on MOL solution of DOM with SLW developed by Selçuk and her coworkers [48, 49] were used and radiation code based on MOL solution of DOM with SNBCK was developed to select radiative property estimation technique for radiation code.

### **2.3.1 Structure and Operation of the Computer Code MOL solution of DOM with SNBCK**

Figure 2.3 and Figure 2.4 display the flow diagram of the computer code based on MOL solution of DOM with SNBCK which is modified from MOL solution of DOM with GG code [42,43,47]. Further details of SNBCK can be found in section of 4.3. The general steps of the computer code are as follows:

1. Define the subdivision of the enclosure, order of approximation, spatial differencing scheme, minimum and maximum wavenumber, and number of equations in the system of ODEs.
2. Declare 5-D arrays to store intensities, position derivatives, and time derivatives at each ordinate of each grid point for each gray gas. The 5-D arrays are of dimensions  $[NX \times NY \times NZ \times ND \times NM]$  where  $NX, NY$  and  $NZ$  are the number of nodes along  $x, y$  and  $z$ -axes respectively,  $ND$  stands for number of octants ( $ND = 8$  for a 3-D

problem) and  $NM$  is the number of ordinates specified by order of angular quadrature.

3. Read in the input data specifying the physics of the problem which are, the dimensions of the enclosure, wall temperatures and emissivities, and temperature and concentration profiles of the medium, SNBCK data for  $H_2O$  and  $CO_2$  ( $k_i$ ) as a function of temperature, wavenumber and 7-point Gauss-Labatto quadrature scheme and absorption coefficient and scattering coefficient of particles .
4. Calculate absorption coefficient of the combustion gases medium as a function of temperature and concentration profiles of the medium by using SNBCK data for  $H_2O$  and  $CO_2$  and for each wavenumber.
5. Calculate extinction coefficient and albedo of the particle laden combustion gases for each wavenumber.
6. Read in input data related with the ODE integrator which are the initial time, final time, print interval and the error tolerance.
7. Set the initial conditions required for the ODE integrator.
8. Specify the direction cosines and corresponding weights.
9. Specify a wavenumber
10. Initialize the band averaged intensity at all ordinates at all grid points.
11. Specify a Gauss-Labatto quadrature point.
12. Initialize the intensities at all ordinates at all grid points for Gauss-Labatto quadrature point.
13. Set boundary conditions for the intensities leaving the boundary surfaces.

#### **Calculation of the Approximations for the Spatial Derivatives**

14. Specify an octant, and an ordinate.
15. Specify a discrete location on the  $y,z$  plane.

16. Store the values of the intensities (at this direction and location) along x-axis in a 1-D array.
17. Call for spatial discretization subroutine which accepts the 1-D array of intensities as an input and computes the derivative with respect to r-axis as an output over the grid of NX points.
18. Transfer the 1-D array of spatial derivatives into the 5-D array of x-derivatives.
19. Repeat steps 14-18 for all discrete locations y-z plane, all ordinates and all octants.
20. Repeat steps 14-18 for derivative terms with respect to y and z-axes, forming 1-D arrays along y and z-axes.

#### **Calculation of the Time Derivatives**

21. Calculate the time derivative of intensity at each node for each ordinate of each octant using Equation (3.3.1) to form a 5-D array of time derivatives.
22. Transform the 5-D arrays of intensities and time derivatives into 1-D arrays to be sent to the ODE solver.

#### **Integration of the system of ODEs**

23. Call the ODE solver subroutine to integrate the system of ODEs by using a time adaptive method. The ODE propagates in time by solving for the intensities at a time step j, calculating the time derivatives by performing steps 14 to 22 and integrating again to solve for intensities at the new time step j+1.
24. Return to the main program at prespecified time intervals.
25. Check if ODE integration has proceeded satisfactorily; print an error message if an error condition exists.
26. Transfer the solution at current print point from the 1-D array to a 5-D array.
27. Set the boundary conditions at current time step.
28. Print solution.



29. Check for convergence by comparing the solutions at current time step with those at previous three time steps. If current solution is within the specified range of the previous solutions, convergence is established go to step 32.
30. If convergence is not established, save the solution for convergence check.
31. Check the end of run time if final time is not reached go back to step 14.
32. If convergence is established or final time is reached, calculate the parameters of interest.
33. Repeat steps 11-32 for all Gauss-Labatto quadrature points.
34. Calculate band averaged intensity at each wavenumber by using Equation (3.3.13) and print out.
35. Repeat steps 9-34 for all wavenumber.
36. Calculate overall incident radiative heat flux and source term
37. Print output.
38. Stop.

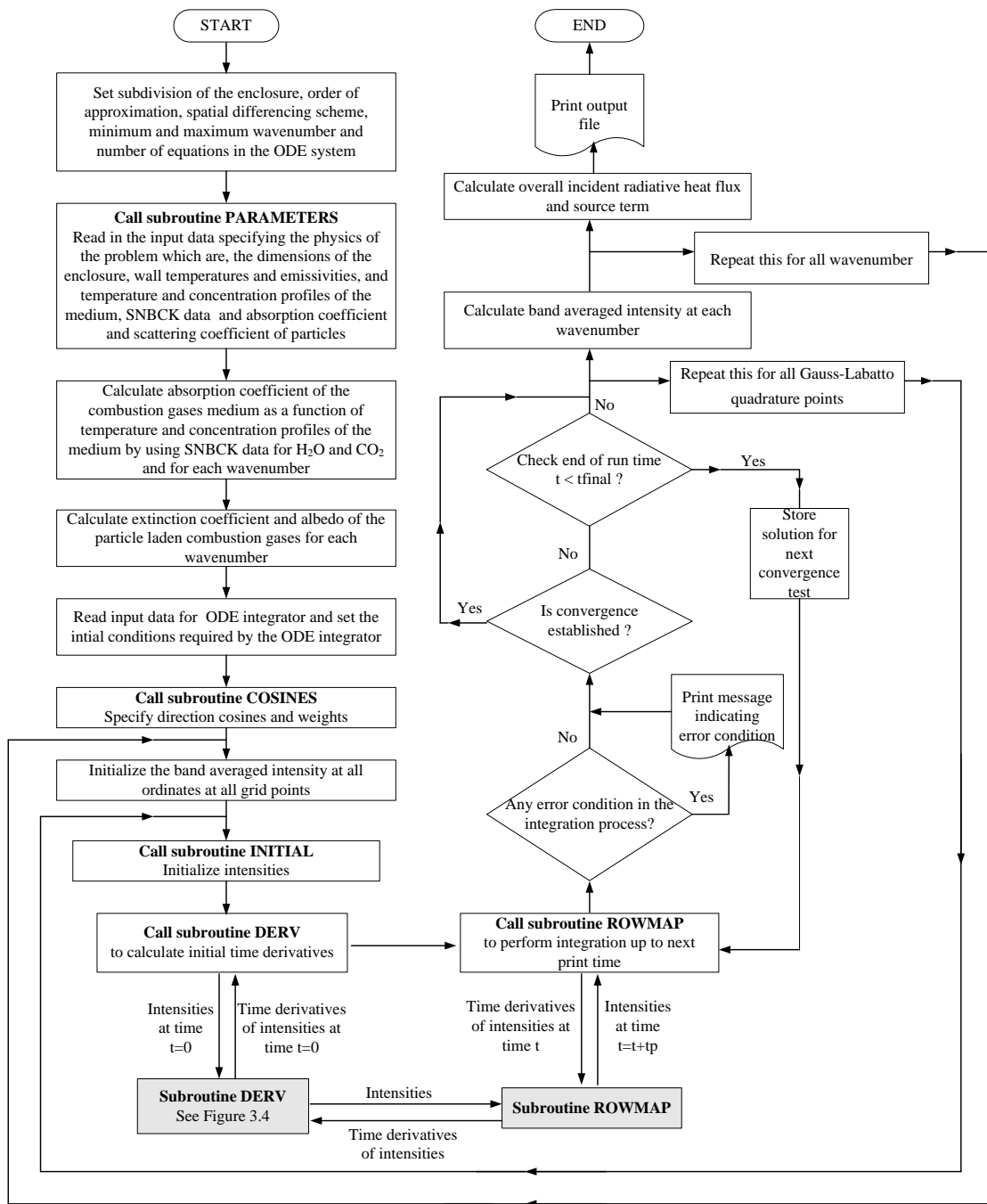


Figure 2.3. Flowchart of MOL solution of DOM with SNBCK

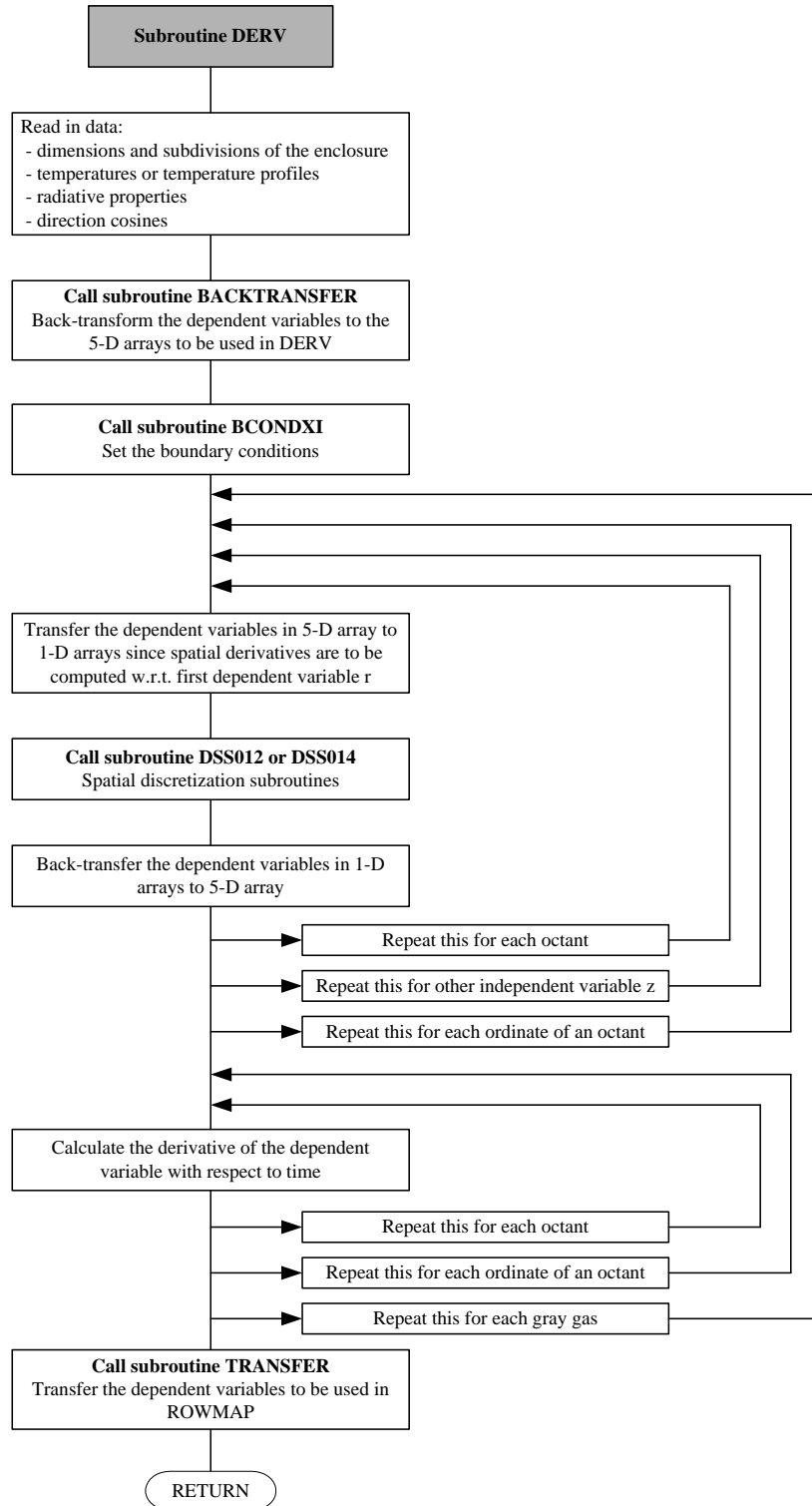


Figure 2.4. Algorithm of the subroutine DERV

## 2.4 P<sub>1</sub> Approximation

Equation (2.1.1) can be rewritten in terms of non-dimensional optical coordinates and source function

$$\boldsymbol{\Omega} \cdot \nabla_{\tau} I(\mathbf{r}, \boldsymbol{\Omega}) = S(\mathbf{r}, \boldsymbol{\Omega}) - I(\mathbf{r}, \boldsymbol{\Omega}) \quad (2.4.1)$$

where  $I(\mathbf{r}, \boldsymbol{\Omega})$  denotes the intensity at position  $\mathbf{r}$  in the direction  $\boldsymbol{\Omega}$ ,  $\tau$  is optical thickness along the ray traveling into a direction  $\boldsymbol{\Omega}$  and  $S(\mathbf{r}, \boldsymbol{\Omega})$  is the radiative source term given by

$$S(\mathbf{r}, \boldsymbol{\Omega}) = (1 - \omega)I_b(\mathbf{r}) + \frac{\omega}{4\pi} \int_{4\pi} I(\mathbf{r}, \boldsymbol{\Omega}') \Phi(\boldsymbol{\Omega}', \boldsymbol{\Omega}) d\boldsymbol{\Omega}' \quad (2.4.2)$$

where  $\omega$  is the single scattering albedo,  $I_b(\mathbf{r})$  is the black body intensity,  $\Phi(\boldsymbol{\Omega}', \boldsymbol{\Omega})$  denotes the scattering phase function.

P<sub>1</sub> provides a solution for RTE based on the spherical harmonics method truncated at the first order. Details of the derivation may be found in [44] in particular. As a summary, the intensity can be rewritten in terms of incident radiation,  $G(\mathbf{r})$ , and radiative heat flux,  $\mathbf{q}(\mathbf{r})$ , as

$$I(\mathbf{r}, \boldsymbol{\Omega}) = \frac{1}{4\pi} (G(\mathbf{r}) + 3\mathbf{q}(\mathbf{r}) \cdot \boldsymbol{\Omega}) \quad (2.4.3)$$

Then, assuming a linear anisotropic scattering, in in-scattering term is simplified as

$$\frac{\omega}{4\pi} \int_{4\pi} I(\mathbf{r}, \boldsymbol{\Omega}') \Phi(\boldsymbol{\Omega}', \boldsymbol{\Omega}) d\boldsymbol{\Omega}' = \frac{\omega}{4\pi} [G(\mathbf{r}) + A_1 \mathbf{q}(\mathbf{r}) \cdot \boldsymbol{\Omega}] \quad (2.4.4)$$

where  $A_1$  is the coefficient of linear anisotropy of the assumed scattering phase function,  $\Phi(\boldsymbol{\Omega}', \boldsymbol{\Omega}) = 1 + A_1 \boldsymbol{\Omega}' \cdot \boldsymbol{\Omega}$ . Equation (2.4.1) is finally rewritten, after some manipulations, in terms of incident radiation and radiative heat flux, providing the following set of equations

$$\nabla_{\tau} \mathbf{q}(\mathbf{r}) = (1 - \omega)(4\pi I_b(\mathbf{r}) - G(\mathbf{r})) \quad (2.4.5)$$

$$\nabla_{\tau} G(\mathbf{r}) = -(3 - A_1 \omega) \mathbf{q}(\mathbf{r}) \quad (2.4.6)$$

Equation (2.4.5) is the divergence of the radiative heat flux, which would be a source term involved in the energy balance. Equation (2.4.6) gives a mean to compute the radiative heat flux knowing the incident radiation field. Combining both equations provides a partial differential equation to be solved numerically

$$\nabla_{\tau} \left( \frac{1}{(3 - A_1 \omega)} \nabla_{\tau} G(\mathbf{r}) \right) - (1 - \omega) G(\mathbf{r}) = -(1 - \omega) 4\pi I_b(\mathbf{r}) \quad (2.4.7)$$

Boundary conditions by Marshak [50] are usually taken into consideration. It implies the following formulation for opaque boundaries with emissivity  $\varepsilon_w$

$$-\frac{2 - \varepsilon_w}{\varepsilon_w} \frac{2}{(3 - A_1 \omega)} \nabla_{\tau} G(\mathbf{r}_w) \cdot \mathbf{n} + G(\mathbf{r}_w) = 4\pi I_b(\mathbf{r}_w) \quad (2.4.8)$$

where  $\mathbf{n}$  is the normal vector to the boundary,  $G(\mathbf{r}_w)$  is the incident radiation set at a location  $\mathbf{r}_w$  on the wall and  $I_b(\mathbf{r}_w)$  is the blackbody intensity at the wall temperature.

In the present work, the code based on P<sub>1</sub> was developed. In the code, the total intensity of incident radiation is first solved from Equation (2.4.7) together with boundary conditions by using finite difference method and then the z-component of the radiative heat flux which is the parameter of interest can be obtained from Equation (2.4.5).

## 2.5 Improved Differential Approximation

IDA addresses the wall contribution and the radiation coming from the medium in a separate manner. The starting point is RTE (Equation (2.4.1)) written in its integral form

$$I(\mathbf{r}, \boldsymbol{\Omega}) = \frac{J_w(\mathbf{r}_w)}{\pi} e^{-\tau_r} + \int_0^{\tau_r} S(\mathbf{r}', \boldsymbol{\Omega}) e^{-(\tau_r - \tau_{r'})} d\tau_{r'} \quad (2.5.1)$$

where  $J_w(\mathbf{r}_w)$  is the radiosity at the wall,  $\tau_r = \int_0^r \beta dr'$  is the optical distance between that point on the wall from which the beam emits and the point under consideration,  $r'$

is the location in the medium between the emission point on the wall and the point under consideration and  $\beta$  is the extinction coefficient. The first expression on the right hand side deals with the wall contribution ( $I_w$ ), involving its radiosity, attenuated along the ray path from wall,  $\mathbf{r}_w$ , up to position  $\mathbf{r}$ . The second one stands for the source term due to emission and in-scattering of radiation inside the medium along the path and represents the medium contribution ( $I_{med}$ ). In IDA method,  $I_{med}$  is approximated from the  $P_1$  approximation as

$$I_{med}(\mathbf{r}, \boldsymbol{\Omega}) \approx \int_0^{\tau_r} S^*(\mathbf{r}', \boldsymbol{\Omega}) e^{-(\tau_r - \tau_{r'})} d\tau_{r'} \quad (2.5.2)$$

where

$$S^*(\mathbf{r}, \boldsymbol{\Omega}) = (1 - \omega)I_b(\mathbf{r}) + \frac{\omega}{4\pi} [G^*(\mathbf{r}) + A_1 \mathbf{q}^*(\mathbf{r}) \cdot \boldsymbol{\Omega}] \quad (2.5.3)$$

This equation is based on linear anisotropic scattering. The asterisk is used for the corresponding variables obtained from the  $P_1$  approximation (seen section 2.4).

The integral (2.5.2) can be calculated analytically assuming the linearity of the source function [10], finally yielding

$$I_{med}(\mathbf{r}, \boldsymbol{\Omega}) \approx S^*(\mathbf{r} - \mathbf{r}_o, \boldsymbol{\Omega})(1 - e^{-\tau_r}) \quad (2.5.4)$$

where the specific distance  $\mathbf{r}_o$  in the medium is related to the following optical distance

$$\tau_o = 1 - \frac{\tau_r e^{-\tau_r}}{1 - e^{-\tau_r}} \quad (2.5.5)$$

Substitution of Equation (2.5.4) into Equation (2.5.1) leads to

$$I(\mathbf{r}, \boldsymbol{\Omega}) \approx \frac{J_w(\mathbf{r}_w)}{\pi} e^{-\tau_r} + S^*(\mathbf{r} - \mathbf{r}_o, \boldsymbol{\Omega})(1 - e^{-\tau_r}) \quad (2.5.6)$$

where

$$J_w(\mathbf{r}) = \varepsilon_w \pi I_{bw}(\mathbf{r}) + (1 - \varepsilon_w) \int_{\mathbf{n} \cdot \boldsymbol{\Omega} < 0} I_w(\mathbf{r}', \boldsymbol{\Omega}) |\mathbf{n} \cdot \boldsymbol{\Omega}| d\Omega \quad (2.5.7)$$

Once the radiative intensity distribution is determined, the improved values for radiative heat flux can be obtained from

IDA solution necessitates following steps:

- solution of  $P_1$  to evaluate variables with asterisk;
- determination of radiosities;
- evaluation of intensity for any point inside the medium.

In IDA, the intensity in the medium is evaluated by using a ray tracing (RT) process, scanning the medium from cell to cell. The RT process requires following significant numbers of rays for each cell inside the medium and each boundary cell face and so this procedure increases the computational cost. When angular discretization methods are used instead of RT process, the number of directions reduces and hence CPU time requirement decreases [11].

### **2.5.1 Structure and Operation of the Computer Code IDA**

In the present work, the code based on IDA with different angular discretization methods was developed. Figure 2.5 and Figure 2.6 show the flow diagram of the computer code. The general steps of the computer code are as follows:

1. Define the subdivision of the enclosure and order of approximation.
2. Read input data specifying the physics of the problem which are the dimension of enclosure, temperature of the medium and the walls, emissivities of the walls, absorption and scattering coefficients of the medium, and the linear anisotropy of scattering coefficient.
3. Specify the direction cosines and corresponding weights.

4. Determine the central points of all control volumes in order to specify the location of medium grid points.

**Calculate incident radiation and radiative heat flux by  $P_1$  approximation**

5. Initialize incident radiation at all grid points
6. Set blackbody intensity of the medium.
7. Set blackbody intensity at the boundaries.
8. Calculate incident radiation at boundaries using Equation (2.4.8)
9. Calculate incident radiation of the medium using Equation (2.4.7)
10. Check for convergence by comparing the calculated incident radiation at current step with those at previous calculation step. If the current solution is within the specified range of the previous solutions, convergence is established go to step 12.
11. If convergence is not established, save the solution for convergence check and go to step 8.
12. If convergence is established, calculate radiative heat flux using Equation (3.4.5).
13. Print radiative heat flux to output file.

**Calculate Intensities**

14. Calculate source term of each cell by incident radiation and radiative heat flux obtained from the  $P_1$  approximation using Equation (2.5.3).
15. Calculate wall radiosity using Equation (2.5.7)
16. Fire the rays in specified directions from each cell centre.
17. Follow the path of each direction from cell centre till it intersects the far wall to calculate the distance the ray travels.



18. Evaluate the specific distance,  $r_o$ , by using Equation (2.5.5) to determine intensity coming from medium by using Equation (2.5.4).
19. Calculate the intensity at the cell centre where the ray is fired by applying Equation (2.5.6) with the known boundary condition at the point of intersection on the wall.
20. Calculate the z-component of the radiative heat flux which is the parameter of interest.
21. Print the z-component of the radiative heat flux to output file.

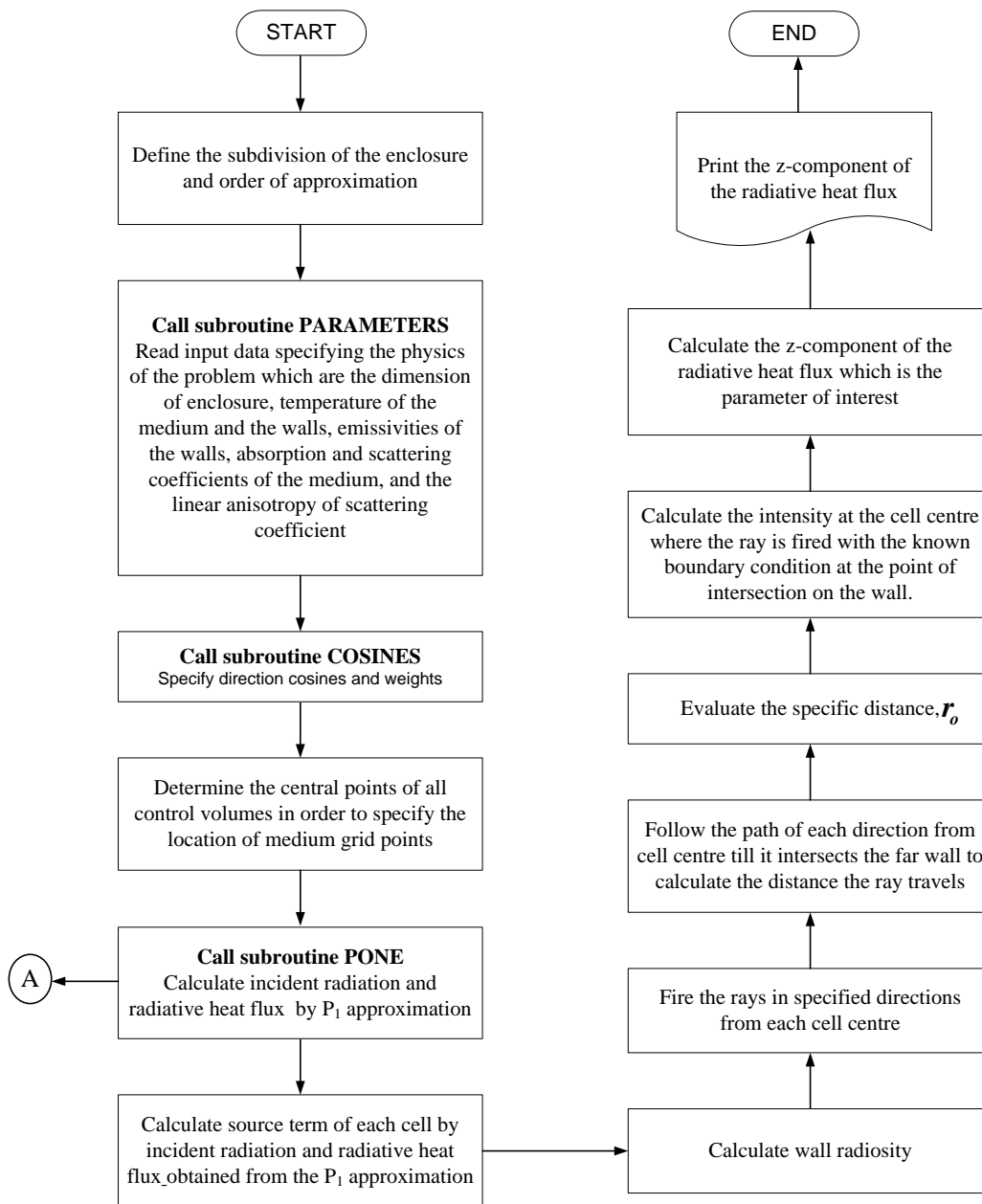


Figure 2.5 Flowchart for IDA

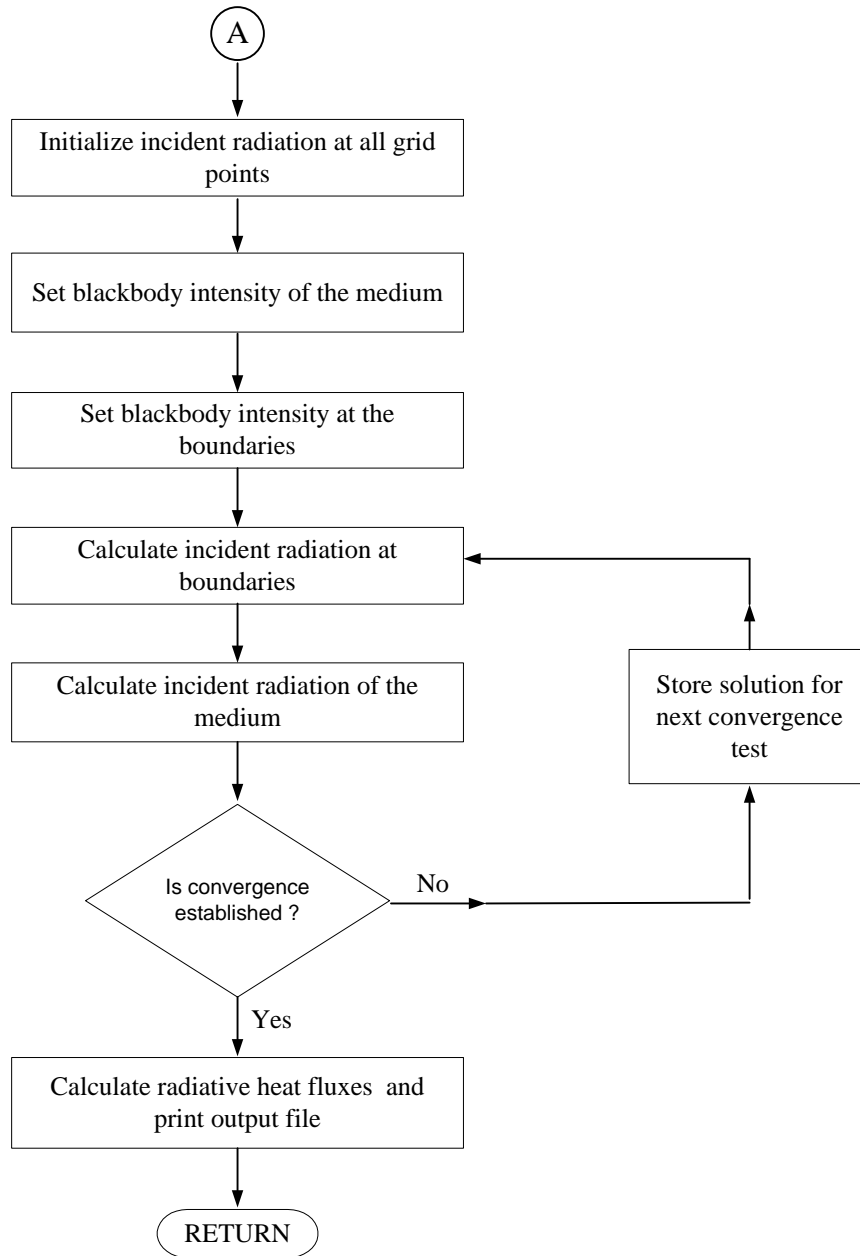


Figure 2.6 Algorithm of the subroutine  $P_1$  Approximation

## 2.6 Angular Discretization

Angular discretization is characterized by the angular quadrature scheme and the order of approximation.  $S_N$  and  $T_N$  are the angular quadrature schemes most commonly used for discretization.  $S_N$  quadrature originally developed by Carlson and Lathrop [51] satisfies a number of key moments of the radiative intensity. Extended level symmetric  $S_N$  quadratures that accurately satisfy key moments of the RTE and its boundary conditions as well as higher order moments of complex phase functions are proposed by El Wakil and Sacadura [52] and Fiveland [53]. A sketch of the directions used in one octant of a unit sphere for  $S_2$ ,  $S_4$ ,  $S_6$ ,  $S_8$  and  $S_{10}$  order of approximations is shown in Figure 2.7. As can be seen from the figure, discrete directions are ordered in levels (constant  $\theta$ ) and number of directions is different at each level.

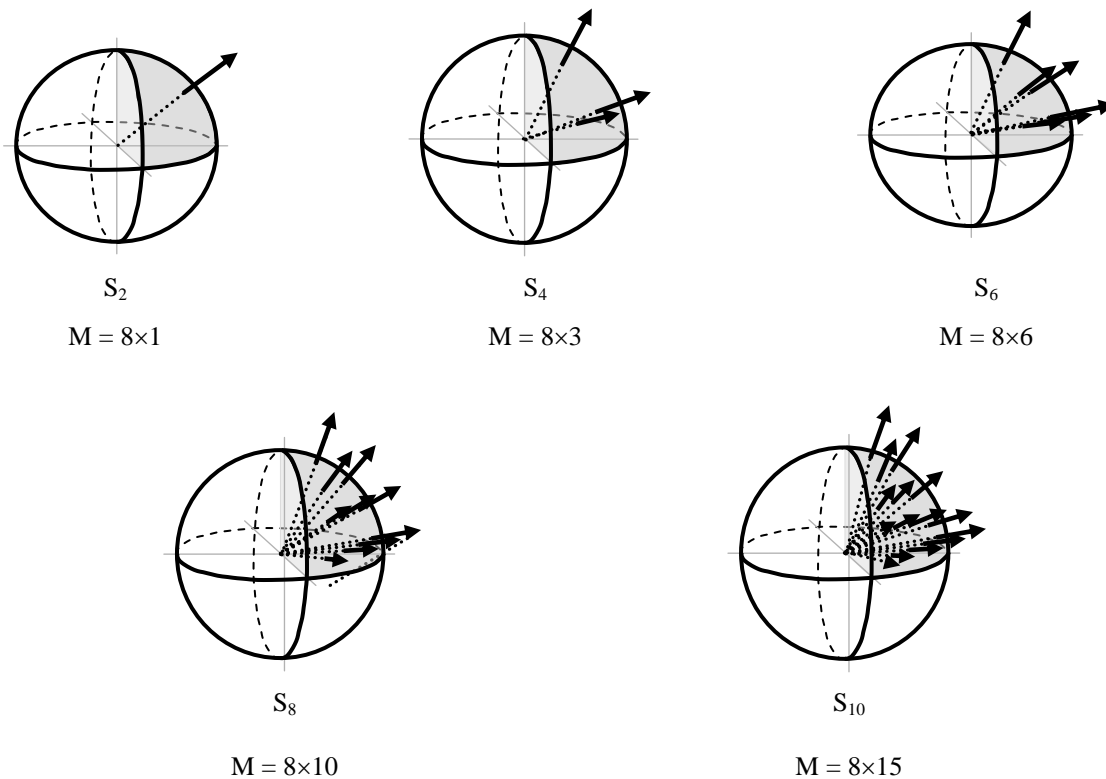


Figure 2.7 Orders of approximation for  $S_N$

$T_N$  quadrature developed by Thurgood and his coworkers [54] provides more accurate results in computing the first-order moment and a finer angular resolution, which is not possible by using  $S_N$  quadrature, allowing greater reduction or virtual elimination of the ray effect. In the  $T_N$  quadrature set, the basal equilateral triangle with vertices at  $(1,0,0)$ ,  $(0,1,0)$  and  $(0,0,1)$  is used for mapping the octant. The basal triangle is divided into  $N^2$  smaller equilateral triangles. Each ray passing through the centroids of the smaller triangles is defined as the direction associated with respect to the smaller triangle. The assembly of equilateral triangles and centroids onto the surface of the unit sphere is then mapped [54]. The tessellations of the basal triangle and the sphere triangles for  $T_4$  quadrature set are illustrated in Figure 2.8.

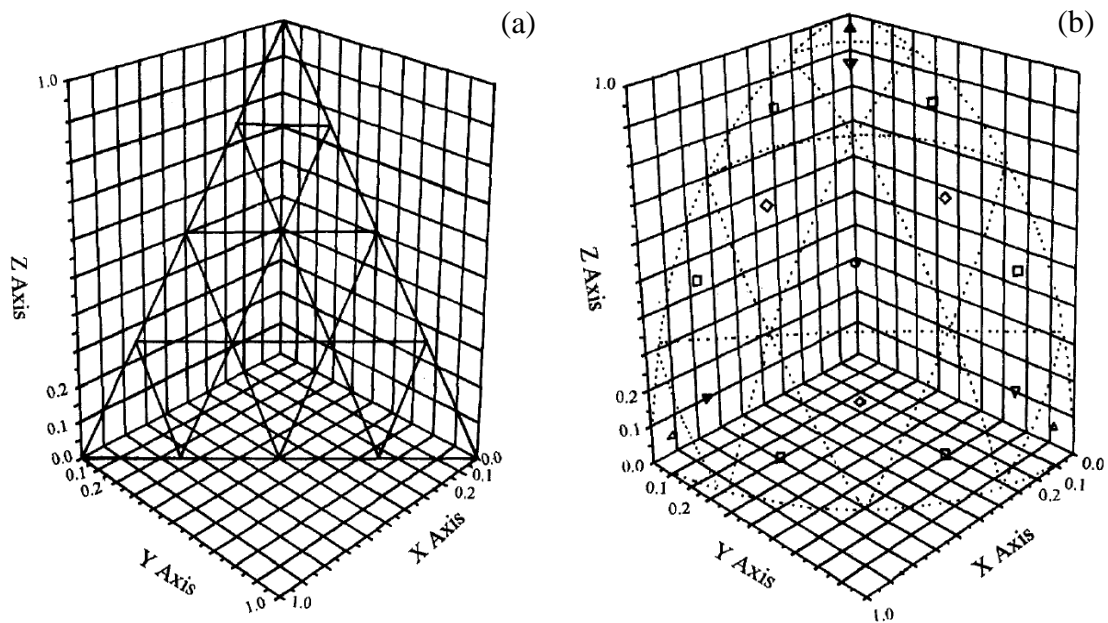


Figure 2.8. Orders of approximation for  $T_4$  (a) Tessellation of basal equilateral triangle  
(b) sphere triangles [54]

Table 2.1 summarizes formulæ of number of ordinates per octant and total number of ordinates for  $S_N$  and  $T_N$  quadratures in three-dimensional systems. The quadrature ordinates and weights for axisymmetric cylindrical geometry of  $S_N$  and  $T_N$  approximations are listed in Appendix A.

Table 2.1. Number of ordinates for  $S_N$  and  $T_N$  quadratures in 3-D systems

<b>Angular Quadrature Scheme</b>	<b>Formulæ for number of ordinates per octant</b>	<b>Formulæ for total number of ordinates</b>
$S_N$	$N(N+2)/8$	$M=2^D N(N+2)/8$
$T_N$	$N^2$	$M=8 N^2$

In this study, CFD solver, ANSYS FLUENT, coupled with radiative heat transfer is used to obtain flow field of plume. Angular discretization in ANSYS FLUENT is carried out by dividing each octant into  $N_\theta \times N_\phi$  solid angles of extent  $\omega_i$  at any spatial location. The angles  $\theta$  and  $\phi$  are represent the polar and azimuthal angles respectively, and are measured according to the Cartesian system ( $\mathbf{x}$ ,  $\mathbf{y}$ ,  $\mathbf{z}$ ) as shown in Figure 2.9. Control angles,  $\Delta\theta$  and  $\Delta\phi$  are taken as constant. Total directions become  $8N_\theta N_\phi$  in three-dimensional enclosures [55].

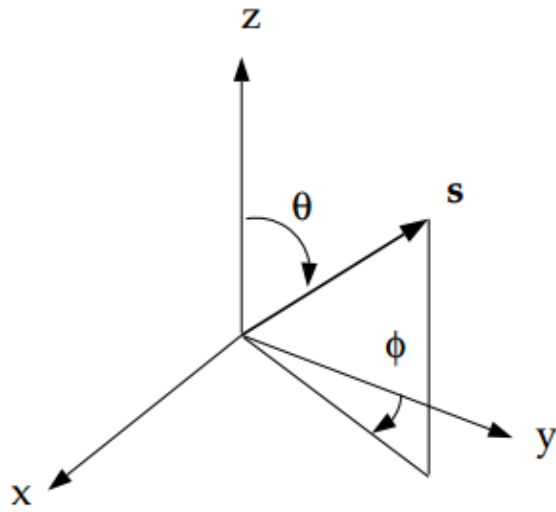


Figure 2.9. Angular Coordinate System used in ANSYS FLUENT [55]





## CHAPTER 3

### ESTIMATION OF RADIATIVE PROPERTIES

Accurate determination of radiative transfer necessitates both accurate solution of the RTE and reliable evaluation of the medium radiative properties. In this chapter, Grey Gas (GG), Spectral Line-based Weighted Sum of Grey Gases (SLW), Statistical Narrow-Band Correlated-k (SNBCK) models used for calculation of gas radiative properties and Mie theory used for evaluation of  $\text{Al}_2\text{O}_3$  particle radiative properties are described.

#### 3.1 Grey Gas Model

In the GG model, the radiative properties of the participating combustion gases are estimated by using Leckner's correlations [56], which require the partial pressures of carbon dioxide and water vapor, the gas temperature and mean beam length,  $L_m$ . Calculation of the gas emissivity,  $\varepsilon_g$ , through Leckner's correlations leads to gas absorption coefficient expressed by

$$\kappa_g = -(1/L_m)\ln(1 - \varepsilon_g) \quad (3.1.1)$$

For the grey, absorbing, emitting, scattering medium, the radiation intensity and radiative properties of the medium in Equation (2.1.1) are taken as constant ( $I_v(\mathbf{r}, \boldsymbol{\Omega}) = I(\mathbf{r}, \boldsymbol{\Omega})$ ,  $\kappa_{gv} = \kappa_g$ ,  $\kappa_{pv} = \kappa_p$ ,  $\sigma_{pv} = \sigma_p$ ,  $\Phi_v(\boldsymbol{\Omega}', \boldsymbol{\Omega}) = \Phi(\boldsymbol{\Omega}', \boldsymbol{\Omega})$ ).

In the present study, radiation code based on MOL solution of DOM with GG model developed by Selçuk and her coworkers [47] was used. Further details of the code can be found in [47].

### 3.2 Spectral Line-based Weighted Sum of Grey Gases Model

In the SLW model, the non-grey gas is replaced by a number of grey gases which are logarithmically spaced between  $3 \times 10^{-5}$  and  $60 \text{ m}^2/\text{mol}$  for water vapor and  $3 \times 10^{-5}$  and  $120 \text{ m}^2/\text{mol}$  for carbon dioxide as recommended by Denison and Webb [57].

In order to calculate total heat transfer rates in a mixture of two gases,  $\text{H}_2\text{O}$  and  $\text{CO}_2$ , the RTE [Equation (2.3.1)] for isotropic scattering is modified by

$$k_t \frac{\partial I_{j,k}^m}{\partial t} = - \left( \mu_m \frac{\partial I_{j,k}^m}{\partial x} + \eta_m \frac{\partial I_{j,k}^m}{\partial y} + \xi_m \frac{\partial I_{j,k}^m}{\partial z} \right) + \left( \kappa_p + (\kappa_g)_{j,k} \right) a_{j,k} I_b - \left( \kappa_p + (\kappa_g)_{j,k} + \sigma_p \right) I_{j,k}^m + \frac{\sigma_p}{4\pi} \sum_{m'=1}^M w_{m'} I_{j,k}^{m'} \quad (3.2.1)$$

The indices  $j$  and  $k$  denote the  $j^{\text{th}}$  and  $k^{\text{th}}$  grey gas for  $\text{H}_2\text{O}$  and  $\text{CO}_2$ , respectively. It has been shown by Denison and Webb [58] that the joint grey gas weights are well approximated by the product of the two individual weights:

$$a_{j,k} = a_j \cdot a_k \quad (3.2.2)$$

The grey gas weights  $a_j, a_k$  are calculated through absorption-line blackbody distribution functions,  $F_s$ , derived from high-resolution HITRAN database [59]. Denison and Webb provided simple mathematical correlations for absorption-line blackbody distributions functions for  $\text{H}_2\text{O}$  and  $\text{CO}_2$ , respectively [23, 60].

The absorption coefficients  $(\kappa_g)_{j,k}$  are given as the sum of contributions of the two species [61]

$$(\kappa_g)_{j,k} = N_w \cdot C_{abs,w,j} + N_c \cdot C_{abs,c,k} \quad (3.2.3)$$

where  $N_w$  and  $N_c$  are the molar densities,  $C_{abs,w,j}$  and  $C_{abs,c,k}$  are absorption cross-sections of  $\text{H}_2\text{O}$  and  $\text{CO}_2$ , respectively.

In the present study, radiation code based on MOL solution of DOM with SLW developed by Selçuk and her coworkers [48,49] was used. Further details of the code can be found in [48, 49].

### 3.3 Statistical Narrow-Band Correlated-K Model

The basis point of Correlated-K (CK) methods is that for any radiative quantity  $\phi_\nu$  that is solely dependent on gas absorption coefficient the integration over wavenumber can be replaced by integration over the absorption coefficient

$$\bar{\phi}_\nu = \frac{1}{\Delta\nu} \int_{\Delta\nu} \phi(\kappa_\nu) d\nu = \int_0^\infty f(k) \phi(k) dk \quad (3.3.1)$$

where

$$f(k) = \frac{1}{\nu} \frac{d\nu}{dk} \quad (3.3.2)$$

is the normalized distribution function of the gas absorption coefficient inside  $\Delta\nu$  and  $f(k)dk$  represents the fraction of wavenumber inside  $\Delta\nu$  where the gas absorption coefficient lies between  $k$  and  $k + dk$ . Note that when the integration over wavenumber is replaced by integration over the gas absorption coefficient, the spectral gas absorption coefficient  $\kappa_\nu$  is denoted by  $k$  since it now plays the role of an independent variable and is no longer a function of wavenumber. Application of Equation (4.3.1) to gas transmissivity leads to [62]

$$\bar{\tau}_\nu(L) = \int_0^\infty f(k) \exp(-kL) dk \quad (3.3.3)$$

In the SNB model, the gas transmissivity over an isothermal and homogeneous path is given as [31]

$$\bar{\tau}_\nu(L) = \left[ -\frac{\pi B}{2} \left( \sqrt{1 + \frac{4SL}{\pi B}} - 1 \right) \right] \quad (3.3.4)$$

where  $B = 2\bar{\beta}_v/\pi^2$ ,  $S = \bar{k}_v X p$ ,  $L$  is the path length,  $X$  is the mole fraction of the radiating gas,  $p$  is the pressure,  $\bar{k}_v$  is the mean line-intensity to spacing ratio,  $\bar{\beta}_v = 2\pi\bar{\gamma}/\bar{\delta}_v$  is the mean line width to spacing ratio,  $\bar{\gamma}$  is the mean collision half-width of an absorption line and  $\bar{\delta}_v$  is the equivalent line spacing. In this study,  $\bar{k}_v$  and  $\bar{\delta}_v$  are taken from Soufiani and Taine [63] and from Riviere and Soufiani [64].  $\bar{\gamma}$  for H<sub>2</sub>O, CO<sub>2</sub>, and CO are given by [65]

$$\bar{\gamma}_{H_2O} = \frac{p}{p_s} \left\{ 0.462 X_{H_2O} \left( \frac{T_s}{T} \right) + \left( \frac{T_s}{T} \right)^{0.5} [0.079(1 - X_{CO_2} - X_{O_2}) + 0.106 X_{CO_2} + 0.036 X_{O_2}] \right\} \quad (3.3.5)$$

$$\bar{\gamma}_{CO_2} = \frac{p}{p_s} \left( \frac{T_s}{T} \right)^{0.7} \{ 0.07 X_{CO_2} + 0.058(1 - X_{CO_2} - X_{H_2O}) + 0.1 X_{H_2O} \} \quad (3.3.6)$$

$$\bar{\gamma}_{CO} = \frac{p}{p_s} \left\{ 0.075 X_{CO_2} \left( \frac{T_s}{T} \right)^{0.6} + 0.12 X_{H_2O} \left( \frac{T_s}{T} \right)^{0.82} + 0.06 \left( \frac{T_s}{T} \right)^{0.7} (1 - X_{CO_2} - X_{H_2O}) \right\} \quad (3.3.7)$$

with  $p_s$  and  $T_s$  are equal to 1 atm and 296 K, respectively.

By inverse Laplace transformation of the SNB gas transmissivity given in Equation (4.3.4),  $f(k)$  can be expressed as [61]

$$f(k) = \frac{1}{2} k^{-3/2} (BS)^{1/2} \exp \left[ \frac{\pi B}{4} \left( 2 - \frac{S}{k} - \frac{k}{S} \right) \right] \quad (3.3.8)$$

with a peak value at

$$k_{max} = \left( \frac{3\bar{k}_v}{\pi B} \right) \left( \sqrt{\left( \frac{\pi B}{3} \right)^2 + 1} - 1 \right) \quad (3.3.9)$$

The cumulative function  $g(k)$  is defined as

$$g(k) = \int_0^k f(k') dk' \quad (3.3.10)$$

which is a monotonically increasing function from 0 to 1. By using Equation (3.3.8) and Equation (3.3.10), the analytical expression of  $g(k)$  are given by [65]

$$g(k) = \frac{1}{2} \left[ 1 - \operatorname{erf} \left( \frac{a}{\sqrt{k}} - b\sqrt{k} \right) \right] + \frac{1}{2} \left[ 1 - \operatorname{erf} \left( \frac{a}{\sqrt{k}} + b\sqrt{k} \right) \right] e^{\pi B} \quad (3.3.11)$$

where  $a = \frac{1}{2} \sqrt{\pi B S}$ ,  $b = \frac{1}{2} \sqrt{\pi B / S}$  and  $\operatorname{erf}(x)$  is the error function.

Using the cumulative function  $g$ , the narrow-band average of any radiative variable dependent solely on the gas absorption coefficient  $\Phi_v$  can be evaluated as

$$\bar{\Phi}_v = \frac{1}{\Delta v} \int_{\Delta v} \phi(\kappa_v) dv = \int_0^1 \phi(g) dg \quad (3.3.12)$$

Equation (3.3.12) can be conveniently calculated using a Gauss quadrature scheme

$$\bar{\Phi}_v = \sum_{i=1}^N w_i \phi(g_i) \quad (3.3.13)$$

where  $N$  is the number of quadrature points. The 7-point Gauss-Labatto quadrature was selected due to its accuracy and computationally efficiency [63]. Table 3.1 summarizes the weight parameters,  $w_i$ , and the quadrature point,  $g_i$ , of the 7-point Gauss-Labatto quadrature scheme.

The absorption coefficient  $k_i$  corresponding to the  $i$ th quadrature point  $g_i$  is obtained by inversion of the cumulative distribution function given in Equation (3.3.11).  $k(g_i)$  can be found numerically by using a Newton-Raphson iteration method with a few iterations when  $k_{\max}$  given in Equation (3.3.9) is used as the initial value of  $k$ , as suggested by Lacis and Oinas [65]. Detailed description of SNBCK can be found elsewhere [65].

Table 3.1. The 7-point Gauss-Labatto quadrature scheme

<b>i</b>	<b><math>g_i</math></b>	<b><math>w_i</math></b>
1	0.00000	0.04500
2	0.15541	0.24500
3	0.45000	0.32000
4	0.74459	0.24500
5	0.90000	0.05611
6	0.93551	0.05125
7	0.98449	0.03764

In this study, the absorption coefficient of gas mixture for a given spectral band is evaluated by summation of each individual gaseous species absorption coefficient due to accuracy and CPU times [62].

### 3.3.1 Structure and Operation of the Computer Code SNBCK

In the present work, the SNBCK code was developed to evaluate radiative properties of gases. Figure 3.1 displays the flow diagram of the computer code. The general steps of the computer code are as follows:

1. Define mole fraction of H<sub>2</sub>O, CO<sub>2</sub>, and CO,  $p_s$ ,  $T_s$  and  $w_i$  and  $g_i$  of the 7-point Gauss-Labatto quadrature scheme.
2. Read in input data as  $\bar{k}_\nu$  and  $\bar{\delta}_\nu$  for H<sub>2</sub>O, CO<sub>2</sub>, and CO as a function of temperature and wavenumber.
3. Calculate the mean collision half-width of an absorption line ( $\bar{\gamma}$ ) for considered absorbing gas (H<sub>2</sub>O, CO<sub>2</sub>, or CO) by using Equations (3.3.5-3.3.7).
4. Evaluate  $k_{max}$  by using Equation (3.3.9) and it is used as the initial value of  $k_i$ .

5. Calculate cumulative distribution function ( $g(k)$ ) given in Equation (3.3.11) and its derivatives for Newton-Raphson iteration method
6. Calculate new value of  $k_i$  by using Newton-Raphson iteration method.
7. Check for convergence by comparing the solutions at current step with those at previous step. If current solution is within the specified range of the previous solution (absolute error is less than  $10^{-6}$ ), converge is established.
8. If convergence is not established, save the solution for convergence check and go to step 5.
9. If convergence is established, print  $k_i$  as a function of temperature, wavenumber and 7-point Gauss-Labatto quadrature scheme to output files.
10. Repeat steps 5-9 for all Gauss-Labatto quadrature points.
11. Repeat steps 3-10 for all temperature, all wavenumber and all considered absorbing gases.

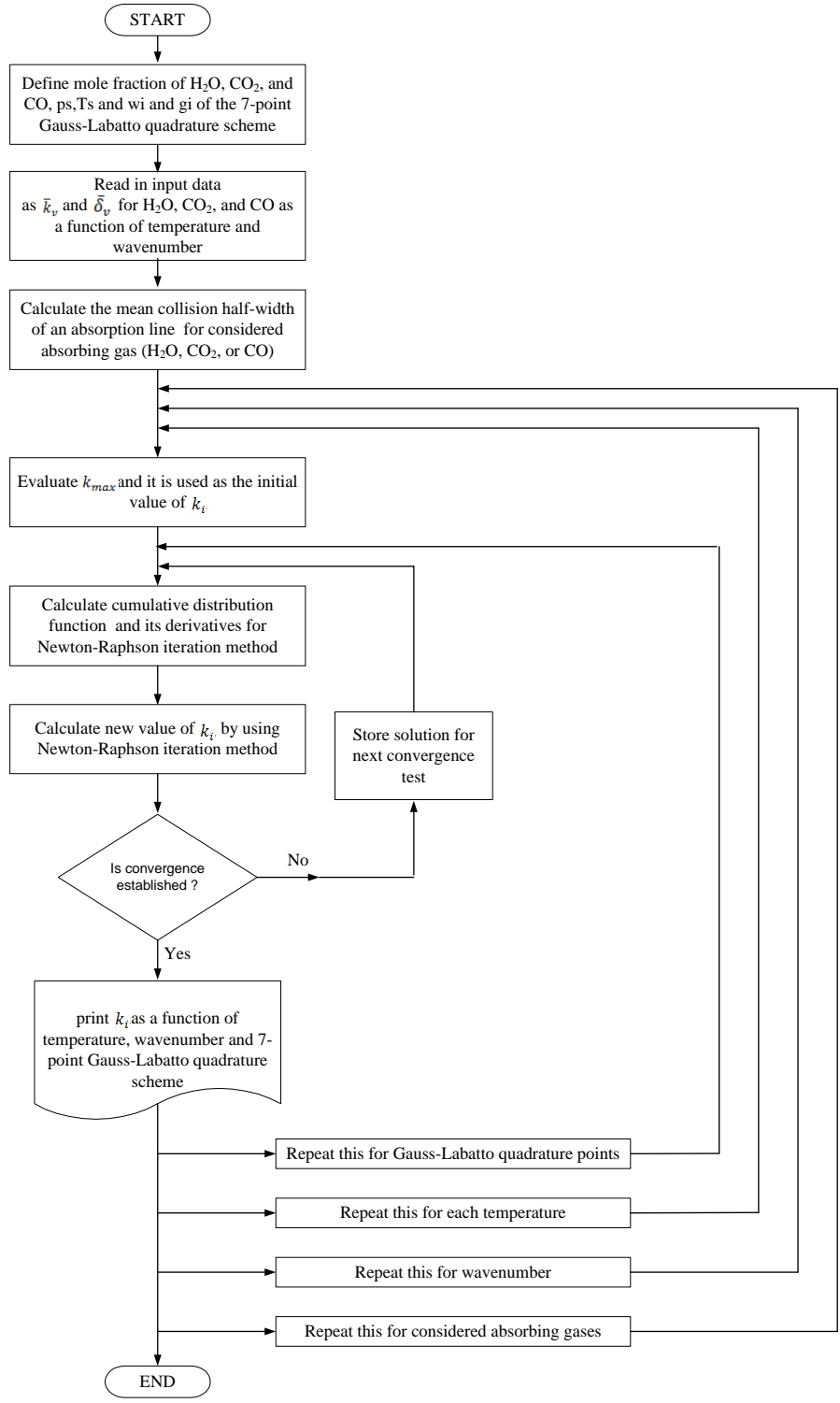


Figure 3.1. Flowchart of SNBCK



### 3.4 Mie Theory

Radiative properties of particles are generally calculated by using the Mie scattering theory for spheres with specified size (larger than  $\lambda$ ) and complex refractive index ( $m = n - ik$ ). The size parameter,  $x$ , is defined as

$$x = \frac{2\pi a}{\lambda} \quad (3.4.1)$$

where  $a$  is the radius of the spherical particles and  $\lambda$  is the wavelength.

The amount of scattering and absorption by a particle is expressed in terms of the scattering cross-section,  $C_{sca}$ , and absorption cross-section,  $C_{abs}$ . The total amount of absorption and scattering (extinction) is expressed in terms of the extinction cross-section

$$C_{ext} = C_{abs} + C_{sca} \quad (3.4.2)$$

By using Mie theory, scattering cross-section,  $C_{sca}$ , and extinction cross-section,  $C_{ext}$  are evaluated as

$$C_{sca} = \frac{2\pi a^2}{x^2} \sum_{n=1}^{\infty} (2n+1) (|a_n|^2 + |b_n|^2) \quad (3.4.3)$$

$$C_{ext} = \frac{2\pi a^2}{x^2} \sum_{n=1}^{\infty} (2n+1) \text{Re}\{a_n + ab_n\} \quad (3.4.4)$$

where the Mie scattering coefficient  $a_n$  and  $b_n$  are complex functions of  $x$  and  $y = mx$ ,

$$a_n = \frac{\psi'_n(y)\psi_n(x) - m\psi_n(y)\psi'_n(x)}{\psi'_n(y)\xi_n(x) - m\psi_n(y)\xi'_n(x)} \quad (3.4.5)$$

$$b_n = \frac{m\psi'_n(y)\psi_n(x) - \psi_n(y)\psi'_n(x)}{m\psi'_n(y)\xi_n(x) - \psi_n(y)\xi'_n(x)} \quad (3.4.6)$$

The function  $\psi_n$  and  $\xi_n$  are known as Ricatti-Bessel functions and related to Bessel and Hankel functions by [44]

$$\psi_n(z) = \left(\frac{\pi z}{2}\right)^{1/2} J_{n+1/2}(z), \quad \xi_n(z) = \left(\frac{\pi z}{2}\right)^{1/2} H_{n+1/2}(z) \quad (3.4.7)$$

In this study, radiative properties of particles were calculated using the BHMIE code based on Mie theory [66]. In the code, the logarithmic derivative,  $D_n$ , is used to evaluate the Mie scattering coefficient  $a_n$  and  $b_n$ .

$$D_n(z) = \frac{d}{dz} \ln \psi_n(z) \quad (3.4.8)$$

Equations (3.4.5) and (3.4.6) can be rewritten as

$$a_n = \frac{[D_n(y)/m+n/x]\psi_n(x) - \psi_{n-1}(x)}{[D_n(y)/m+n/x]\xi_n(x) - \xi_{n-1}(x)} \quad (3.4.9)$$

$$b_n = \frac{[mD_n(y)+n/x]\psi_n(x) - \psi_{n-1}(x)}{[mD_n(y)+n/x]\xi_n(x) - \xi_{n-1}(x)} \quad (3.4.10)$$

where the recurrence relations is used as

$$\psi'_n(x) = \psi_{n-1}(x) - \frac{n\psi_n(x)}{x}, \quad \xi'_n(x) = \xi_{n-1}(x) - \frac{n\xi_n(x)}{x} \quad (3.4.11)$$

to eliminate  $\psi'_n$  and  $\xi'_n$ . The logarithmic derivative satisfies the recurrence relation

$$D_{n-1} = \frac{n}{z} - \frac{1}{D_n + \frac{n}{z}} \quad (3.4.12)$$

$D_n(y)$  in Equations (3.4.9) and (3.4.10) is computed by the downward recurrence relation between Eq. (3.4.12) beginning with  $D_{\text{NMX}}$ .

In BHMIE, series are terminated after NSTOP terms, where NSTOP is the integer closest to  $x + 4x^{1/3} + 2$  and NMX is taken to be  $Max(NSTOP, |y|) + 15$  and  $D_{NMX}$  is begun with  $0.0 + i0.0$ .

Both  $\psi_n$  and  $\xi_n (= \xi\psi_n - i\chi_n)$  satisfy

$$\psi_{n+1}(x) = \frac{2n+1}{x}\psi_n(x) - \psi_{n-1}(x) \quad (3.4.13)$$

and are computed by this upward recurrence relation beginning with

$$\psi_{-1}(x) = \cos x, \quad \psi_0(x) = \sin x, \quad \chi_{-1}(x) = -\sin x, \quad \chi_0(x) = \cos x \quad (3.4.14)$$

Detailed description of BHMIE code can be found elsewhere [66]. In the present work, BHMIE code based on Mie theory [66] was modified to provide wavelength dependent scattering and extinction cross-section. Moreover, calculation of asymmetry factor,  $g$ , was added into BHMIE code to evaluate scattering phase function approximated by the Henyey-Greenstein function as [44].

$$g = \frac{4\pi a^2}{x^2 C_{sca}} \sum_{n=1}^{\infty} \left[ \frac{n(n+2)}{n+1} Re\{a_n a_{n+1}^* + b_n b_{n+1}^*\} + \frac{2n+1}{n(n+1)} Re\{a_n b^*\} \right] \quad (3.4.15)$$

### 3.4.1 Structure and Operation of the Computer Code BHMIE

Figure 3.2 shows the flow diagram of the computer code. The general steps of the computer code are as follows:

1. Define complex reflective index, radius of particle, wavelengths.
2. Calculate size parameter and NSTOP and NMX.
3. Initialize scattering cross-section and extinction cross-section as 0.
4. Calculate logarithmic derivative by using Equation (3.4.12).

5. Calculate Ricatti-Bessel functions by using Equations (3.4.13) and (3.4.14).
6. Calculate Mie scattering coefficient  $a_n$  and  $b_n$  by using Equations (3.4.9) and (3.4.10).
7. Calculate scattering cross-section, extinction cross-section and asymmetry factor by using Equations (3.4.3), (3.4.4) and (3.4.15).
8. If NSTOP is not reached, scattering cross-section is equal to summation of current scattering cross-section and previous one ; extinction cross-section is equal to summation of current extinction cross-section and previous one; and asymmetry factor is equal to summation of current asymmetry factor and previous one, go to 4.
9. If NSTOP is reached, evaluate scattering cross-section, extinction cross-section, and asymmetry factor.
10. Write scattering cross-section, extinction cross-section and asymmetry factor.
11. Repeat steps 2-10 for all wavelengths.

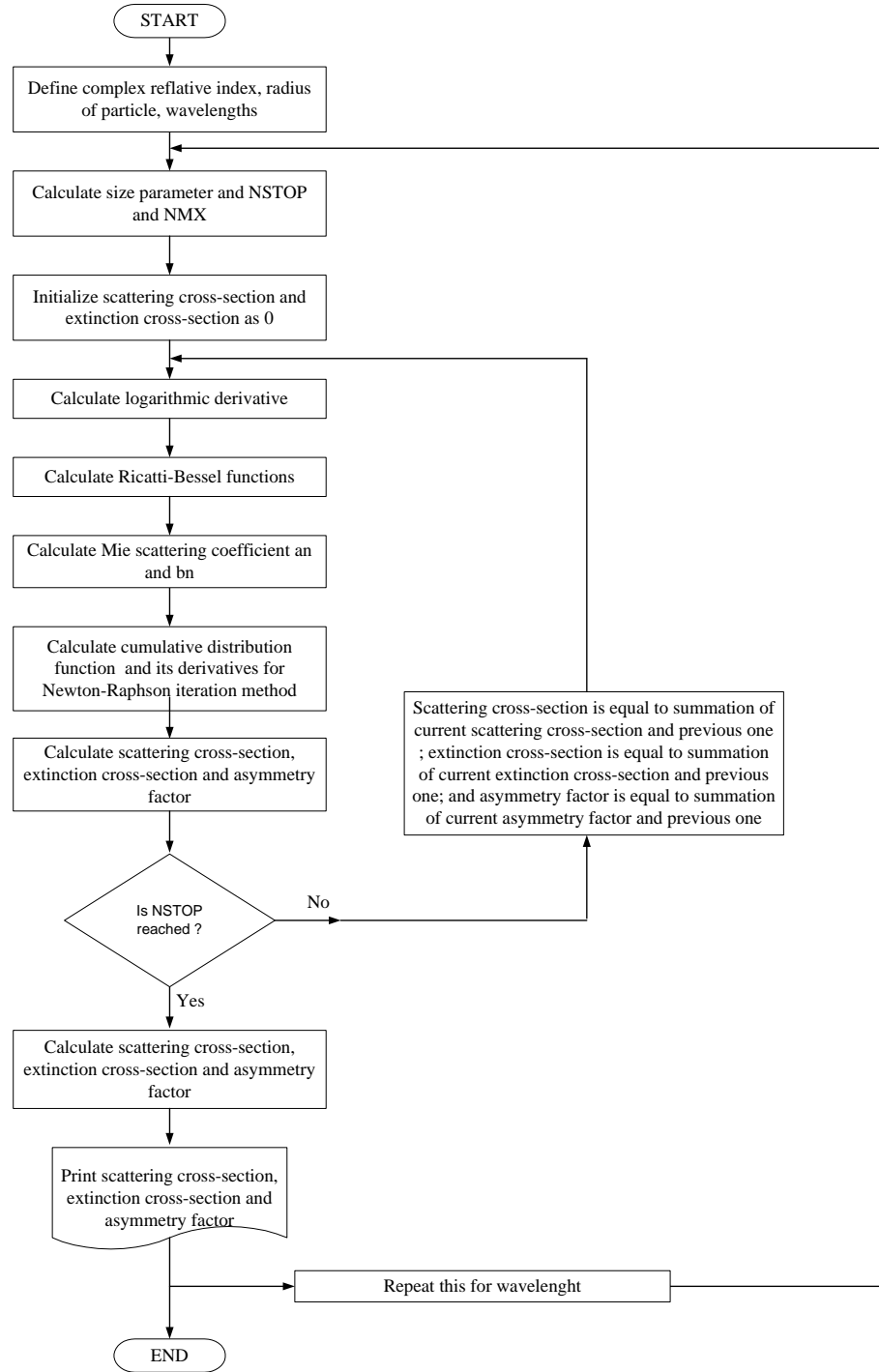


Figure 3.2. Flowchart of BHMIE



## CHAPTER 4

### RESULTS

In this chapter, selection of RTE solution technique for CFD solver and the radiation code, selection of radiative property estimation technique for CFD solver and the radiation code, validation of CFD solver with SLW, validation of the radiation code and exhaust plume simulations for non-aluminized/aluminized propellant cases are presented.

#### **4.1 Selection of RTE Solution Technique**

To select RTE solution technique for CFD solver and the radiation code, the predictive accuracy and computationally efficiency of DOM,  $P_1$  and IDA were investigated by applying the methods to four cubical test problems shown in Figure 4.1 and comparing their predictions with benchmark solutions available in the literature. This study is published in [67].

Simulations were carried out on a personal computer with Pentium 4 2.80 GHz processor having 1.5 GB of RAM.

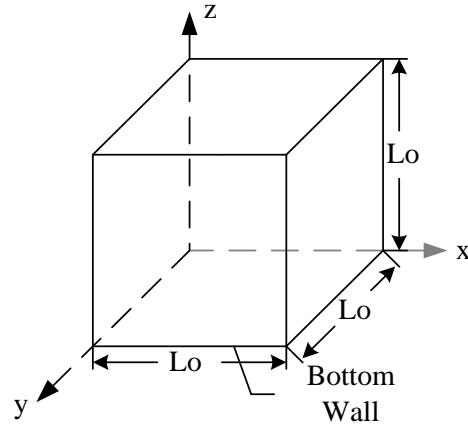


Figure 4.1. Schematic representation of the system under consideration.

#### 4.1.1 Purely Isotropically Scattering Medium and Non-Symmetric Boundary Conditions

Physical system under consideration for this problem is a 3-D cubical enclosure ( $L_0 = 1$  m) containing uniform, grey, purely isotropically scattering medium confined within diffuse black walls. Only bottom wall (at  $z=0$ ) is at emissive power such that  $\sigma T^4 / \pi = 1$ . The temperature of the other walls and the medium are taken as 0 K. The medium is characterized by optical thickness equal to unity. The enclosure is divided into  $30 \times 30 \times 30$  control volumes.

Performances of DOM and IDA with  $S_8$ ,  $S_{10}$  and  $T_4$  quadratures for this problem were assessed by comparing their predictions for radiative heat flux  $q_z$  along the centerline of the enclosure ( $L_0/2, L_0/2, z$ ) with benchmark solution provided by Tan and Hsu [68].

Comparisons are shown in Figure 4.2. As can be seen from the figure,  $P_1$  leads to overprediction of radiative heat flux. Heat flux predictions obtained from DOM with  $S_8$ ,  $S_{10}$  and  $T_4$  quadratures are found to be in good agreement with the benchmark solution, while those of IDA with  $S_8$ ,  $S_{10}$  and  $T_4$  quadratures are found to oscillate due to ray effects. The average absolute errors are illustrated in Table 4.1. As can be seen from the table, for DOM,  $S_8$  quadrature leads to more accurate and computationally efficient



results, whereas for IDA,  $T_4$  quadrature provides more accurate solutions with less CPU times. Therefore,  $S_8$  quadrature for DOM (DOM  $S_8$ ) and  $T_4$  quadrature for IDA (IDA  $T_4$ ) were utilized in the rest of the present study.

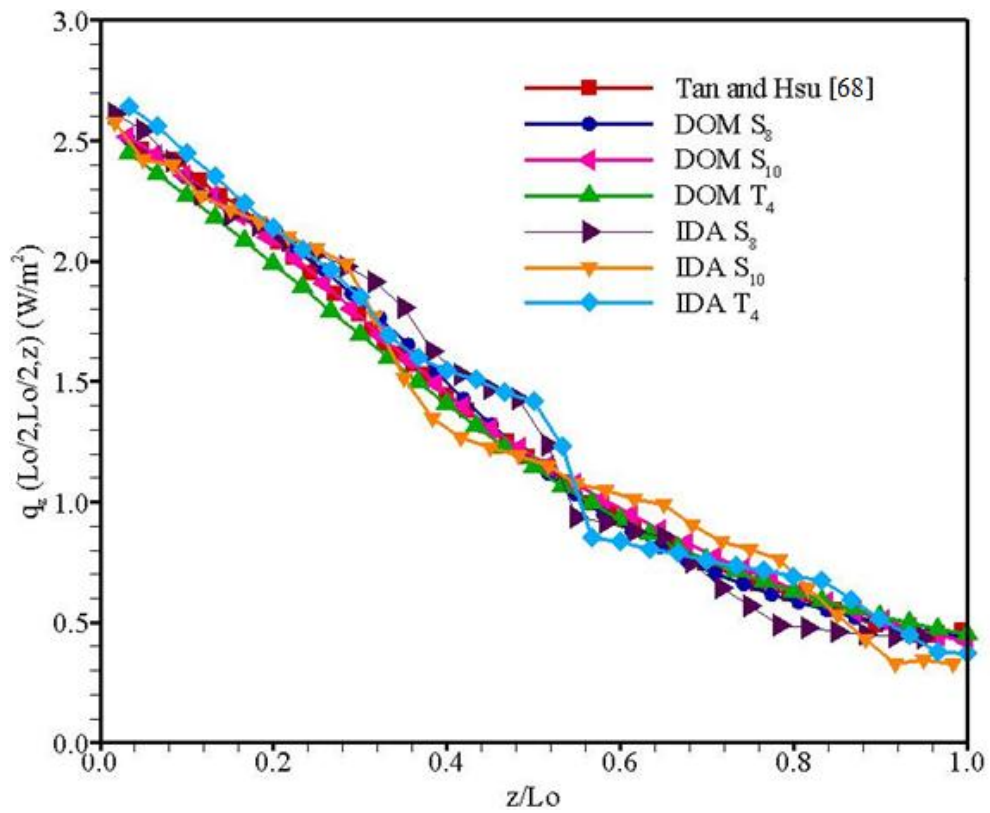


Figure 4.2. Effect of angular discretization on the radiative heat flux predictions along the centerline of the enclosure for DOM and IDA.

Table 4.1. Average percentage errors in the radiative heat flux predictions along the centerline of the enclosure with CPU times for different angular quadrature schemes

Model	Angular Quadrature Scheme	Average Absolute % Error <sup>1</sup>	CPU Times (s)
DOM	S <sub>8</sub>	2.49	15.81
	S <sub>10</sub>	2.73	28.63
	T <sub>4</sub>	3.72	36.75
P <sub>1</sub>	-	25.01	22.39
IDA	S <sub>8</sub>	8.24	93.86
	S <sub>10</sub>	9.10	82.39
	T <sub>4</sub>	5.83	85.33

<sup>1</sup>Absolute % Error = (|predicted-benchmark| / benchmark) × 100

#### 4.1.2 Absorbing-Emitting-Scattering Medium and Non-Symmetric Boundary Conditions

The second case is a 3-D cubical enclosure ( $L_0 = 1$  m) containing uniform, grey, absorbing-emitting-isotropically scattering medium with black boundaries. Only bottom wall (at  $z = 0$ ) is at emissive power such that  $\sigma T^4 / \pi = 1$ . The temperature of the other walls and the medium are taken as 0 K. The optical thickness and albedo of the medium are 0.1 and 0.5, respectively. Uniform grid structure of  $30 \times 30 \times 30$  is utilized.

Figure 4.3 shows radiative heat flux  $q_z$  along the centreline of the enclosure ( $L_0/2, L_0/2, z$ ). The solutions of DOM S<sub>8</sub>, P<sub>1</sub> and IDA T<sub>4</sub> are compared with benchmark solution provided by Tan and Hsu [68]. As can be seen from the figure, P<sub>1</sub> results in overprediction of radiative heat flux with an average absolute error of 68.07 % and CPU time of 150.96 seconds. Radiative heat flux calculated by IDA T<sub>4</sub> oscillates considerably with an average absolute error of 9.93 % and CPU time of 215.14 seconds. DOM S<sub>8</sub>

leads to more accurate and computationally efficient results with an average absolute error of 4.96 % in radiative heat flux and CPU time of 6.08 seconds.

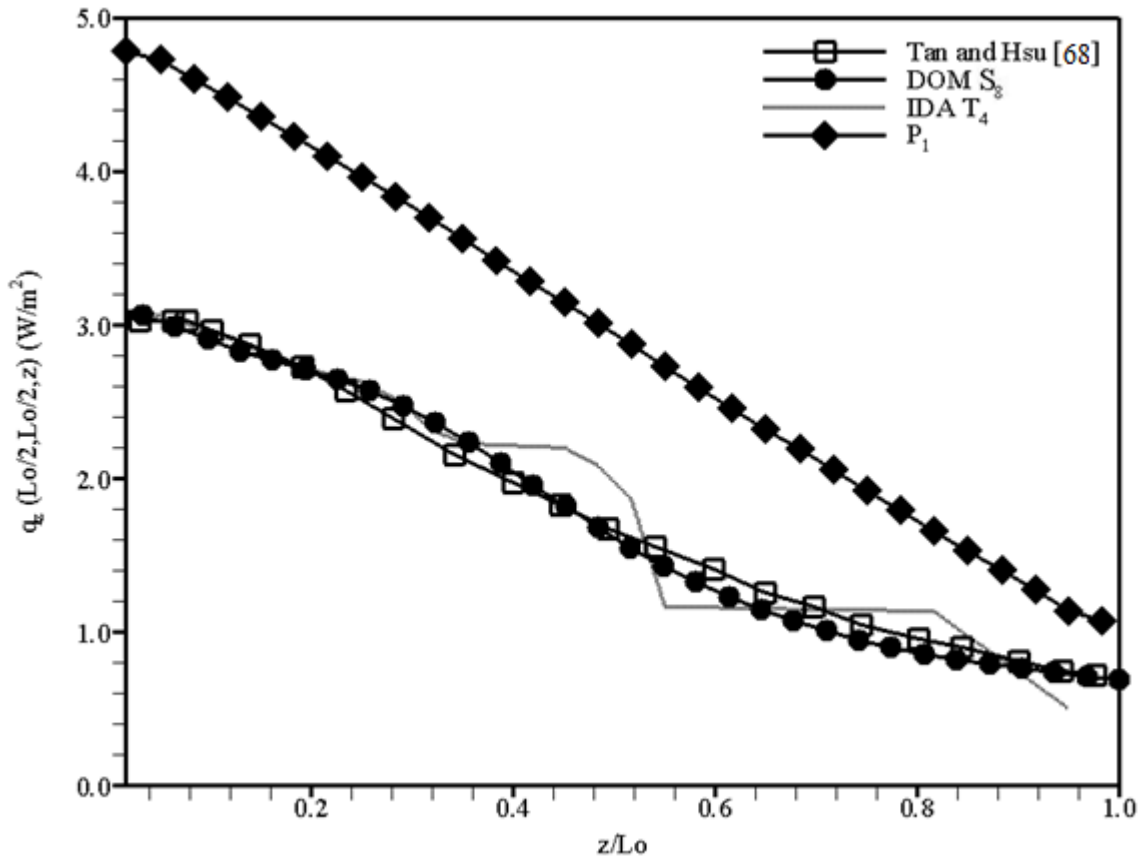


Figure 4.3. Comparison between the radiative heat flux predictions along the centreline of the enclosure for DOM  $S_8$ ,  $P_1$  and IDA  $T_4$ .

### 4.1.3 Absorbing-Emitting-Isotropically Scattering Medium and Symmetric Boundary Conditions

In this case, a cubical enclosure with the side length ( $L_o$ ) of 1 m containing a grey, absorbing-emitting-isotropically scattering medium at a uniform temperature of 648 K is considered. The walls of the enclosure are cold at 0 K.

DOM S<sub>8</sub>, P<sub>1</sub> and IDA T<sub>4</sub> were implemented on the test problem by using various extinction coefficients (1, 2, and 10 m<sup>-1</sup>) with  $\omega=0.5$  and uniform grid resolutions (25×25×25, 30×30×30 and 45×45×45). The performances of the methods were tested by comparing their predicted dimensionless radiative heat flux  $Q_z^*$  along the centerline of a wall (x, L<sub>o</sub>/2, L<sub>o</sub>) with those of MC method provided by Kim and Huh [69]. The dimensionless radiative heat flux is defined as

$$Q_z^* = \frac{q_z}{\sigma T_{med}^4} \quad (5.1.1)$$

where  $T_{med}$  is the medium temperature and  $\sigma$  represents Stefan-Boltzmann constant.

Figure 4.4 shows the comparison between the dimensionless radiative heat flux predictions of the methods. As can be seen, the dimensionless heat flux predicted by DOM S<sub>8</sub> is found to be in excellent agreement with the benchmark solution for all extinction coefficients and grid resolutions. Moreover, the predictions obtained from P<sub>1</sub> and IDA T<sub>4</sub> for  $\beta=1 \text{ m}^{-1}$  and  $2 \text{ m}^{-1}$  are in good agreement with the benchmark solution for all grid resolutions, whereas both methods lead to underprediction of the dimensionless heat flux for  $\beta=10 \text{ m}^{-1}$ .

Average absolute percentage errors in the radiative heat flux predictions along the centerline of a wall and corresponding CPU times are tabulated in Table 4.2. As can be seen from the table, P<sub>1</sub> produces less accurate heat flux prediction with the lowest execution time requirement for all extinction coefficients and grid resolutions. Average percentage errors obtained from DOM S<sub>8</sub> do not improve significantly with the grid resolution for all extinction coefficients. For  $\beta=1 \text{ m}^{-1}$  and  $2 \text{ m}^{-1}$ , DOM S<sub>8</sub> results are found to be more accurate with less CPU times than those of IDA T<sub>4</sub>. For  $\beta=10 \text{ m}^{-1}$ , DOM S<sub>8</sub> and IDA T<sub>4</sub> are found to require the same order of magnitude CPU time with IDA T<sub>4</sub> leading to an order of magnitude higher error at the same grid resolution 25x25x25. For the same average absolute percentage error, IDA T<sub>4</sub> requires a finer grid resolution (45x45x45) with an order of magnitude higher CPU time. The computational

time of geometry calculation for IDA  $T_4$  is about 40 % of the total calculation time. In order to find the effect of CPU time spent for geometry calculation on the total CPU time, this calculation was carried out once and stored as binary format for  $\beta=10 \text{ m}^{-1}$ . This resulted in a decrease of total CPU time by almost half for all grid resolutions. However, for the same accuracy obtained from DOM  $S_8$  with  $25 \times 25 \times 25$  and IDA  $T_4$  with  $45 \times 45 \times 45$ , DOM  $S_8$  results are found to be more computationally efficient.

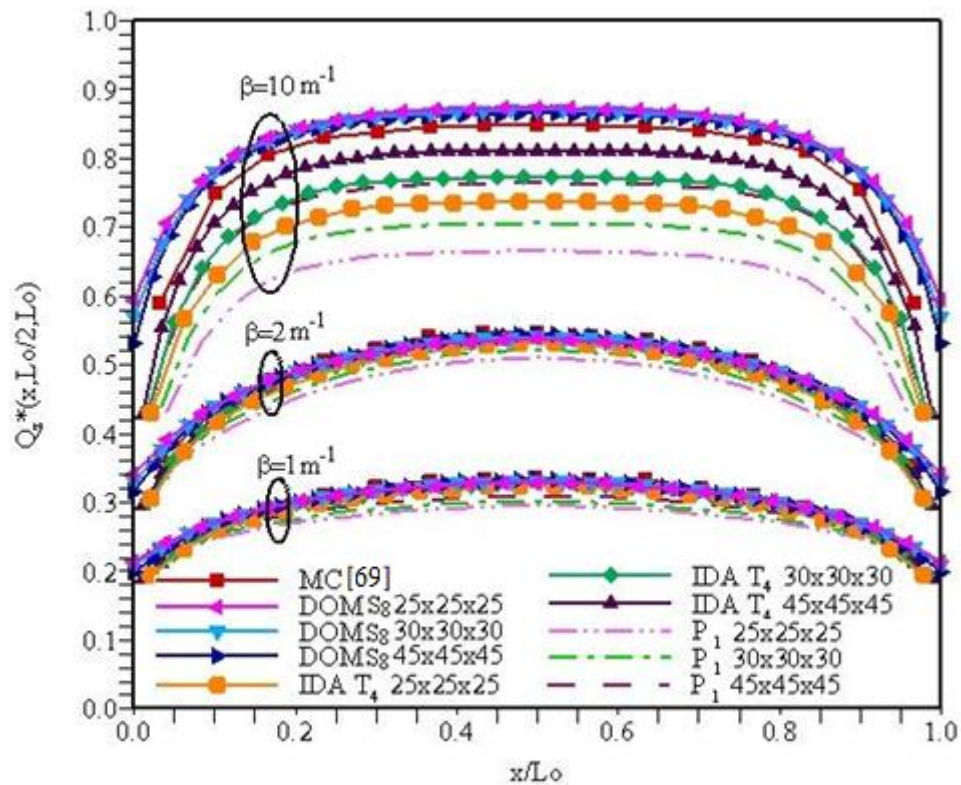


Figure 4.4. Comparison between the radiative heat flux predictions of DOM  $S_8$ ,  $P_1$  and IDA  $T_4$  for different extinction coefficients.

Table 4.2. Average percentage errors in the radiative heat flux predictions along the centerline of a wall with CPU times for different extinction coefficients and uniform grid resolutions

Extinction coefficient ( $m^{-1}$ )	Model	Grid resolutions	Average Absolute % Error <sup>2</sup>	CPU time (s)		
				P <sub>1</sub>	Geometry	Total
1	DOM S <sub>8</sub>	25×25×25	2.27	-	-	44.75
		30×30×30	1.96	-	-	84.53
		45×45×45	1.49	-	-	268.68
	P <sub>1</sub>	25×25×25	9.11	9.81	-	9.81
		30×30×30	7.08	21.67	-	21.67
		45×45×45	6.31	179.41	-	179.41
	IDA T <sub>4</sub>	25×25×25	3.42	9.81	22.95	61.35
		30×30×30	2.68	21.67	44.65	123.17
		45×45×45	1.91	179.41	159.93	523.50
2	DOM S <sub>8</sub>	25×25×25	3.79	-	-	54.21
		30×30×30	1.51	-	-	102.25
		45×45×45	1.04	-	-	355.20
	P <sub>1</sub>	25×25×25	7.30	6.95	-	6.95
		30×30×30	4.95	12.16	-	12.16
		45×45×45	2.38	99.71	-	99.71
	IDA T <sub>4</sub>	25×25×25	3.39	6.95	26.07	62.37
		30×30×30	2.37	12.16	46.33	116.57
		45×45×45	1.23	99.71	148.04	427.10
10	DOM S <sub>8</sub>	25×25×25	4.26	-	-	82.71
		30×30×30	3.77	-	-	158.90
		45×45×45	3.04	-	-	497.32
	P <sub>1</sub>	25×25×25	23.06	1.05	-	1.05
		30×30×30	17.97	1.43	-	1.43
		45×45×45	10.57	16.56	-	16.56
	IDA T <sub>4</sub>	25×25×25	14.09	1.05	25.56	59.79
		30×30×30	9.53	1.43	46.64	108.53
		45×45×45	4.52	16.56	156.38	402.40

<sup>2</sup> Absolute % Error =  $(|\text{predicted-MC}| / \text{MC}) \times 100$

#### **4.1.4 Purely Linearly Anisotropically Scattering Medium and Symmetric Boundary Conditions**

In the last case, the medium is a 3-D cubical enclosure ( $L_0 = 1$  m) containing uniform, grey, purely linearly anisotropically scattering medium confined within diffuse black walls. Only bottom wall (at  $z=0$ ) is at emissive power such that  $\sigma T^4 / \pi = 1$ . Other walls and the medium are cold at 0 K. The optical thickness and albedo of the medium are 1 and 1, respectively. The coefficient of linear anisotropy of scattering is taken as 1. The enclosure is divided into uniform  $33 \times 33 \times 33$  and  $45 \times 45 \times 45$  control volumes.

Performances of DOM  $S_8$ ,  $P_1$  and IDA  $T_4$  for this problem were tested by comparing their predictions for radiative heat flux  $q_z$  along the centerlines of bottom (AB Line) and the top walls (CD Line) as well as  $q_x$  along the centerline of side wall (BC Line) (illustrated in Figure 4.1) with those of Radiative Integral Transfer Equation (RITE) solutions provided by Altaç and Tekkalmaz [70]. For the bottom and side walls, comparisons obtained for grid resolution  $45 \times 45 \times 45$  are shown in Figure 4.5. As can be seen from the figure,  $P_1$  results in overprediction of radiative heat flux for both walls. Heat flux predictions obtained from DOM  $S_8$  are found to be in agreement with the benchmark solution, while those of IDA  $T_4$  are found to oscillate due to ray effects. The average absolute errors are tabulated in Table 4.3. Overall comparisons show that DOM  $S_8$  leads to more accurate solutions with an order of magnitude lower CPU time compared to IDA  $T_4$ .

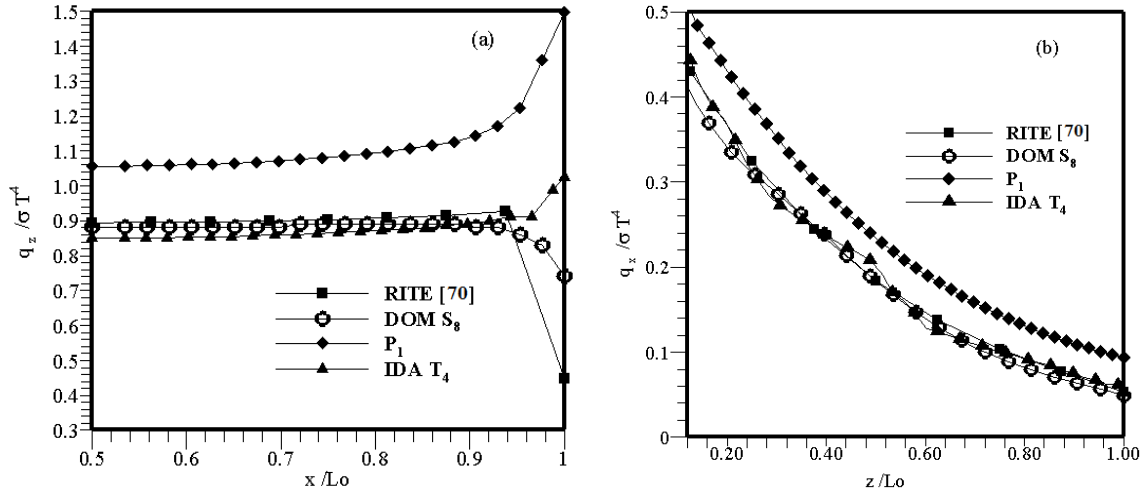


Figure 4.5. Comparison between the radiative heat flux predictions (a)  $q_z$  along AB Line (b)  $q_x$  along BC Line of DOM  $S_8$  and IDA  $T_4$  for grid resolution  $45 \times 45 \times 45$ .

Table 4.3. Average percentage errors in the radiative heat flux predictions along AB Line, BC Line and CD Line with CPU times for different uniform grid resolutions

Model	Grid resolutions	Average Absolute % Error			CPU time (s)
		AB Line $q_z / \sigma T^4$	BC Line $q_x / \sigma T^4$	CD Line $q_z / \sigma T^4$	
DOM $S_8$	$33 \times 33 \times 33$	4.10	8.76	6.04	73.93
	$45 \times 45 \times 45$	2.32	8.16	4.63	189.54
$P_1$	$33 \times 33 \times 33$	21.58	35.51	5.53	23.61
	$45 \times 45 \times 45$	29.95	37.12	20.42	87.26
IDA $T_4$	$33 \times 33 \times 33$	18.59	5.29	19.34	242.46
	$45 \times 45 \times 45$	19.94	5.89	19.71	1089.27



Overall comparisons show that DOM S<sub>8</sub> produces higher accuracy and computational efficiency than IDA T<sub>4</sub> on all test problems under consideration. Therefore, DOM is selected as RTE solution technique for CFD solver and the radiation code.

## **4.2 Selection of Radiative Property Estimation Technique**

In order to verify the sensitivity of the radiative property estimation technique, SNBCK, to RTE solutions, a different test case, freeboard of an Atmospheric Bubbling Fluidized Bed Combustor (ABFBC) containing CO<sub>2</sub>, H<sub>2</sub>O and fly ash particles with a size distribution, was selected. The second reason for the choice of this test problem was the availability of measurements of incident radiative fluxes on the side walls of the enclosure. Finally, the third reason was the availability of incident fluxes predicted by the MOL solution of DOM with SLW [49]. However, solutions of MOL solution of DOM with SNBCK for particle laden combustion gases in freeboard of fluidized bed combustors are not available to date.

For this purpose, a three-dimensional radiation code based on the MOL solution of DOM with SNBCK and geometric optics approximation was developed. Predictive accuracy and computationally efficiency of the MOL solution of DOM coupled with different radiative property estimation techniques (GG, SLW, SNBCK models) were assessed by applying them to the prediction of incident radiative fluxes along the freeboard walls of a 0.3 MWt ABFBC and comparing their predictions with measurements generated previously from two runs one without and the other with recycle. Freeboard is treated as a three-dimensional rectangular enclosure containing a grey/non-grey, absorbing-emitting-isotropically scattering medium [71].

### **4.2.1 Description of Test Rig**

The main body of the test rig is the modular combustor formed by five modules of internal cross-section of 0.45 m×0.45 m and 1 m height. Inner walls of the modules are lined with alumina based refractory bricks and insulated. The first and fifth modules

from the bottom refer to bed and cooler, respectively, and the ones in between are the freeboard modules. There exist two cooling surfaces in the modular combustor, one in the bed and the other in the cooler providing  $0.35 \text{ m}^2$  and  $4.3 \text{ m}^2$  of cooling surfaces, respectively. There are 14 ports for thermocouples and 10 ports for gas sampling probes along the combustor. Two ports for feeding coal/limestone mixture are provided in the bed module, one 0.22 m, the other 0.85 m above the distributor plate.

In order to measure concentrations of  $\text{O}_2$ ,  $\text{CO}$ ,  $\text{CO}_2$ ,  $\text{SO}_2$ ,  $\text{NO/NO}_x$  along the combustor at steady state, combustion gas is sampled from the combustor and passed through gas conditioning system where the sample is filtered, dried and cooled to be fed to the analyzer. The process values such as flow rates and temperatures of each stream, gas composition and temperature along the combustor are logged to a PC by means of a data acquisition and control system, Bailey INFI 90. Further details of the test rig can be found elsewhere [72].

Radiative heat fluxes incident on the refractory side-walls of the freeboard were measured by water cooled radiometer with Medtherm 48P-20-22K heat flux transducer during the steady state operation of the test rig. Details of transducer are available elsewhere [73]. The radiometer eliminates the effects of convection and measures only the incident radiative heat flux. The radiometer probe was inserted into the gas sampling ports at five different heights along freeboard flush with the inner surface of the refractory side-wall. The radiometer output for incident radiative heat flux was read by using Medtherm H-201 digital heat flux meter with certified calibration.

Radiative heat flux measurements were carried out in two combustion tests, one without and the other with recycle of fine particles. Experiments were carried out with typical low calorific value and high ash content Turkish lignite, namely Beypazari lignite. Table 4.4 lists some of the operating conditions for these runs at steady state. It is worth noting at this point that freeboard fly ash particle load, reported in the table, is taken as the sum of particles collected by cyclone and baghouse. Particle load determination in the test

with recycle needs further elaboration of the recycling system of the combustor under consideration as follows. Cyclone catch particles pass through an air lock (i.e., a rotary valve) and fall onto a diverter. Depending on the position of the diverter, particles are either discharged from the system to a continuously weighted ash storage bin (load cell) for experiments without recycle or flow back to the combustor for re-firing. The fraction of a short time interval over which the position of the diverter remains on the recycle mode determines the recycle ratio. Continuity of flow is provided by repeating this time interval periodically. In order to provide a wider range of recycle ratio and yet not to disturb the steady state conditions within the combustor, a periodic time interval of 10 s was selected. For experiment with recycle (run 2), the diverter remains nine units of time on the recycle mode and one unit of time on no recycle mode. Cyclone flow rate (26.58 kg/h) shows the flow rate of particles in no recycle mode for one unit of time, which gives the recycle flow rate when multiplied by 9. Recycle flow rate of 239.22 kg/h leads to an order of magnitude increase in particle loading (from 0.011–0.131 kg/m<sup>3</sup>) as shown in Table 4.4 and used in the calculation of incident fluxes. Further experimental details of the runs can be found in [72].

For radiative property estimation of particle-laden combustion gases, particles collected from both cyclone and baghouse downstream of the freeboard were subjected to particle size distribution analysis by laser light scattering technique. Additive rule is applied to obtain actual size distribution in the freeboard which is indicated in Figure 4.6 for both runs. Temperature measurements were carried out on a discrete grid of points along the freeboard at steady state operation. In order to facilitate the use of these measurements as input data in the calculation of radiative exchange, the experimental data were represented by high order polynomials given in Table 4.5.

Table 4.4. Operating conditions of the 0.3 MWt ABFBC

	<b>Run 1</b> <b>Without recycle</b>	<b>Run 2</b> <b>With recycle</b>
<b>Superficial velocity, m/s</b>	3.0	2.80
<b>Coal flow rate, kg/h</b>	101	101
<b>Carryover flow rate, kg/h</b>	23.65	26.58
<b>Baghouse filter flow rate, kg/h</b>	1.08	3.43
<b>Recycle ratio*, -</b>	0.00	2.37
<b>Particle load, kg/m<sup>3</sup></b>	0.0115	0.1307
<b>Average bed temperature, K</b>	1148	1119
<b>Average freeboard temperature, K</b>	1120	1178
<b>Average H<sub>2</sub>O concentration, %</b>	10	10
<b>Average CO<sub>2</sub> concentration, %</b>	10	11

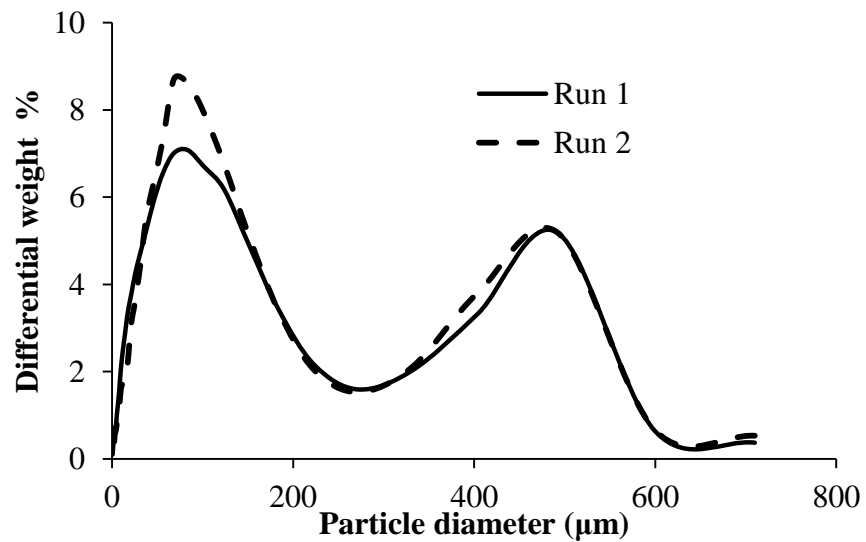


Figure 4.6. Particle size distributions for runs with and without recycle.

Table 4.5. Polynomials for temperature profiles

	<b>Run 1</b>	<b>Run 2</b>
<p><b>Gas temperature profile, K</b></p> $T_g(z) = \sum_{i=0}^6 a_i z^i$	$a_0 = 1164.00$ $a_1 = -124.40$ $a_2 = 198.70$ $a_3 = -111.60$ $a_4 = 26.97$ $a_5 = -2.47$ $a_6 = 0.00$	$a_0 = 1114.20$ $a_1 = -18.49$ $a_2 = -37.83$ $a_3 = 80.49$ $a_4 = -38.22$ $a_5 = 7.65$ $a_6 = -0.61$
<p><b>Wall temperature profile, K</b></p> $T_w(z) = \sum_{i=0}^5 b_i z^i$	$b_0 = 1147.20$ $b_1 = 53.60$ $b_2 = -106.70$ $b_3 = 69.68$ $b_4 = -17.43$ $b_5 = 1.35$	$b_0 = 1112.20$ $b_1 = 192.10$ $b_2 = -318.96$ $b_3 = 209.66$ $b_4 = -56.24$ $b_5 = 4.93$

#### 4.2.2 Treatment of Freeboard

In order to apply the radiation model to the freeboard, it is required to provide temperatures and radiative properties of the surfaces and the medium. The freeboard section of the combustor is treated as a 3-D rectangular enclosure containing grey/non-grey absorbing-emitting-isotropically scattering medium bounded by diffuse, grey/black walls. The physical system and the treatment of the freeboard are schematically illustrated in Figure 4.7. The side walls are taken as grey, diffuse walls ( $\epsilon_w = 0.33$ ). The cooler boundary at the top, which consists of gas lanes and cooler tubes, is represented by an equivalent grey surface of effective emissivity ( $\epsilon_w = 0.87$ ) related to area weighted average emissivity of the components. Details of the treatment of tube-

row/gas-lane combination can be found elsewhere [73]. The boundary with the bed section at the bottom is represented as a black surface due to Hohlraum effect [73].

Final step in the preparation of the input data is the estimation of radiative properties of the particle laden combustion gases consisting of CO<sub>2</sub>, H<sub>2</sub>O and fly ash particles bounded by the freeboard walls. Its radiative properties are assumed to be uniform and constant throughout the freeboard. This assumption is based on uniform CO<sub>2</sub> and H<sub>2</sub>O concentrations measured along the freeboard and the fact that particle concentration and size distribution can be represented by the material sampled from the cyclone and the baghouse filter [74].

The radiative properties of the participating combustion gases are estimated by using GG, SLW, SNBCK models briefly described in Chapter 3. Radiative properties of the cloud of fly ash particles depend on the composition, size distribution and particle loading. The ash content of the fly ash particles determined by chemical analysis was 98% indicating that the fly ash can be treated as pure ash in the radiative property estimation. The complex refractive index of fly ash particles ( $m=n-ik$ ) was defined by using real index ( $n$ ) and absorption index ( $k$ ). The spectral dependence of complex index of refraction is neglected and a representative value of  $m=1.5-0.02i$  is used as given in [75]. Independent scattering is assumed to take place in the freeboard of the test rig as the particle volume fraction is in the order of  $10^{-5}$ . The size parameter is determined by using a representative wavelength (3  $\mu\text{m}$ ) suggested for combustion systems in [40] and the actual size distribution of fly ash particles in the freeboard. Radiative properties of fly ash particles are evaluated by geometric optics approximation and illustrated with mass distribution function,  $m(D_p)$ , in Table 4.6. Further details of radiative properties of fly ash particle can be found in [49].

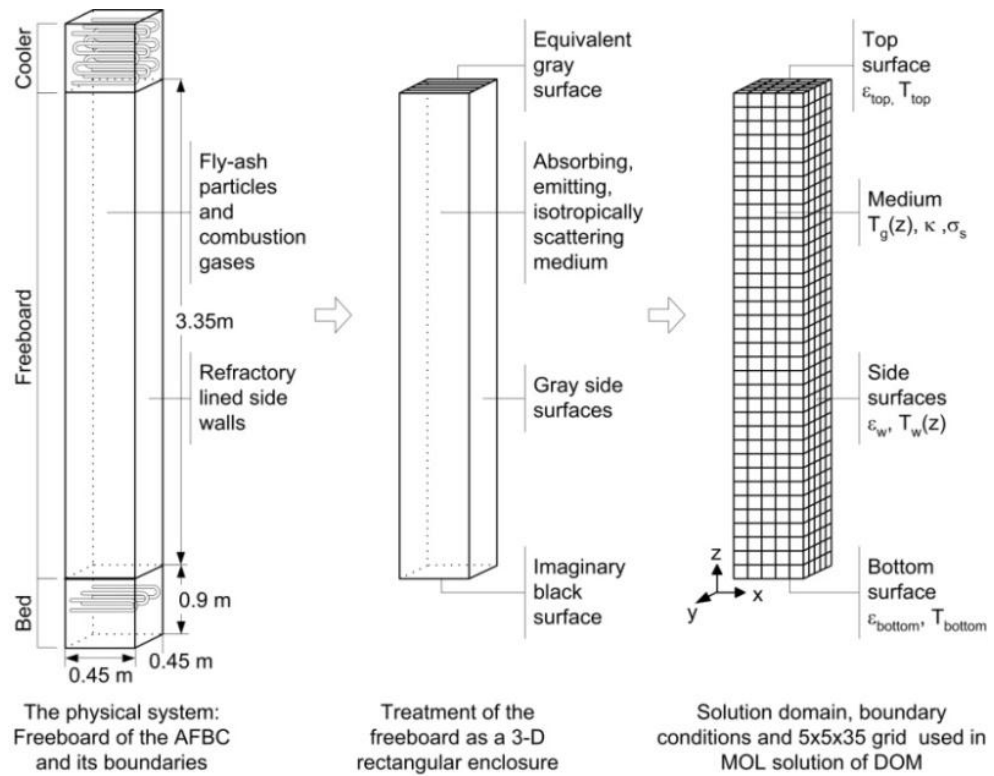


Figure 4.7. Treatment of freeboard for radiation model

Table 4.6. Radiative properties of fly ash particles in the freeboard

	Run 1	Run 2
$m(D_p)$ , $\text{kg/m}^3 \mu\text{m}$	$7.935 \times 10^{-4}$	$7.972 \times 10^{-3}$
$\kappa_p$ , $\text{m}^{-1}$	15.220	155.960
$\sigma_p$ , $\text{m}^{-1}$	0.634	7.204

### 4.2.3 Comparisons between Model Predictions and Measurements

In the present work, for the implementation of the DOM, the  $S_N$  angular quadrature scheme proposed by Carlson and Lathrop [51] was selected. The choice is based on an assessment study carried out by Selçuk and Kayakol [13]. A combination of  $S_4$  order of approximation and  $5 \times 5 \times 35$  grid structure, found to provide accurate and efficient solutions in a previous grid refinement study [76], was utilized. For the difference relations of spatial derivatives, three-point upwind differencing scheme DSS014, assessed previously for accuracy [42, 47] was employed. The ODE solver utilized is ROWMAP which is based on the ROW-methods of order 4 and uses Krylov techniques for the solution of linear systems. Simulations were carried out on a personal computer with Pentium 4 2.80 GHz processor having 1.5 GB of RAM.

In the present study, radiation code based on MOL solution of DOM with SLW model developed by Selçuk and her coworkers [48, 49] was used. Totally 10 grey gases for SLW model were utilized. Further details of the code are available elsewhere [44, 45].

Figure 4.8 shows comparison between incident heat fluxes predicted by MOL solution of DOM coupled with GG, SLW, and SNBCK and measurements for both runs. As can be seen from the figure, predictions obtained from all models are in good agreement with measurements except at the uppermost port for Run 1. The lower measured heat flux at this location is considered to be due to lower particle loading and/or lower temperature conditions in Run 1 compared to those of Run 2.



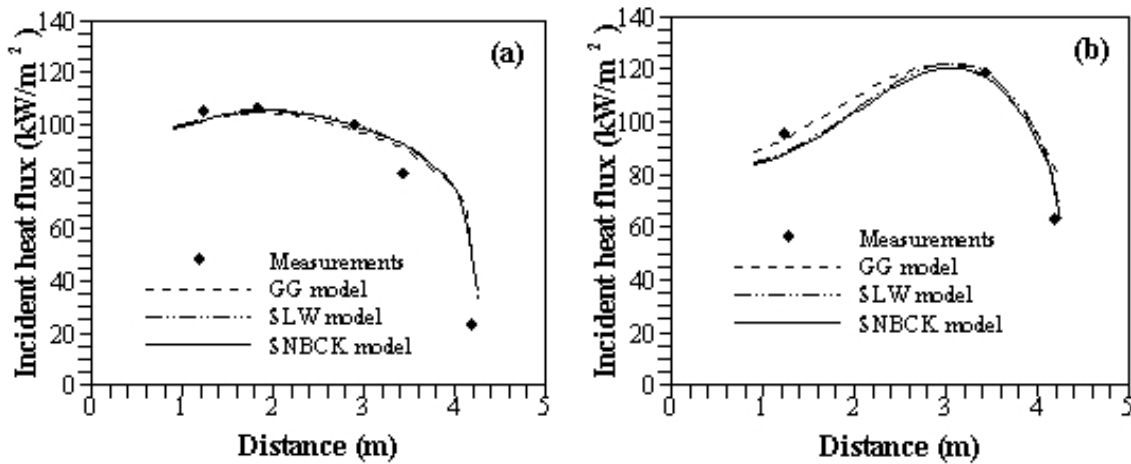


Figure 4.8. Comparisons between model predictions and measurements results of experimental studies for a) Run 1 and b) Run 2

The absolute percentage error in the incident flux predictions along the centerline of the wall and corresponding CPU times for Run 1 and Run 2 are tabulated in Table 4.7 and Table 4.8, respectively. As can be seen from the tables, absolute percentage errors obtained by the models are of the same order of magnitude for both runs. However, GG model is found to require an order of magnitude lower CPU time than SLW model and five order of magnitude lower CPU time than SNBCK model.

Table 4.7. Comparison between predicted and measured incident heat fluxes with CPU times for Run 1

Height (m)	Measurements (kW/m <sup>2</sup> )	Predictions (kW/m <sup>2</sup> )			Absolute % Error <sup>3</sup>		
		GG	SLW	SNBCK	GG	SLW	SNBCK
1.23	105.00	101.75	101.79	101.43	3.10	3.06	3.40
1.83	106.30	104.54	105.68	105.28	1.66	0.58	0.96
2.91	100.00	97.7	99.76	99.38	2.30	0.24	0.62
3.44	81.3	90.32	92.32	91.95	11.09	13.55	13.10
4.19	22.50	33.03	36.68	35.97	46.80	63.02	59.87
<b>CPU Time (s)</b>	-	1.64	55.80	69802.32			

<sup>3</sup>Absolute % Error = (|predicted-measured|/measured) x100

Table 4.8. Comparison between predicted and measured incident heat fluxes with CPU times for Run 2

Height (m)	Measurements (kW/m <sup>2</sup> )	Predictions (kW/m <sup>2</sup> )			Absolute % Error		
		GG	SLW	SNBCK	GG	SLW	SNBCK
1.23	95.00	93.36	88.22	87.33	1.73	7.14	8.07
3.44	118.80	117.02	118.69	116.58	1.50	0.09	1.87
4.19	62.50	63.29	61.49	62.69	1.26	1.62	0.30
<b>CPU Time (s)</b>	-	2.08	75.96	63679.81			

Despite the fact that there is good agreement between the wall fluxes predicted by all models under consideration, it was considered necessary to investigate the source term predictions to be used in the solution of energy conservation equation in CFD codes. Figure 4.9 illustrates the comparison between the source term distributions predicted by MOL solution of DOM with GG, SLW and SNBCK along the centerline of the freeboard for both runs. It is worth noting that the source term profiles predicted by all models are found to follow similar trend to the temperature profiles, as physically expected. For comparative testing purposes, source term distribution obtained by SNBCK is taken as reference solution due to its accuracy. As can be seen from the figure, the predictions obtained from SLW are in good agreement with those of SNBCK with average percentage error of 8.68 for Run 1 and average percentage error of 18.56 for Run 2. GG model leads to underprediction of the source term distribution with average percentage error of 16.19 for Run 1 and average percentage error of 24.94 for Run 2. This is in agreement with finding of Johansson et al. [77].

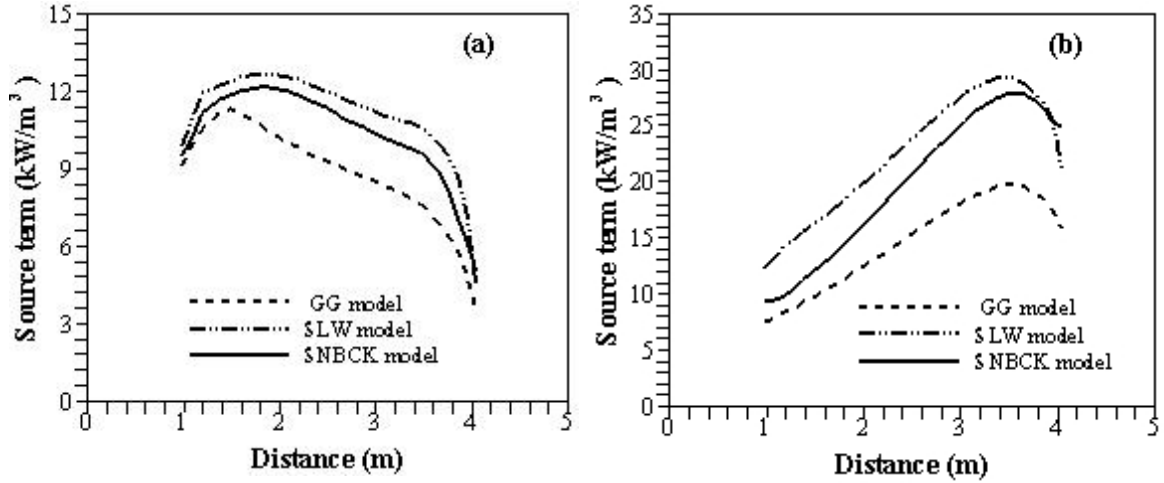


Figure 4.9. Comparisons between the source term distribution predictions of GG, SLW, and SNBCK along the centerline of the freeboard for a) Run 1 and b) Run 2

From the viewpoints of accuracy and computationally economy, SLW is selected as radiative property estimation technique for CFD solver due to fact that it produces accurate solutions with less CPU times and SNBCK is chosen as radiative property estimation technique for the radiation code as it is highly accurate and wavelength dependent technique.

### 4.3 Validation of ANSYS FLUENT with SLW

ANSYS FLUENT which is the most frequently used commercial CFD solver for computational fluid dynamics coupled with radiative heat transfer, deploys DOM for RTE solver and grey WSGG for radiative property estimation of gases. In ANSYS FLUENT, correlations of Smith et al. [78] are utilized to evaluate the total emissivity of H<sub>2</sub>O/CO<sub>2</sub> mixture in grey WSGG, and then a grey absorption coefficient based on the total emissivity and mean beam length of an enclosure is evaluated by using Beer's law for DOM. The implementation of grey WSGG in the CFD solver is expected to be less accurate compared to that of non-grey radiative property estimation techniques [79]. Moreover, in the correlations evaluated by Smith et al., partial pressure ratios of water vapor to carbon dioxide were taken as 2 or 1 which are only convenient for the air and

gaseous fuel combustion, but not for oxy-fuel combustion which is gaining increasing interest worldwide as one of the promising carbon capture and storage (CCS) technologies. Therefore modeling of radiative heat transfer in the CFD solver necessitates an accurate and computationally efficient non-grey radiative property estimation technique for all combustion environments. To achieve this objective, accuracy of different non-grey WSGG [79-84] and Full-Spectrum k-distribution (FSK) method [85] were tested by comparing their predictions against those of grey WSGG, all coupled with ANSYS FLUENT for different test cases. These studies imply that non-grey gas radiative properties are necessary when modeling air-fuel, oxy-fuel, or oxy-enriched combustion. The drawback of grey/non-grey WSGG is the need for specific set of coefficients at pressure path lengths and ratios of H<sub>2</sub>O and CO<sub>2</sub> to calculate absorption coefficients [77]. This leads to the use of more general non-grey radiative property estimation techniques in CFD solver for all applications. SLW model proposed by Denison and Webb [57, 58, 60, 61] meets all these requirements. Implementation of SLW method in ANSYS FLUENT is not available to date.

In the present study, SLW model was implemented to ANSYS FLUENT v.13.0, as radiative property estimation technique for gases by User Defined Function (UDF). Totally 10 grey gases for SLW model with calculations of radiative properties of non grey gas were utilized. DOM in ANSYS FLUENT was used as RTE solver. Predictive accuracy of ANSYS FLUENT with SLW was tested by applying it to three benchmark problems, two containing isothermal homogenous/non-homogenous water vapor and one isothermal water vapor/carbon dioxide mixture. In order to make use of tabulated data from MOL of DOM with SLW developed by Selçuk and Doner [48], ANSYS FLUENT with SLW results were compared with those data in all test cases. While benchmarking ANSYS FLUENT with SLW, results of RT with SNB [86] were also used in the first two test cases. MOL of DOM with SLW developed by Selçuk and Doner [48] was used for benchmarking the last test case.

Angular discretization schemes used for ANSYS FLUENT and MOL solution of DOM for 3-D problems in the present work are summarized in Table 4.9. The detail of angular discretization schemes are given in Section 2.6.

Table 4.9. Number of ordinates used for quadratures

<b>Code</b>	<b>Angular Quadrature Scheme</b>	<b>Order of Approximation (N)</b>	<b>Number of ordinates per octant</b>	<b>Total number of ordinates</b>
<b>FLUENT</b>	$N_\theta \times N_\phi$	2x2	4	32
		8x8	64	512
<b>MOL solution of DOM</b>	$S_N$	$S_4$	3	24
		$S_6$	6	48
		$S_8$	10	80

The benchmark problem is a rectangular enclosure of 2m x 2m x 4m containing absorbing-emitting and non-scattering gases at a uniform temperature of 1000 K and surrounded by black walls at 300 K [86]. Identical grid structures, that is, spatial discretization, as those of benchmark problems are utilized in order to enable point by point comparison.

#### 4.3.1 Isothermal and Homogenous Medium of H<sub>2</sub>O

Test case 1 refers to a medium of pure water vapor at a uniform temperature of 1000 K. Uniform grid resolution of 11 x 11 x 16 was deployed. Absorption coefficients ( $\kappa_j$ ) and their associated weights ( $a_j$ ) obtained from ANSYS FLUENT and MOL solution of DOM are illustrated in

Table 4.10. As can be seen from the table, radiative properties obtained from ANSYS FLUENT are found to be in good agreement with those of MOL solution of DOM with average absolute error of  $6.35 \times 10^{-3}$  % for absorption coefficients and average absolute error of  $5.41 \times 10^{-5}$  % for their associated weights.

Table 4.10. Absorption coefficients ( $\kappa_j$ ) and their associated weights ( $a_j$ ) obtained from FLUENT and MOL solution of DOM for test case 1

Grey Gases	FLUENT-SLW		MOL-SLW	
	$\kappa_j$	$a_j$	$\kappa_j$	$a_j$
1	0.000819	0.043033	0.000819	0.043033
2	0.004104	0.066420	0.004104	0.066420
3	0.020573	0.101662	0.020574	0.101662
4	0.103136	0.154413	0.103142	0.154413
5	0.517041	0.212762	0.517074	0.212762
6	2.592027	0.215722	2.592194	0.215721
7	12.994330	0.123079	12.995170	0.123079
8	65.143100	0.032454	65.147299	0.032454
9	326.574900	0.003388	326.595998	0.003388
10	0.000000	0.047064	0.000000	0.047064

Comparisons between incident heat fluxes predicted by the present study and those of MOL solution of DOM with SLW and RT with SNB [86] along the centerline ( $x = 2m$ ,  $y = 1m$ ,  $z$ ) and ( $x, y = 1m, z = 4m$ ) are illustrated in Figure 4.10. Incident heat fluxes obtained by RT with SNB are taken as reference solution due to its accuracy. As can be seen from the figure, predictions of ANSYS FLUENT with SLW are found to be in good agreement with those of MOL solution of DOM and the reference solutions. The maximum and average absolute errors and corresponding CPU times are illustrated in Table 4.11. As can be seen from the table, absolute percentage errors obtained by the models are of the same order of magnitude for both directions. Therefore, 2x2

quadrature for FLUENT and  $S_4$  quadrature for MOL solution of DOM were utilized in the rest of the present study due to CPU efficiency.

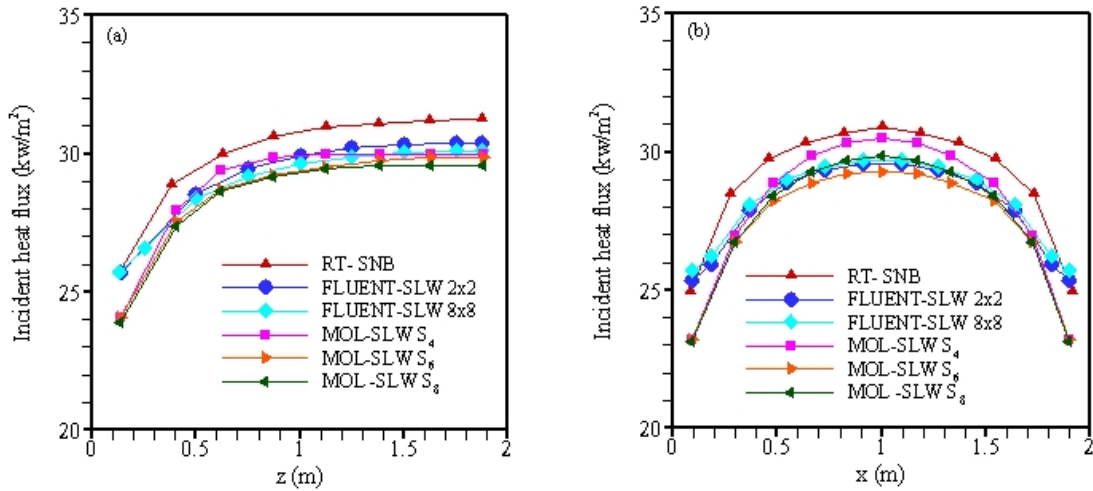


Figure 4.10. Comparison between incident heat flux predictions of present study and MOL solution of DOM with SLW and RT with SNB for test case 1 : (a) along ( $x = 2\text{m}$ ,  $y = 1\text{m}$ ,  $z$ ) and (b) along ( $x$ ,  $y = 1\text{m}$ ,  $z = 4\text{m}$ )

Table 4.11. Absorption coefficients ( $\kappa_j$ ) and their associated weights ( $a_j$ ) obtained from FLUENT and MOL solution of DOM for test case 1

Model of approximation	Maximum Absolute % Relative Error <sup>4</sup>		Average Absolute % Relative Error		CPU Times (s)
	z-Direction	x-Direction	z-Direction	x-Direction	
FLUENT-SLW 2x2	4.40	5.56	2.77	3.77	643
FLUENT-SLW 8x8	4.57	4.72	3.46	3.60	24960
MOL-SLW S <sub>4</sub>	6.56	5.56	3.66	3.76	180
MOL-SLW S <sub>6</sub>	6.49	8.18	4.73	5.83	248
MOL-SLW S <sub>8</sub>	7.15	8.34	5.23	5.01	415

<sup>4</sup>Absolute % Error =  $(|\text{predicted}-\text{RT with SNB}| / \text{RT with SNB}) \times 100$

### 4.3.2 Isothermal and Non-Homogenous Medium of H<sub>2</sub>O

In the second test case, the medium is a non-uniform mixture of water vapor and nitrogen with the mole fraction of water vapor changing along the z-direction according to formulation by  $(z-0.25z^2)$ . The gas temperature remains uniform at 1000K. Uniform grid resolution of 11 x 11 x 25 was utilized.

Figure 4.11 displays comparisons between incident heat fluxes along  $(x = 2\text{m}, y = 1\text{m}, z)$  and  $(x, y = 1\text{m}, z = 4\text{m})$ . As can be seen from the figure, predictions obtained from ANSYS FLUENT with SLW are in good agreement with those of MOL solution of DOM with SLW and RT with SNB. The maximum and average absolute percentage errors are tabulated in Table 4.12. As can be seen from the table, absolute percentage errors obtained by ANSYS FLUENT with SLW are of the same order of magnitude as those of MOL solution of DOM with SLW for both directions.

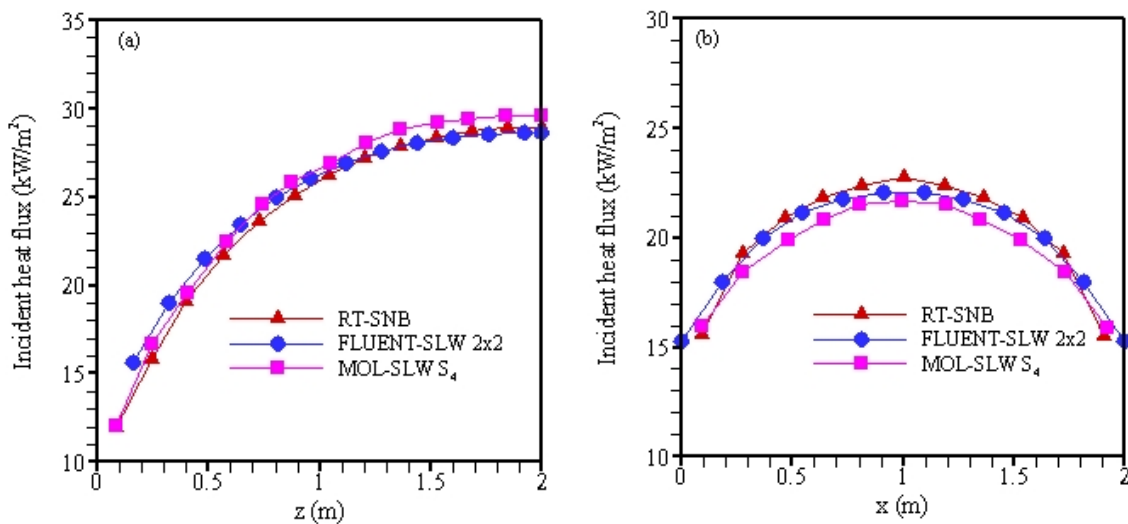


Figure 4.11. Comparison between incident heat flux predictions of present study and MOL solution of DOM with SLW and RT with SNB for test case 1 : (a) along  $(x = 2\text{m}, y = 1\text{m}, z)$  and (b) along  $(x, y = 1\text{m}, z = 4\text{m})$



Table 4.12. Maximum and average absolute percentage errors in the incident heat flux predictions along the centerline ( $x = 2\text{m}$ ,  $y = 1\text{m}$ ,  $z$ ) and ( $x$ ,  $y = 1\text{m}$ ,  $z = 4\text{m}$ ) for test case 2

Model of approximation	Maximum Absolute % Relative Error <sup>5</sup>		Average Absolute % Relative Error	
	z-Direction	x-Direction	z-Direction	x-Direction
FLUENT-SLW 2x2	10.22	6.77	3.22	3.25
MOL-SLW S <sub>4</sub>	5.51	5.20	3.10	3.83

<sup>5</sup> Absolute % Error =  $(|\text{predicted-RT with SNB}| / \text{RT with SNB}) \times 100$

### 4.3.3 Isothermal and Homogenous Medium of H<sub>2</sub>O-CO<sub>2</sub> Mixture

In the last test case, the medium is assumed to be a mixture of 10% CO<sub>2</sub>, 20% H<sub>2</sub>O and 70% N<sub>2</sub> on a molar basis at a uniform temperature of 1000 K. Uniform grid structure of 11 x 11 x 16 was used. 10 grey gases (5 grey gases for CO<sub>2</sub> and 5 grey gases for H<sub>2</sub>O) are utilized. Table 4.13 gives absorption coefficients ( $\kappa_{j,k}$ ) and their associated weights ( $a_{j,k}$ ) obtained from ANSYS FLUENT and MOL solution of DOM. As can be seen from the table, radiative properties obtained from ANSYS FLUENT are found to be in good agreement with those of MOL solution of DOM with average absolute error of  $5.95 \times 10^{-3}$  % for absorption coefficients and average absolute error of  $2.05 \times 10^{-6}$  % for their associated weights.

Comparisons between incident heat fluxes predicted by the present study and those of MOL solution of DOM with SLW along the centerline ( $x = 2\text{m}$ ,  $y = 1\text{m}$ ,  $z$ ) and ( $x$ ,  $y = 1\text{m}$ ,  $z = 4\text{m}$ ) are shown in Figure 4.12. As can be seen from the figure, predictions of ANSYS FLUENT with SLW are found to be in good agreement with those of MOL solution of DOM with SLW. Incident heat fluxes obtained by MOL solution of DOM with SLW are taken as reference solution due to the absence of predictions of RT with

SNB. The maximum absolute errors are found to be 10.98% and 10.49% and average absolute errors are 2.39% and 4.59% for z-direction and x-direction, respectively.

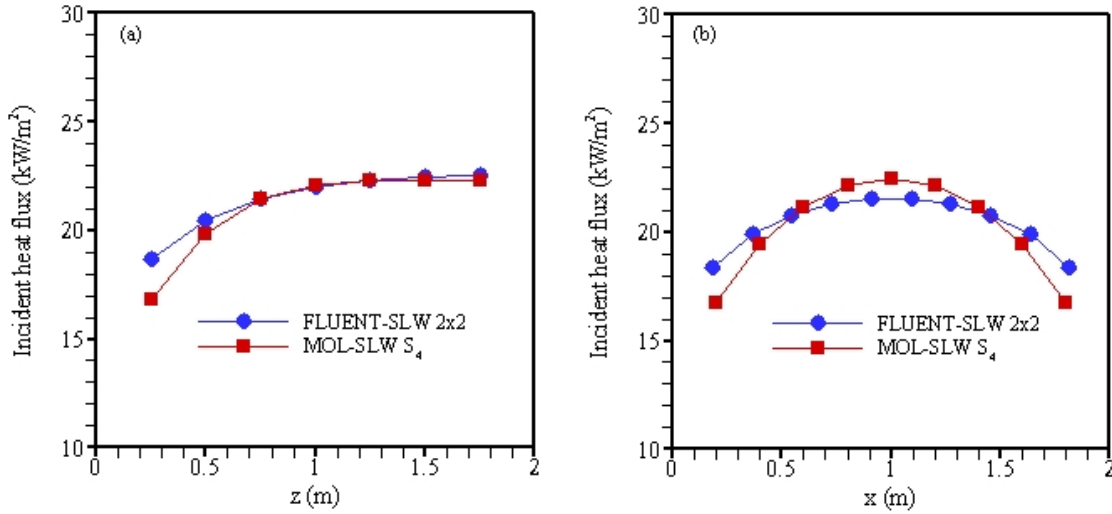


Figure 4.12. Comparison between incident heat flux predictions of present study and MOL solution of DOM with SLW for test case 3: (a) along ( $x = 2\text{m}$ ,  $y = 1\text{m}$ ,  $z$ ) and (b) along ( $x$ ,  $y = 1\text{m}$ ,  $z = 4\text{m}$ )

Overall comparisons reveal that results of ANSYS FLUENT with SLW are in good agreement with the benchmark solutions. This finding proves that the use of DOM with SLW in CFD codes would provide more accurate solutions in studies involving gas combustion where accuracy in spectral radiative properties plays dominant role in heat flux predictions.

Table 4.13. Absorption coefficients ( $\kappa_j$ ) and their associated weights ( $a_j$ ) obtained from FLUENT and MOL solution of DOM for test case 3

Grey Gases		FLUENT-SLW		MOL-SLW	
H <sub>2</sub> O	CO <sub>2</sub>	$\kappa_{j,k}$	$a_{j,k}$	$\kappa_{j,k}$	$a_{j,k}$
1	1	0.000693	0.036393	0.000693	0.036393
1	2	0.011382	0.032297	0.011383	0.032297
1	3	0.489436	0.021215	0.489467	0.021215
1	4	21.868630	0.007503	21.870030	0.007503
1	5	0.000448	0.060053	0.000448	0.060053
2	1	0.017107	0.086977	0.017108	0.086977
2	2	0.027797	0.077188	0.027799	0.077188
2	3	0.505850	0.050702	0.505880	0.050702
2	4	21.885040	0.017931	21.886450	0.017931
2	5	0.016863	0.143522	0.016864	0.143522
3	1	0.634383	0.082883	0.634420	0.082883
3	2	0.645072	0.073555	0.645110	0.073555
3	3	1.123125	0.048315	1.123190	0.048315
3	4	22.502320	0.017087	22.503760	0.017087
3	5	0.634138	0.136766	0.634170	0.136766
4	1	23.847660	0.010374	23.849190	0.010374
4	2	23.858350	0.009206	23.859880	0.009206
4	3	24.336400	0.006047	24.337970	0.006047
4	4	45.715590	0.002139	45.718540	0.002139
4	5	23.847420	0.017118	23.848950	0.017118
5	1	0.000244	0.014498	0.000245	0.014498
5	2	0.010934	0.012867	0.010935	0.012867
5	3	0.488987	0.008452	0.489010	0.008452
5	4	21.868180	0.002989	21.869580	0.002989
5	5	0.000000	0.023924	0.000000	0.023924

#### 4.4 Validation of the Radiation Code

The accuracy of the radiation code developed in this study with DOM – SNBCK for gas and Mie Theory for particles was investigated by applying the method to homogenous H<sub>2</sub>O-N<sub>2</sub>-Al<sub>2</sub>O<sub>3</sub> mixture under both isothermal and non-isothermal conditions and

validating against reference solution of Liu et al. [25] by using the same quadrature scheme,  $T_4$ , and SNB parameters provided by Soufiani and Taine [63]. All test cases used for benchmarking refer to those of Liu et al. [25].

#### **4.4.1 Absorbing-Emitting Gaseous Medium**

The test problem is a rectangular plume of 2x2x8m. The wavelength range is taken as 2000-4000  $\text{cm}^{-1}$  to predict infrared signature of the plume. Hot gas mixture in the plume is assumed to contain  $\text{H}_2\text{O}$  of 20 % and  $\text{N}_2$  of 80 %.

##### ***Test Case 1: Isothermal Absorbing-Emitting Medium***

Physical system under consideration for this problem is a 3-D plume containing uniform absorbing-emitting medium at uniform temperature of 1800 K by setting particle scattering coefficient to zero. The boundaries of the plume are assumed to be black and cold. Uniform grid structure of 11x11x40 was utilized.

Figure 4.13 shows narrowband integrated radiation intensity at  $x = 1$  m,  $y = 1$  m and  $z = 7.9$  m and along the direction of 0.0990147, 0.0990147 and 0.990147. The solution of developed DOM with SNBCK code is compared with those of DOM with SNBCK provided by Liu et al. [25]. As can be seen from the figure, narrowband integrated intensity obtained from the developed DOM with SNBCK code is found to be in excellent agreement with the benchmark solution with an average absolute error of 2.38 % in narrowband integrated radiation intensity.

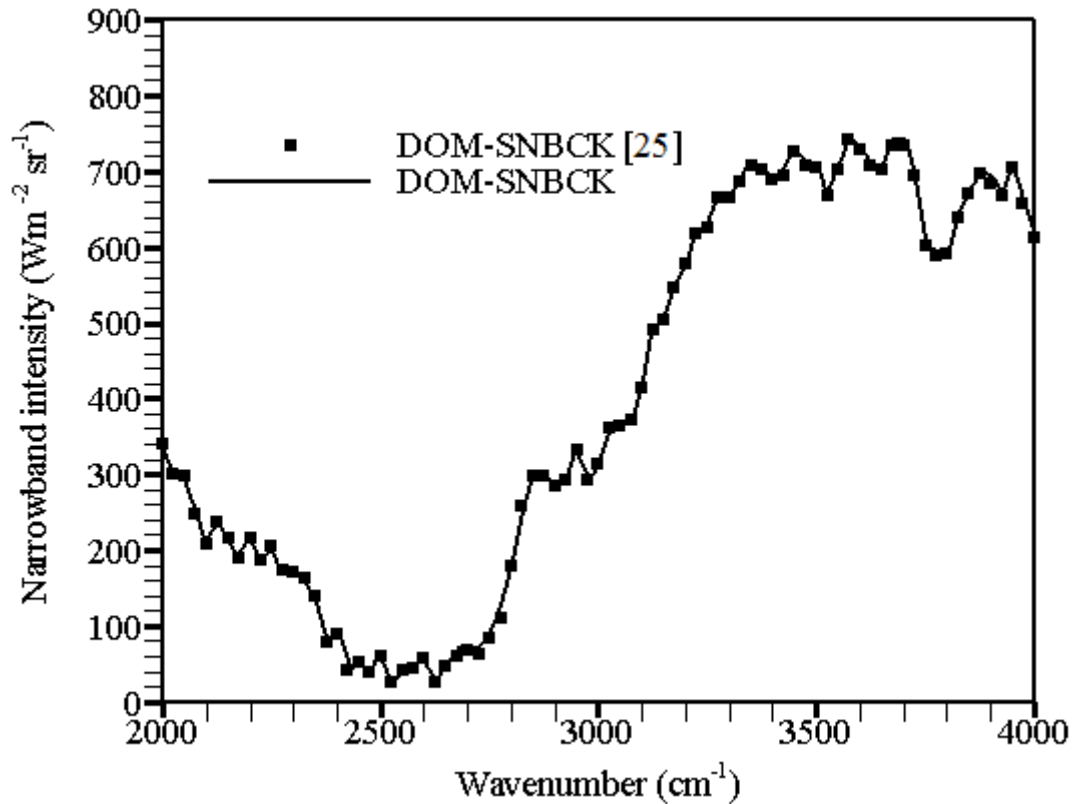


Figure 4.13. Narrowband integrated radiation intensity at  $x = 1$  m,  $y = 1$  m and  $z = 7.9$  m and along the direction of 0.0990147, 0.0990147 and 0.990147 for the isothermal absorbing-emitting case.

***Test Case 2: Non-Isothermal Absorbing-Emitting Medium***

In this case, 3-D plume containing non-isothermal absorbing-emitting medium is considered. The boundaries of the plume are assumed to be black and cold. The plume temperature is taken as symmetrical about the centerline of the plume and is specified in terms of  $T = (T_c - T_e)f(r/R) + T_e$ .  $T_c$  is the plume temperature along the centerline and  $T_e$  is the exit temperature at  $z = 8$  m. Inside the circular region of the cross section of the plume, the variation of temperature is defined by  $f(r/R) = 1 - 3(r/R)^2 + 2(r/R)^3$ , where  $r$  is the distance from the plume centerline and  $R$  is the radius of the circular region ( $R = 1$  m). The plume temperature outside the circular region is assumed

to be uniform and at the value of the exit temperature. The centerline temperature is assumed to increase linearly from 400 K at the inlet ( $z = 0$ ) to 2400 K at  $z = 0.75$  m and then decrease linearly to 800 K at the exit.

In Liu's study [25], it is stated that for non-isothermal case, a non-uniform grid was used along the length of the plume with finer grids placed around the peak temperature and uniform grid was used in the other directions by dividing into  $11 \times 11 \times 40$  control volumes. However, grid structure is not exactly defined; therefore developed DOM with SNBCK was implemented on the test problem by using uniform grid resolutions  $11 \times 11 \times 80$ , and  $11 \times 11 \times 120$ . The performance of the developed code was tested by comparing its predicted narrowband integrated radiation intensity at  $x = 1$  m,  $y = 1$  m and  $z = 7.9$  m and along the direction of 0.0990147, 0.0990147 and 0.990147 with those of DOM with SNBCK provided by Liu et al. [25] shown in Figure 4.14. As can be seen from the figure, narrowband integrated intensity calculated by the developed DOM with SNBCK code is found to be in excellent agreement with the benchmark solution. Average absolute errors in narrowband integrated radiation intensity are found to be 6.25 % and 3.66 % for  $11 \times 11 \times 80$  and  $11 \times 11 \times 120$ , respectively.

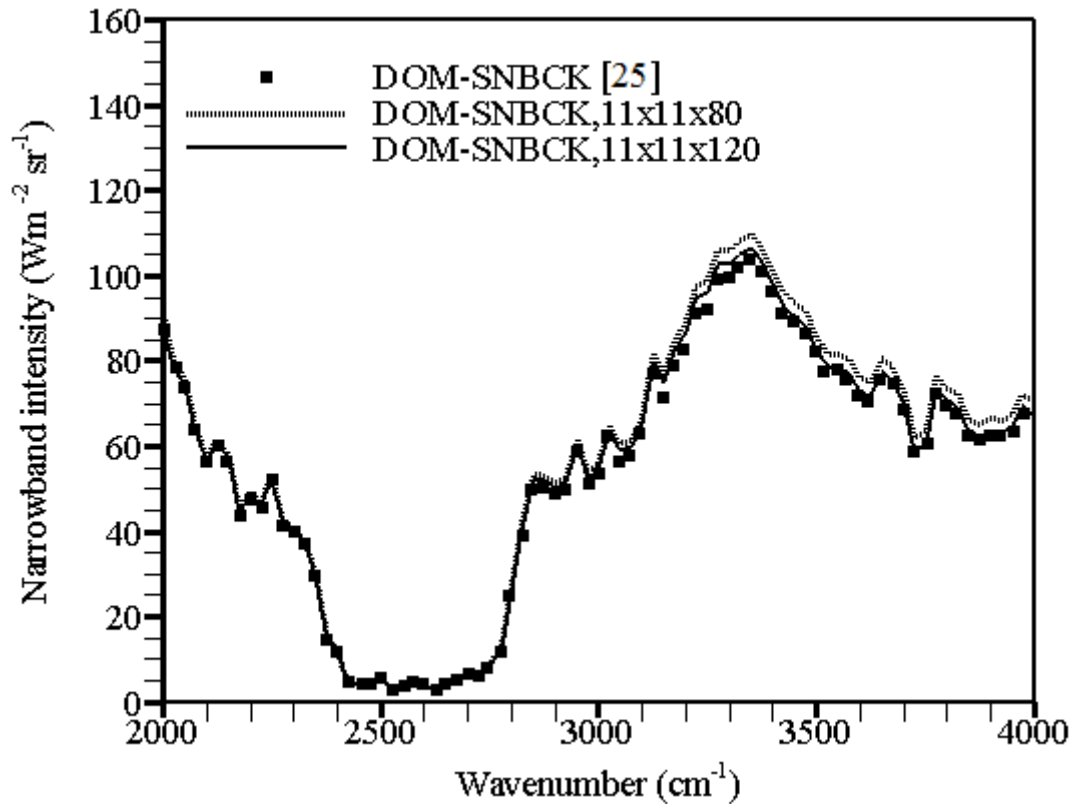


Figure 4.14. Narrowband integrated radiation intensity at  $x = 1$  m,  $y = 1$  m and  $z = 7.9$  m and along the direction of 0.0990147, 0.0990147 and 0.990147 for the non-isothermal absorbing-emitting case.

#### 4.4.2 Absorbing-Emitting Gaseous / Non-absorbing-Non-emitting-Scattering Particle Medium

The test problem is taken as a rectangular plume of  $2 \times 2 \times 8$  m. The wavelength range is taken as  $2000$ - $4000$   $\text{cm}^{-1}$  to predict infrared signature of the plume. Gas mixture in the plume is assumed to contain 20 %  $\text{H}_2\text{O}$  and 80 %  $\text{N}_2$ . Alumina particle distribution in the plume is taken as uniform with particle diameter of  $11.6$   $\mu\text{m}$ . These particles are assumed to be non-absorbing and have a refractive index of  $m=1.74$ . Radiative properties of particle are evaluated by using BHMIE code [66] and the scattering phase

function is approximated by the Henyey-Greenstein function [44] with the asymmetry factor obtained from Mie theory (see section 3.4).

***Test Case 3: Isothermal Absorbing-Emitting Gaseous / Non-absorbing-Non-emitting-Scattering Particle Medium***

The third case is a 3-D plume containing uniform absorbing-emitting-scattering medium at uniform temperature of 1800 K. The boundaries of the plume are assumed to be black and cold. The number density of particles in the plume is taken as  $2 \times 10^9 \text{ m}^{-3}$ . Uniform  $11 \times 11 \times 40$  control volumes are utilized for grid structure.

Performance of developed DOM with SNBCK code for this problem was assessed by comparing its predictions for narrowband integrated radiation intensity at  $x = 1 \text{ m}$ ,  $y = 1 \text{ m}$  and  $z = 7.9 \text{ m}$  and along the direction of 0.0990147, 0.0990147 and 0.990147 with those of DOM with SNBCK provided by Liu et al. [25]. Comparison is shown in Figure 4.15. As can be seen from the figure, narrowband integrated intensity calculated by the developed DOM with SNBCK code is found to be in excellent agreement with the benchmark solution with an average absolute error of 2.68 % in narrowband integrated radiation intensity.



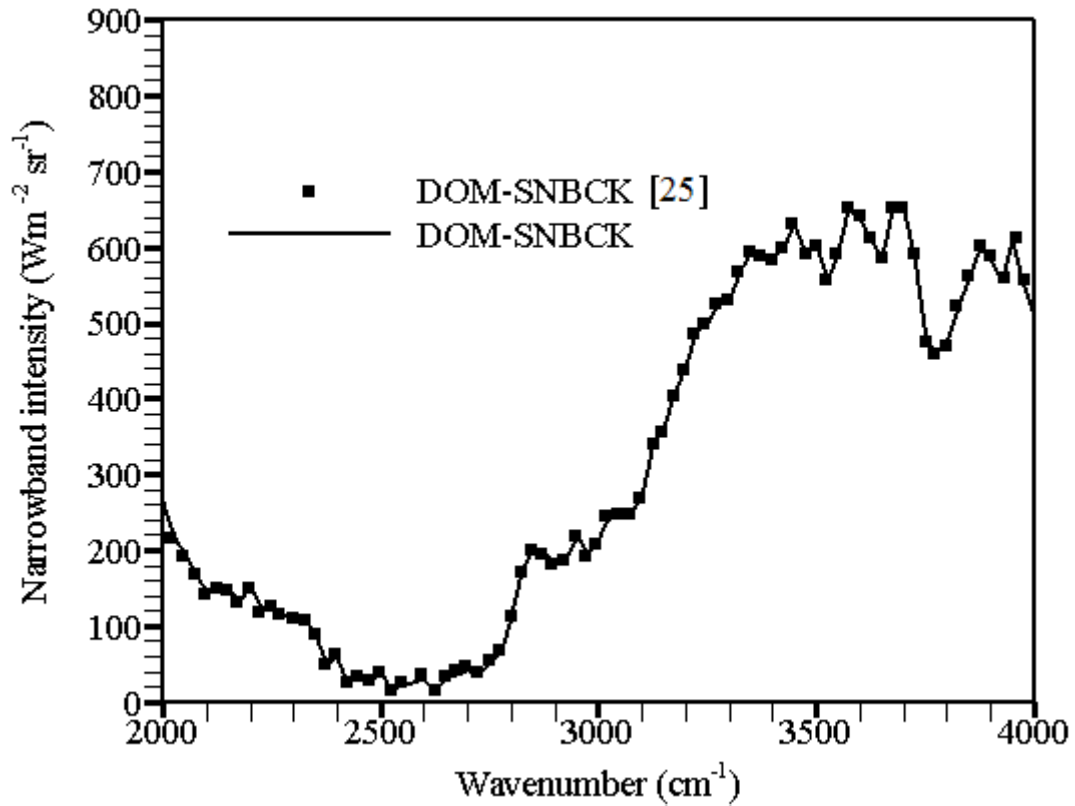


Figure 4.15. Narrowband integrated radiation intensity at  $x = 1$  m,  $y = 1$  m and  $z = 7.9$  m and along the direction of 0.0990147, 0.0990147 and 0.990147 for the isothermal absorbing-emitting-scattering case.

***Test Case 4: Non-Isothermal Absorbing-Emitting Gaseous / Non-absorbing-Non-emitting-Scattering Particle Medium***

In this case, 3-D plume containing non-isothermal absorbing-emitting medium is considered. The boundaries of the plume are assumed to be black and cold. The plume temperature is taken as symmetrical about the centerline of the plume and is specified in terms of  $T = (T_c - T_e)f(r/R) + T_e$ .  $T_c$  is the plume temperature along the centerline and  $T_e$  is the exit temperature at  $z = 8$  m. Inside the circular region of the cross section of the plume, the variation of temperature is defined by  $f(r/R) = 1 - 3(r/R)^2 +$

$2(r/R)^3$ , where  $r$  is the distance from the plume centerline and  $R$  is the radius of the circular region ( $R = 1$  m). The plume temperature outside the circular region is assumed to be uniform and at the value of the exit temperature. The centerline temperature is assumed to increase linearly from 400 K at the inlet ( $z = 0$ ) to 2400 K at  $z = 0.75$  m and then decrease linearly to 800 K at the exit. Uniform alumina particle distribution in the plume is considered to have a number density of  $2 \times 10^9 \text{ m}^{-3}$

In Liu's study [25], it is stated that for non-isothermal case, a non-uniform grid was used along the length of the plume with finer grids placed around the peak temperature and uniform grid was used in the other directions by dividing into  $11 \times 11 \times 40$  control volumes. However, grid structure is not exactly defined; therefore developed DOM with SNBCK was implemented on the test problem by using uniform grid resolutions  $11 \times 11 \times 80$ , and  $11 \times 11 \times 120$ . Figure 4.16 displays narrowband integrated radiation intensity at  $x = 1$  m,  $y = 1$  m and  $z = 7.9$  m and along the direction of 0.0990147, 0.0990147 and 0.990147. As can be seen from the figure, narrowband integrated intensity calculated by the developed DOM with SNBCK code is found to be in excellent agreement with the benchmark solution. Average absolute errors in narrowband integrated radiation intensity are found to be 7.24 % for  $11 \times 11 \times 80$  and 4.03 % for  $11 \times 11 \times 120$ .

Overall comparisons reveal that results of developed DOM with SNBCK are in good agreement with benchmark solutions for all test problems.

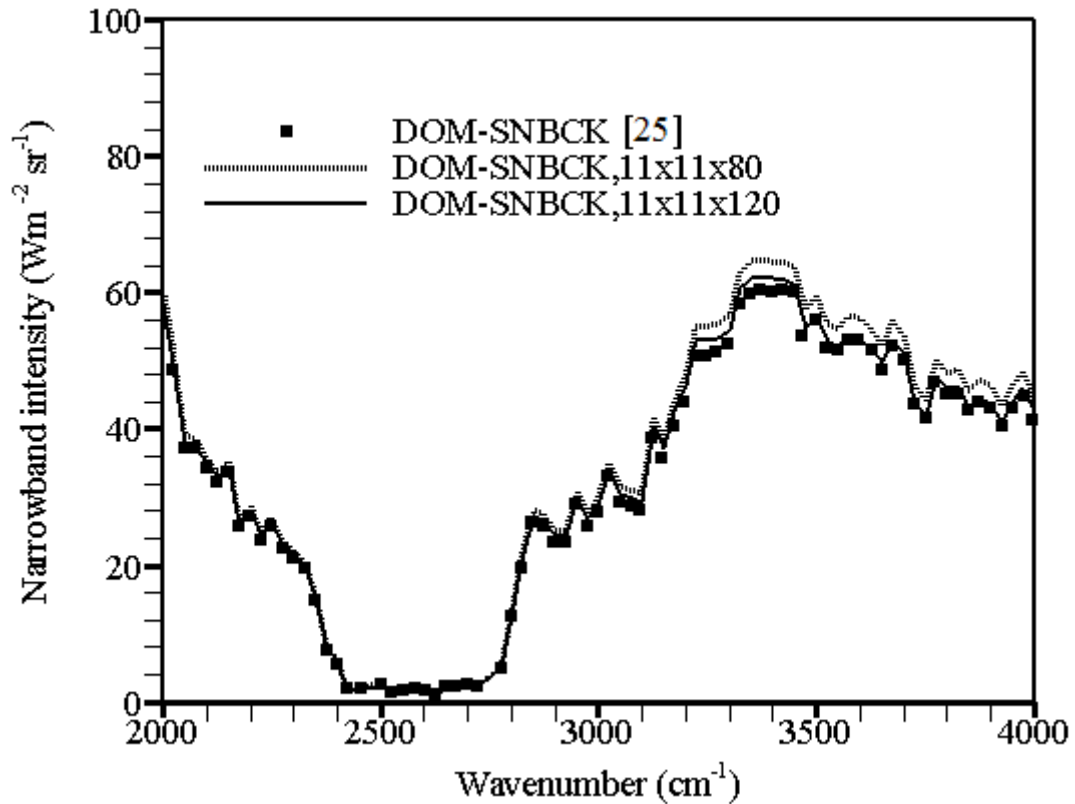


Figure 4.16. Narrowband integrated radiation intensity at  $x = 1$  m,  $y = 1$  m and  $z = 7.9$  m and along the direction of 0.0990147, 0.0990147 and 0.990147 for the non-isothermal absorbing-emitting-scattering case.

#### 4.5 Exhaust Plume Simulation for Non-Aluminized Propellant Case

Evaluation of the accuracy of the radiation code developed within this study necessitates experimental data on a test facility. As no test facility with measurements was available for aluminized solid rocket motor in the open literature, a non-aluminized solid propellant rocket motor is selected for this purpose. The motor consists of metal case, propellant and nozzle. The throat and the exit diameters of nozzle are 15 mm and 25 mm, respectively. The expansion cone of the nozzle is taken as  $15^\circ$ . The propellant consists of 87% AP and 13% HTPB. Motor performance and the thermodynamic

parameters at the nozzle throat and exit were computed by a CFD code and the NASA thermochemical code CET89 [87]. The values of pressure, temperature and chemical compositions provided for this test are given Table 4.14.

Table 4.14. Pressure, temperature and chemical compositions for non-aluminized propellant case [27]

	<b>Stagnation</b>	<b>Throat</b>	<b>Exit</b>
<b>Pressure (Pa)</b>	$3.43 \times 10^6$	$2.24 \times 10^6$	$2.88 \times 10^5$
<b>Temperature (K)</b>	2930	2720	1960
<b>Species (mole fraction)</b>			
<b>H<sub>2</sub>O</b>	-	0.400	0.400
<b>CO<sub>2</sub></b>	-	0.120	0.136
<b>CO</b>	-	0.130	0.115
<b>N<sub>2</sub></b>	-	0.090	0.096
<b>H<sub>2</sub></b>	-	0.070	0.056
<b>OH</b>	-	-	0.056
<b>HCl</b>	-	0.190	0.192

Measurements available on the test are infrared (IR) images of the plume taken by an IR camera and spectral distribution of IR emission measured with a spectroradiometer in the wavelength range of 1.5-5.5  $\mu\text{m}$ .

Freestream conditions used in their study are illustrated in Table 4.15. Mach number of freestream was taken as 0.2 [27] to improve the computational scheme for the compressible flow. 10 chemical reactions between the plume species and the ambient atmospheric gases were used in their study [27]. Further details of the test facility and measurements can be found in [27].

Table 4.15. Freestream Conditions

<b>Parameters</b>	
Pressure (Pa)	101325
Temperature (K)	300
Mach Number	0.2
N <sub>2</sub> (mole fraction)	0.79
O <sub>2</sub> (mole fraction)	0.21

Based on the data provided on the selected test facility, plume flow field and IR radiation predictions carried out in the present study are given in the following sections.

#### **4.5.1 Plume Flow Field**

For evaluation of plume flow field of the test motor, ANSYS FLUENT without and with radiation (grey WSGG and SLW) was applied to predict plume profiles in the present work. SLW model was implemented to ANSYS FLUENT by UDF. DOM was used as RTE solver. 2x2 order of approximation (total number of ordinates = 32) was utilized for angular quadrature scheme.

The non-uniform 240000 quadrilateral cells were utilized for grid resolution (Figure 4.17). As can be seen from the figure, finer grids were utilized in the plume zone and mixing layer. Plume axial and radial lengths were taken as 1m. ANSYS FLUENT was executed until steady state on 16 parallel processors (AMD 1333MHz with 3 GB RAM). ANSYS FLUENT solver parameters and boundary types used in the present study are summarized in Table 4.16 and Table 4.17, respectively. Details of parameters can be found in [55]. Boundary conditions for nozzle exit and freestream were taken as values given in Table 4.14 and Table 4.15, respectively.

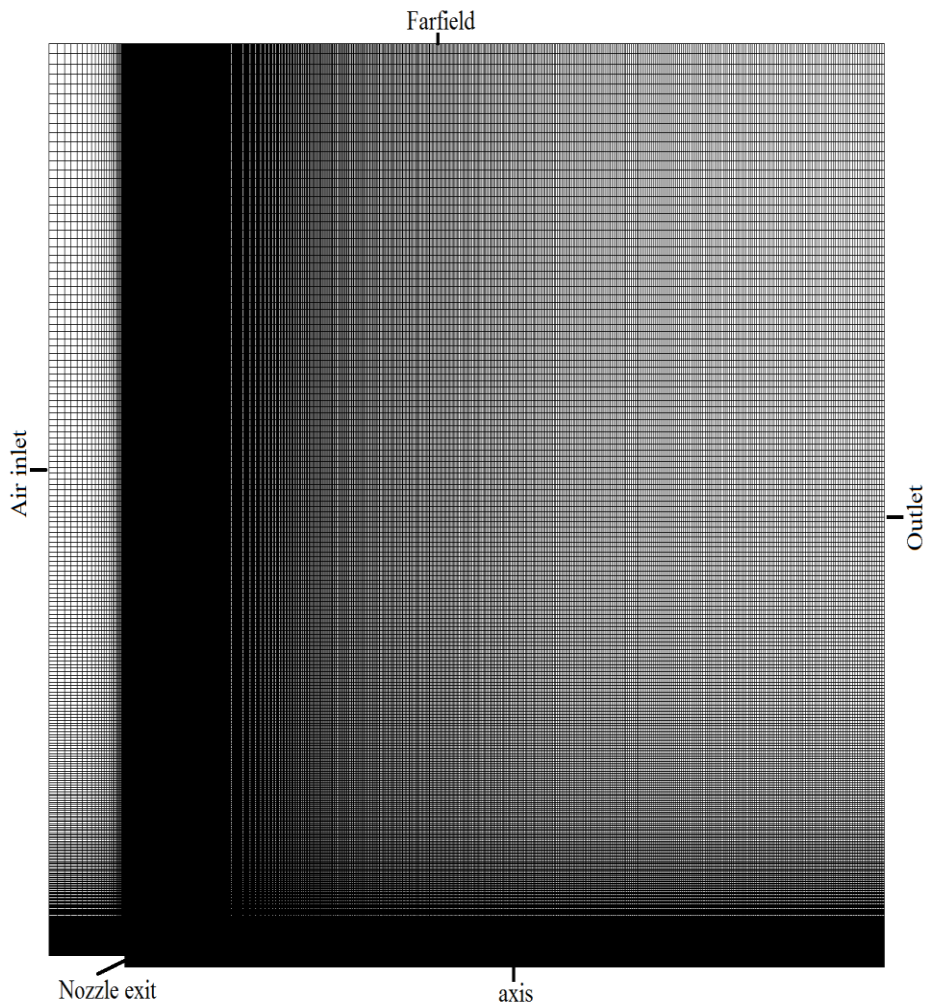


Figure 4.17. Grid resolution used in non-aluminized/aluminized propellant cases

Table 4.16. ANSYS FLUENT solver parameters used in the present study

<b>Parameters</b>	
Solver	Pressure-Based
Turbulence Model	Standard k-omega
Solution Method	Coupled
Spatial Discretization	First Order Upwind

Table 4.17. Boundary types used in the present study

at	Type
Nozzle exit	Mass-flow-inlet
Air inlet	Pressure-far-field
Outlet	Pressure-outlet
Farfield	Pressure-far-field
Axis	axis

In the present study, 10 chemical reactions given in [27] were utilized. Reaction chemistry parameters based on REP3 ( $k_f = A T^b \exp(-E_a/T)$ ) [88] was utilized by using UDF in CHEMKIN format [55]. Chemical reactions and their reaction chemistry parameters are summarized in Table 4.18.

Table 4.18. Chemical reactions with reaction chemistry parameters

No	Chemical Reactions	A	b	E <sub>a</sub> (kJ/mol)
1	$H+O_2 \rightleftharpoons OH+O$	$1.45 \times 10^{14} \text{ cm}^3/(\text{mol s})$	0	68.59
2	$OH+OH \rightleftharpoons H_2O + O$	$6.02 \times 10^{12} \text{ cm}^3/(\text{mol s})$	0	4.57
3	$OH+CO \rightleftharpoons CO_2 + H$	$1.69 \times 10^7 \text{ cm}^3/(\text{mol s K}^{1.3})$	1.3	-2.74
4	$H+ OH+X^6 \rightleftharpoons H_2O+X$	$3.63 \times 10^{22} \text{ cm}^6 \text{ K}^2/(\text{mol}^2 \text{ s})$	-2	0
5	$2O+X \rightleftharpoons O_2+X$	$1.09 \times 10^{14} \text{ cm}^6/(\text{mol}^2 \text{ s})$	0	-7.48
6	$H_2 + O \rightleftharpoons OH+H$	$1.81 \times 10^{10} \text{ cm}^3/(\text{mol s K})$	1	37.25
7	$OH+H_2 \rightleftharpoons H_2O + H$	$1.14 \times 10^9 \text{ cm}^3/(\text{mol s K}^{1.3})$	1.3	15.17
8	$2H+X \rightleftharpoons H_2+X$	$1.09 \times 10^{18} \text{ cm}^6 \text{ K}/(\text{mol}^2 \text{ s})$	-1	0
9	$H+O +X \rightleftharpoons OH+X$	$3.63 \times 10^{18} \text{ cm}^6 \text{ K}/(\text{mol}^2 \text{ s})$	-1	0
10	$CO+O+X \rightleftharpoons CO_2 + X$	$2.54 \times 10^{15} \text{ cm}^6/(\text{mol}^2 \text{ s})$	0	18.29

<sup>6</sup> X can be any one of the chemical species

Comparisons between temperature, axial velocity, Mach number, H<sub>2</sub>O mole fraction, CO<sub>2</sub> mole fraction and CO mole fraction profiles predicted by ANSYS FLUENT without radiation and with grey WSGG and SLW along the centerline from nozzle exit are illustrated in Figure 4.18. As can be seen from the figures, there are no significant discrepancies between predictions of ANSYS FLUENT without radiation and with grey WSGG and SLW.

Figure 4.19-Figure 4.23 show the comparisons between the predictions of the present study for radial temperature, axial velocity, Mach number, H<sub>2</sub>O mole fraction and CO<sub>2</sub> mole fraction profiles at 0.1 m from nozzle exit ( $z = 0.1$  m) and 0.6 m from nozzle exit ( $z = 0.6$  m). As can be seen from the figures, predictions of ANSYS FLUENT without radiation and with grey WSGG and SLW are in good agreement with each other. Temperature, H<sub>2</sub>O mole fraction CO<sub>2</sub> mole fraction and CO mole fraction fields for three runs are illustrated in Figure 4.24-Figure 4.27, respectively. As can be seen from the figures, the field behaviors are similar for all three runs. In the study of Dombrovsky [40], it is stated that thermal radiation of plume does not influence plume field such as temperature field at low altitude due to fact that dynamic and chemical reactions between plume and free stream dominate the formation of the plume field. The results of this study are in agreement with statements of Dombrovsky [40].



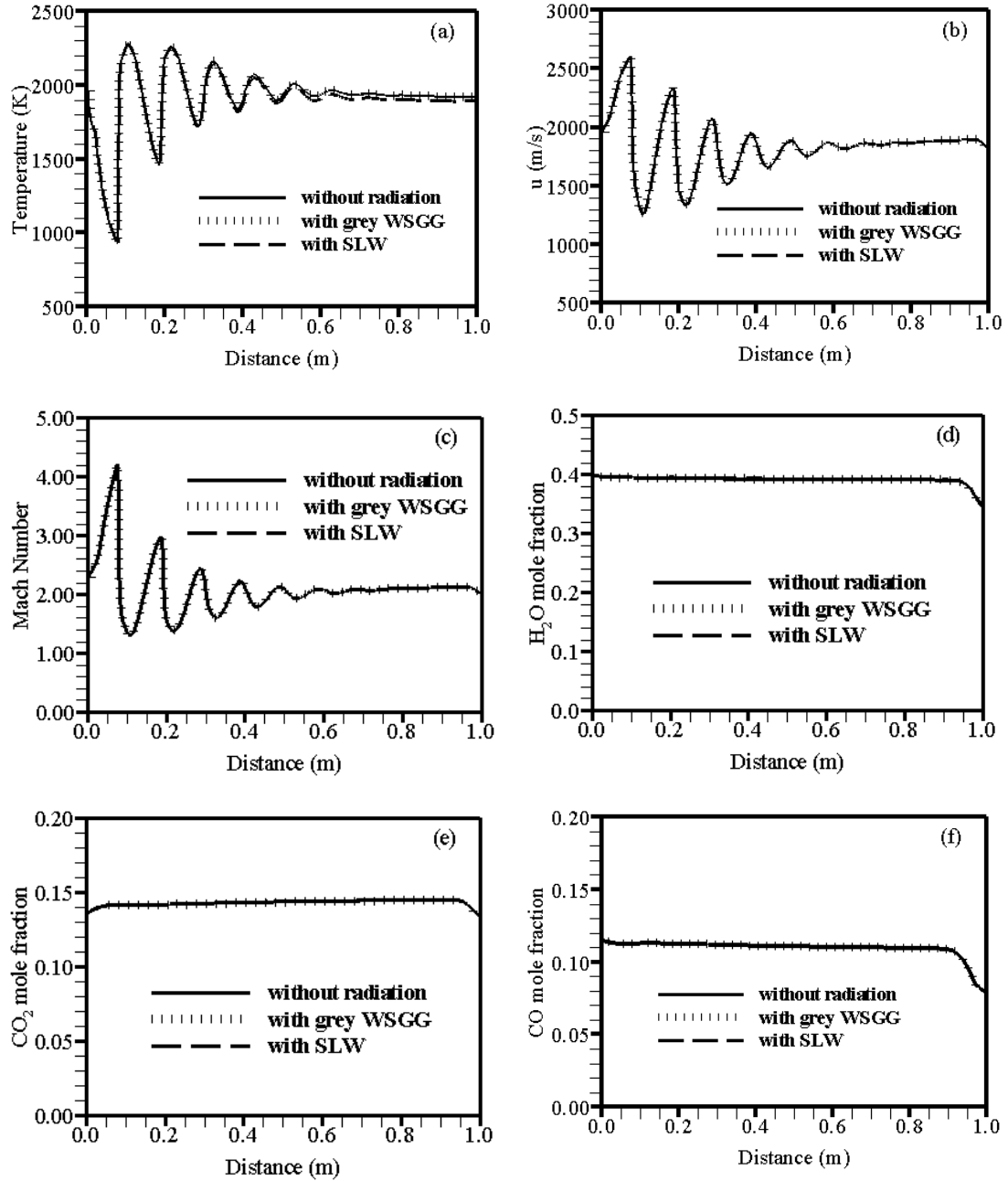


Figure 4.18. Profiles along centerline from nozzle exit for non-aluminized propellant case (a) temperature (b) axial velocity (c) Mach number (d)  $H_2O$  mole fraction (e)  $CO_2$  mole fraction (f) CO mole fraction

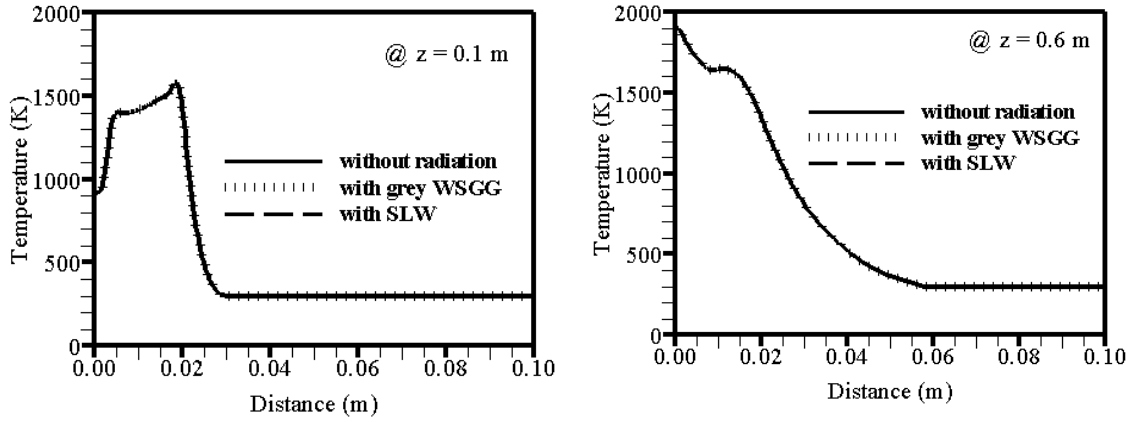


Figure 4.19. Radial temperature profile at 0.1 m from nozzle exit ( $z = 0.1$  m) and 0.6 m from nozzle exit ( $z = 0.6$  m) non-aluminized propellant case

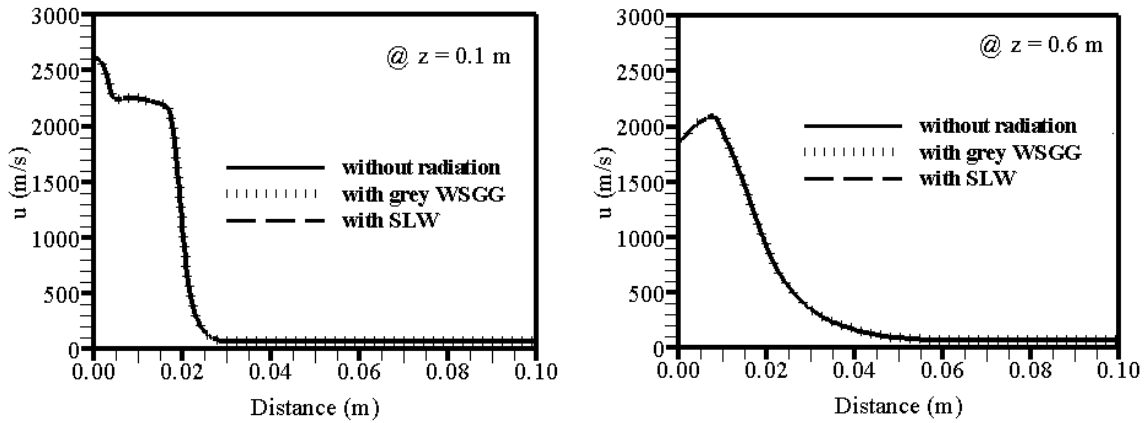


Figure 4.20. Radial axial velocity profile along centerline at 0.1 m from nozzle exit ( $z = 0.1$  m) and 0.6 m from nozzle exit ( $z = 0.6$  m) non-aluminized propellant case

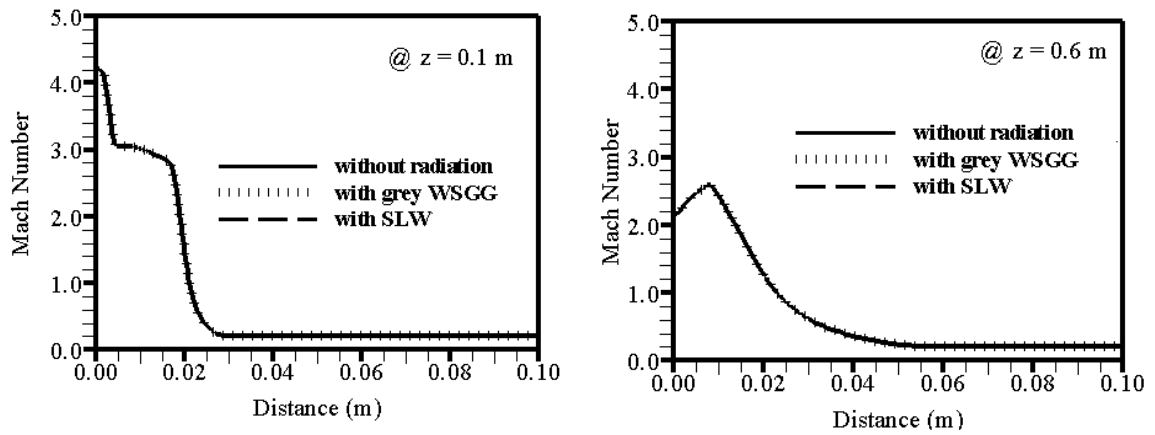


Figure 4.21. Radial Mach number profile along centerline at 0.1 m from nozzle exit ( $z = 0.1$  m) and 0.6 m from nozzle exit ( $z = 0.6$  m) non-aluminized propellant case

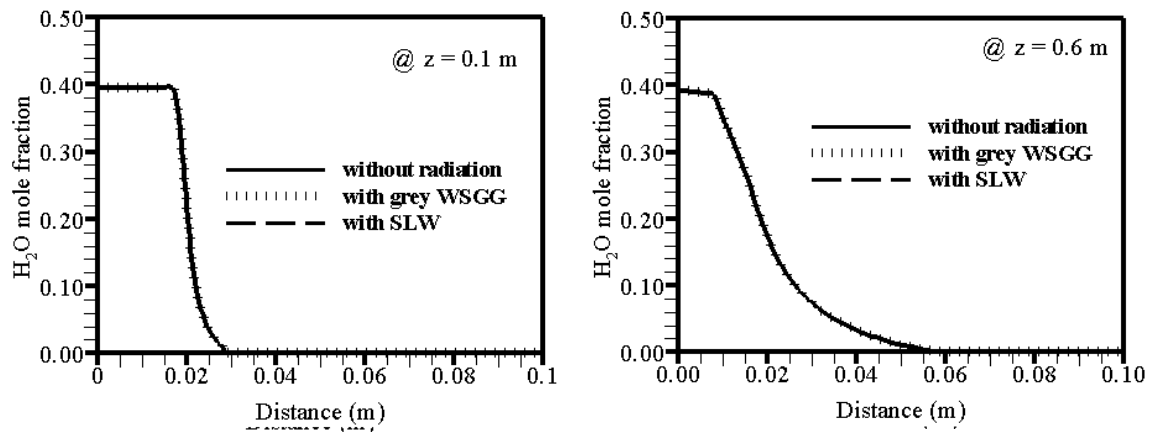


Figure 4.22. Radial H<sub>2</sub>O mole fraction profile along centerline at 0.1 m from nozzle exit ( $z = 0.1$  m) and 0.6 m from nozzle exit ( $z = 0.6$  m) non-aluminized propellant case

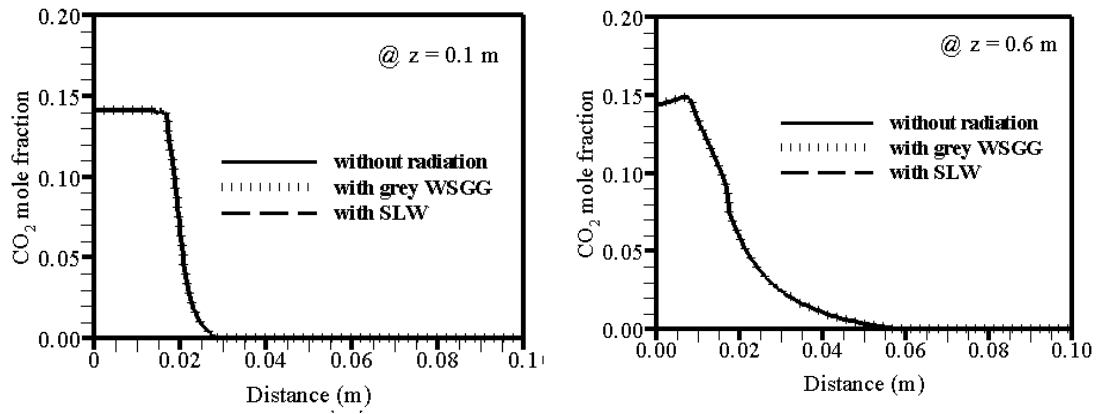


Figure 4.23. Radial CO<sub>2</sub> mole fraction profile along centerline at 0.1 m from nozzle exit ( $z = 0.1$  m) and 0.6 m from nozzle exit ( $z = 0.6$  m) non-aluminized propellant case

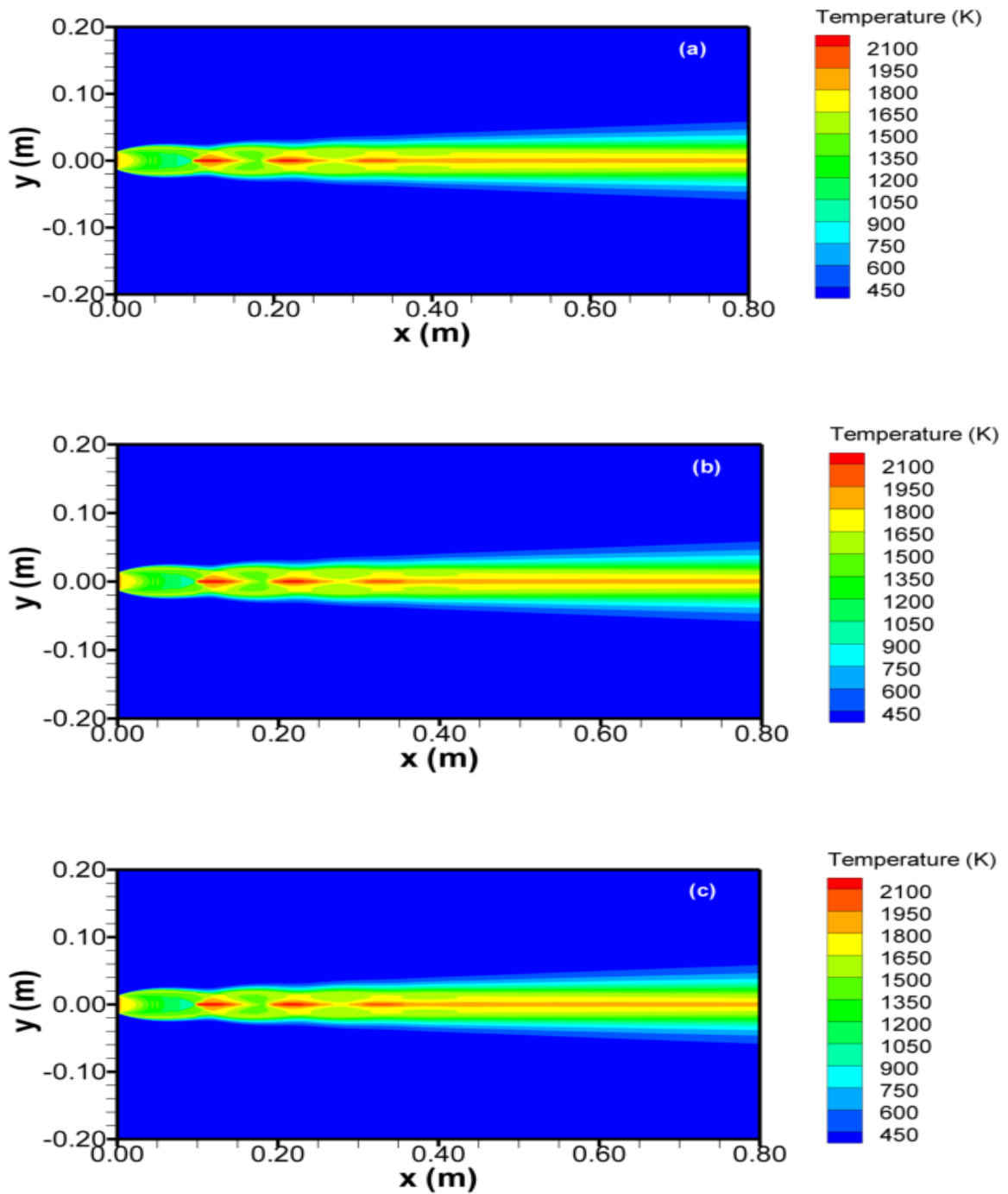


Figure 4.24. Temperature field of plume non-aluminized propellant case (a) without radiation (b) with grey WSGG (c) with SLW

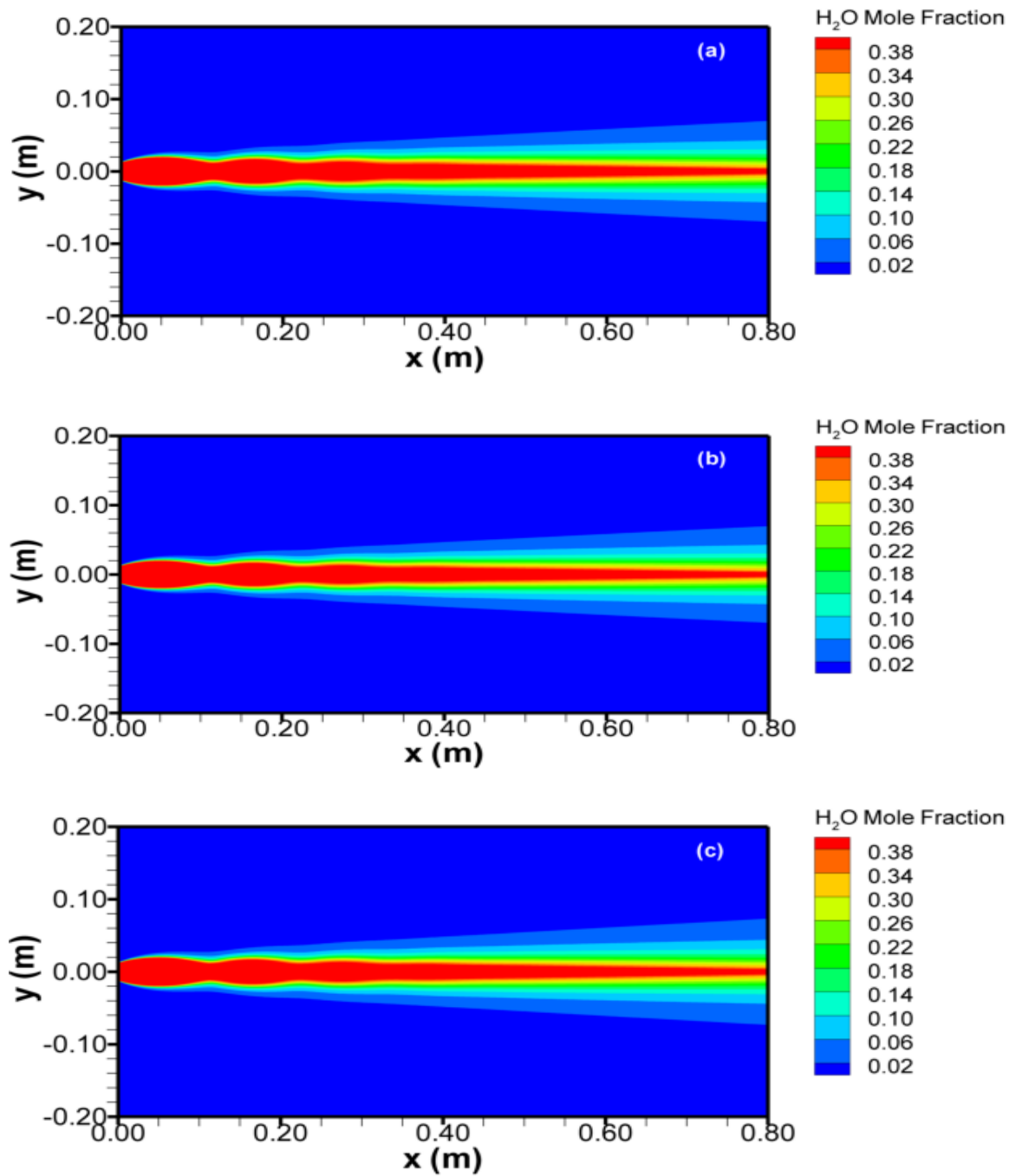


Figure 4.25. H<sub>2</sub>O mole fraction field of plume non-aluminized propellant case (a) without radiation (b) with grey WSGG (c) with SLW

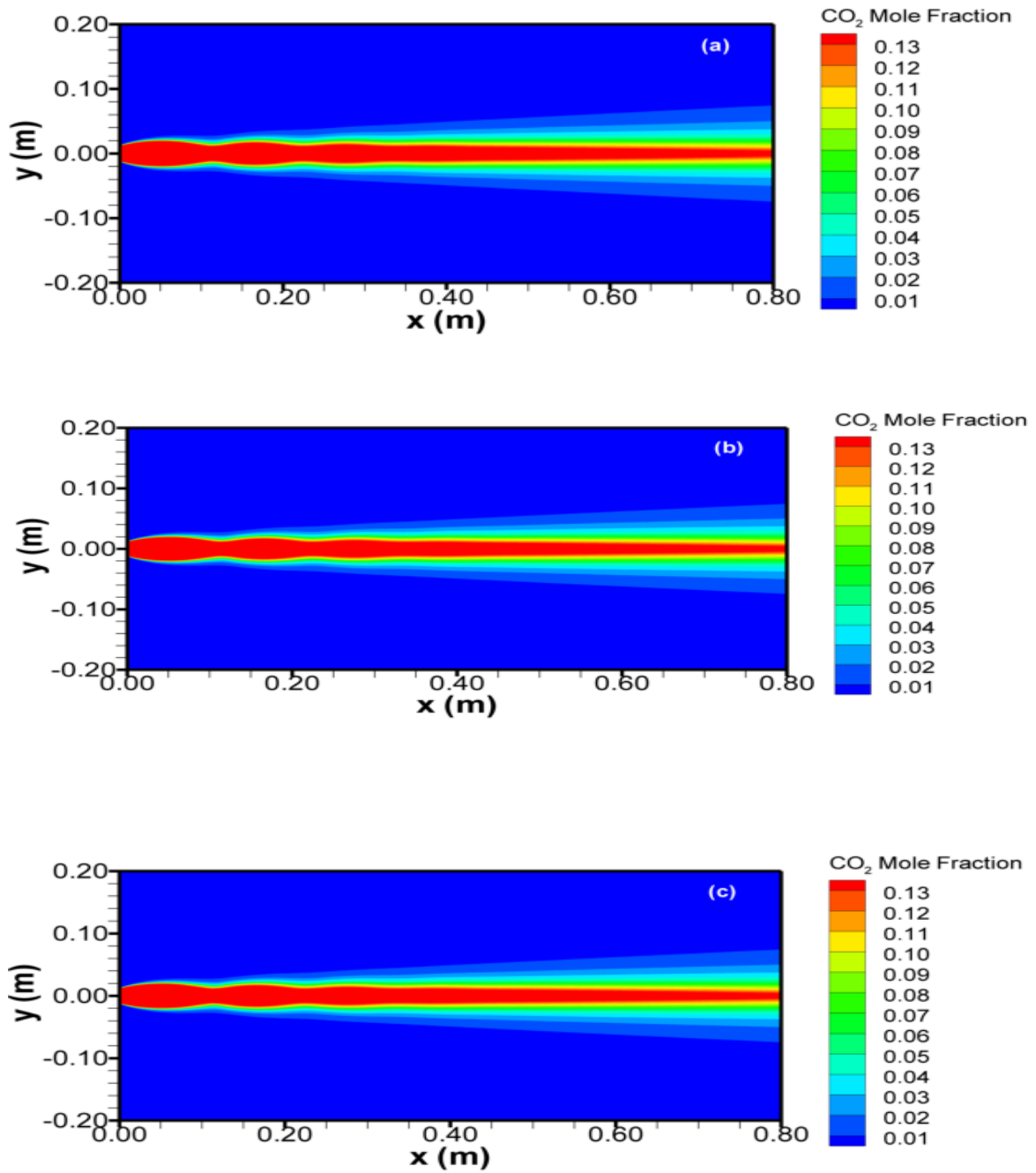


Figure 4.26. CO<sub>2</sub> mole fraction field of plume non-aluminized propellant case (a) without radiation (b) with grey WSGG (c) with SLW

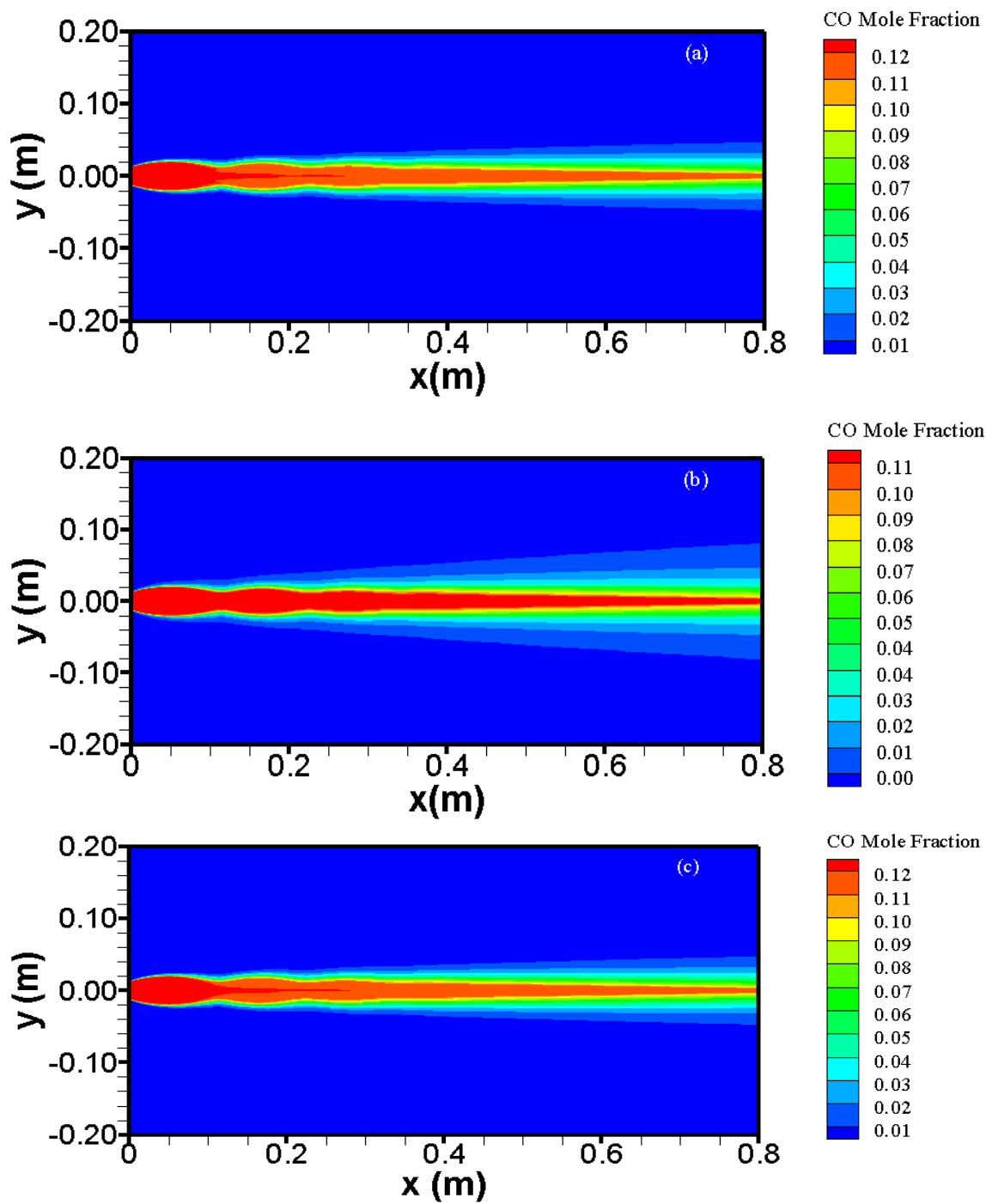


Figure 4.27. CO mole fraction field of plume non-aluminized propellant case (a) without radiation (b) with grey WSGG (c) with SLW



CPU times for all three runs are tabulated in Table 4.19. As can be seen from the table, results obtained from ANSYS FLUENT without radiation are found to require four times lower CPU time than those of ANSYS FLUENT with grey WSGG and fifteen times lower CPU time than those of ANSYS FLUENT with SLW.

Table 4.19. CPU times for all three runs

<b>Runs</b>	<b>CPU Times (h)</b>
without radiation	68
With grey WSGG	275
with SLW	984

#### 4.5.2 Plume IR Radiation

In this study, radiation code based on DOM with SNBCK and Mie Theory was used to predict plume radiation. For the implementation of the DOM, the  $S_N$  angular quadrature scheme proposed by Carlson and Lathrop [51] and  $T_4$  [54] are selected. SNB parameters provided by Riviere and Soufiani [64] were used for SNBCK calculation. Input data for the radiation code such as temperature and gas concentration was obtained by using CFD solver given in the section 4.4.1. 2D input data obtained by CFD solver was transported to 3D input data and coarser grid was utilized for radiation code compared to that of CFD due to the nature of radiation transport [89].

Simulations were carried out on a personal computer with Intel® Xeon® 3.76 GHz processor having 16.0 GB of RAM.

Sensitivity of the source spectral radiant intensity to the presence of CO was tested by comparing the predictions of DOM with SNBCK and Mie Theory considered with  $H_2O-CO_2$  and with  $H_2O-CO_2-CO$  (see in Figure 4.28).  $S_4$  angular quadrature and grid resolution 30x30x100 were utilized. As can be seen from the figure, source spectral radiant intensity is affected mostly in the wavelength interval between 4.7  $\mu m$  and 5.2  $\mu m$  by the presence of CO.

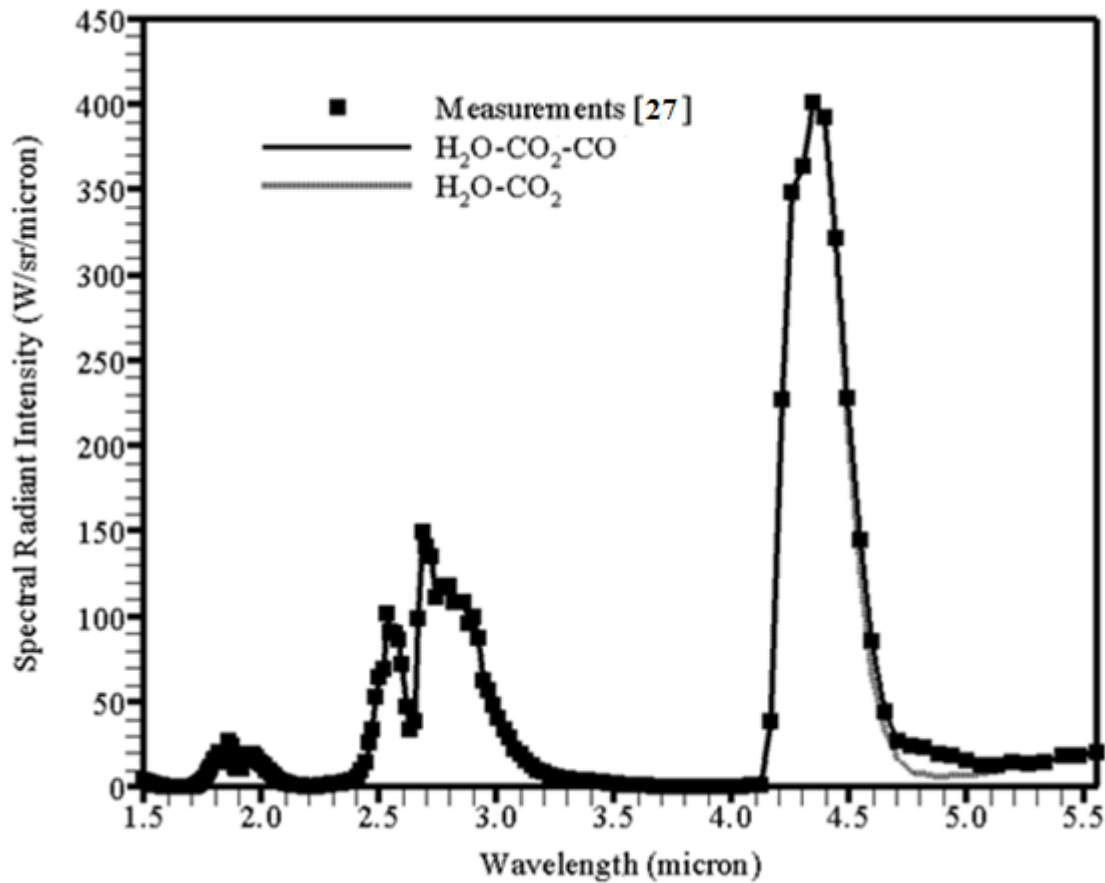


Figure 4.28. Source spectral radiant intensity for H<sub>2</sub>O-CO<sub>2</sub>-CO mixture and H<sub>2</sub>O-CO<sub>2</sub> mixture under non-aluminized propellant case

Therefore, H<sub>2</sub>O, CO<sub>2</sub> and CO gases were taken as combustion gases in the rest of this study. Numerical accuracy and computational economy of DOM with SNBCK and Mie Theory with respect to angular discretization ( $S_4, S_6, S_8, T_4$ ) and spatial discretization (30x30x100 and 30x30x150) were assessed by comparing its predictions of spectral radiant intensity integrated over 1 m of plume lengths with measurements provided by Avital and his co-workers [27]. The related comparisons are illustrated in Figure 4.29. As can be seen from the figure,  $S_4$  and  $S_6$  angular quadrature are found to be in good agreement with measurements whereas  $S_8$  and  $T_4$  angular quadrature leads to underprediction of spectral radiant intensity in the wavelength interval of 2.5 -3  $\mu\text{m}$  and 4.2 -5  $\mu\text{m}$ . Moreover, grid refinement was not found to affect the predictions. Moreover,

for all test cases, the spectral radiant intensity is found to be lower than that of measurement in the range of 3.22-3.84  $\mu\text{m}$  where HCl emits in this region as HCl was not taken as absorbing-emitting gas due to absence of SNBCK data.

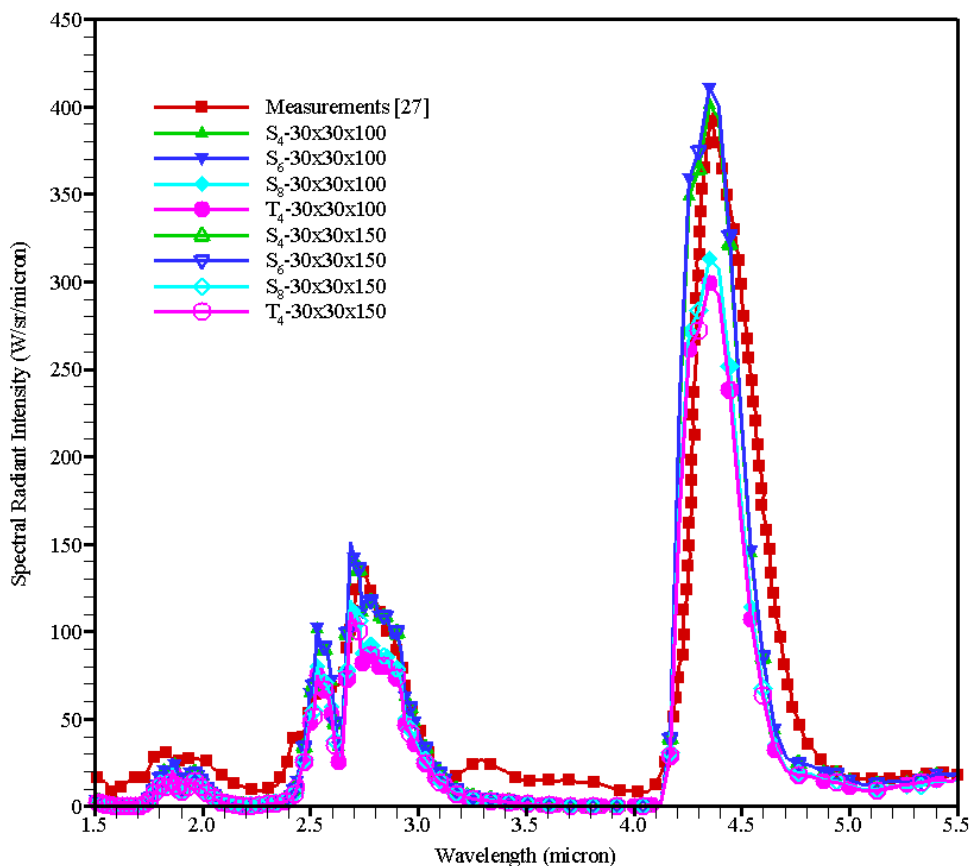


Figure 4.29. Source spectral radiant intensity for different angular quadrature and grid discretizations under non-aluminized propellant case

The absolute percentage error in radiant intensity integrated over 1.5  $\mu\text{m}$  -5.5  $\mu\text{m}$  of wavelength and corresponding CPU times is illustrated in Table 6. As can be seen from the table, the presence of CO decreases the absolute percentage errors with similar CPU time. Errors were found to be grid independent. However, CPU times were found to increase significantly with the number of grids. Hence, from the viewpoints of accuracy and computational economy, the use of H<sub>2</sub>O, CO<sub>2</sub> and CO mixture for combustion gases

and 30 x 30 x 100 control volumes with S<sub>6</sub> angular quadrature scheme were utilized in the rest of the present study.

Table 4.20. Average percentage errors in radiant intensity integrated over 1.5 μm -5.5 μm of wavelength with CPU times for non-aluminized propellant

<b>Angular Quadrature Scheme</b>	<b>Grid</b>	<b>Mixture</b>	<b>Absolute % Relative Error<sup>7</sup></b>	<b>CPU Times (s)</b>
S <sub>4</sub>	30x30x100	H <sub>2</sub> O - CO <sub>2</sub>	16.47	960
S <sub>4</sub>	30x30x100	H <sub>2</sub> O - CO <sub>2</sub> - CO	12.57	972
S <sub>6</sub>	30x30x100	H <sub>2</sub> O - CO <sub>2</sub> - CO	11.26	2377
S <sub>8</sub>	30x30x100	H <sub>2</sub> O - CO <sub>2</sub> - CO	31.33	4892
T <sub>4</sub>	30x30x100	H <sub>2</sub> O - CO <sub>2</sub> - CO	34.84	8100
S <sub>4</sub>	30x30x150	H <sub>2</sub> O - CO <sub>2</sub> - CO	12.51	1440
S <sub>6</sub>	30x30x150	H <sub>2</sub> O - CO <sub>2</sub> - CO	11.21	3240
S <sub>8</sub>	30x30x150	H <sub>2</sub> O - CO <sub>2</sub> - CO	31.29	7920
T <sub>4</sub>	30x30x150	H <sub>2</sub> O - CO <sub>2</sub> - CO	34.80	17820

<sup>7</sup>Absolute % Error = (|predicted-measurement| / measurement) × 100

To investigate atmospheric effect on the plume signature, apparent spectral intensities observed horizontally 10 m and 1000 m away from the plume were evaluated by using atmospheric transmittance obtained from MODTRAN (Figure 4.30). As can be seen from the figure, apparent spectral intensities observed 10 m away from the plume is nearly the same as those of source spectral intensities (radiation emitting from plume) whereas apparent spectral intensities observed 1000 m away from the plume significantly decrease compared to those of source spectral intensities. This is considered to be due to strong effect of atmospheric absorption.

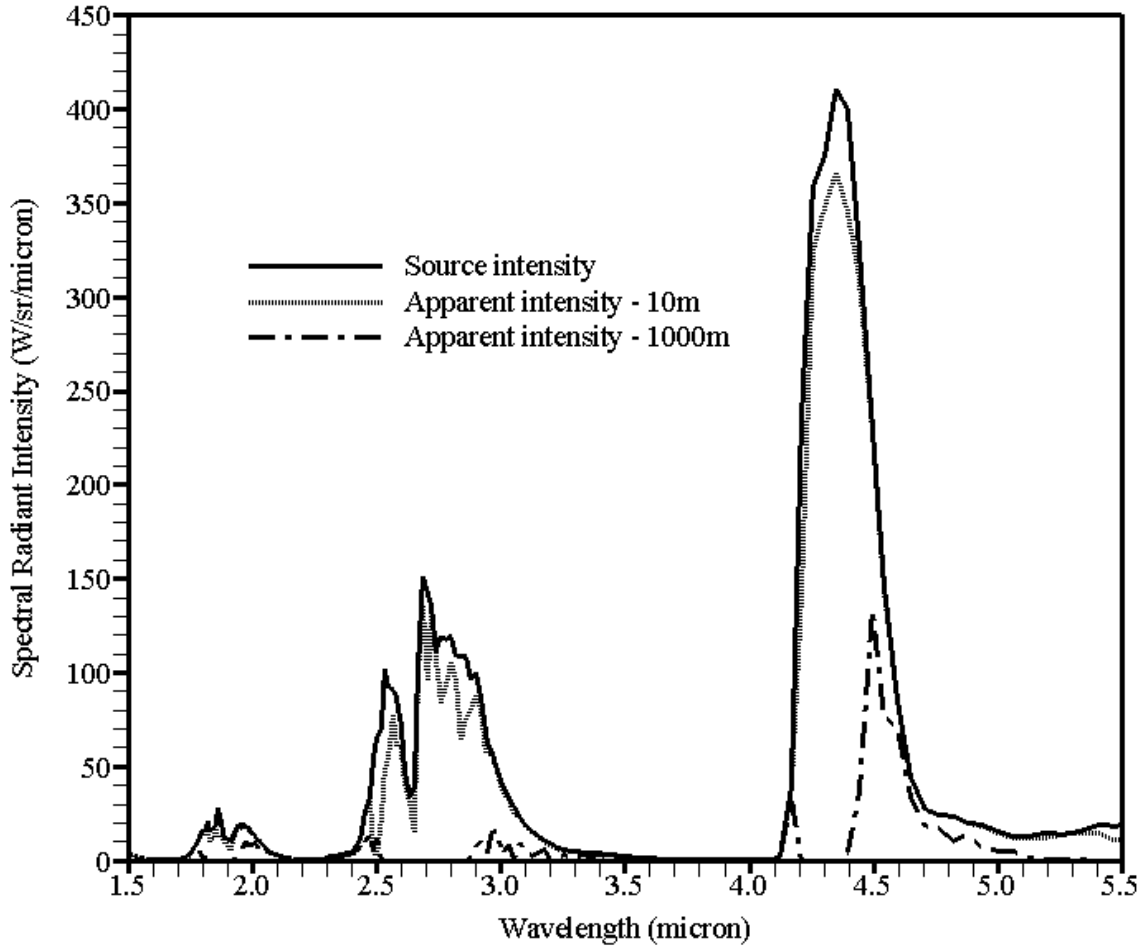


Figure 4.30. Source and apparent spectral radiant intensities for non-aluminized propellant case

#### 4.6 Exhaust Plume Simulation for Aluminized Propellant Case

For aluminized solid propellant case, motor configuration was selected the same as that of non-aluminized case. Concentration of Al in the propellant was taken as 4% due to Al content of in-house propellant. The NASA thermochemical code CET89 [87] was used to evaluate pressure, temperature and chemical compositions at throat and nozzle exit and illustrated in Table 4.21. Stagnation, throat and exit temperatures of aluminized case

are higher than those of non-aluminized case with same stagnation pressure due to  $\text{Al}_2\text{O}_3$  formation.

Table 4.21. Pressure, temperature and chemical compositions for aluminized propellant case

	<b>Stagnation</b>	<b>Throat</b>	<b>Exit</b>
<b>Pressure (Pa)</b>	$3.43 \times 10^6$	$2.24 \times 10^6$	$2.88 \times 10^5$
<b>Temperature (K)</b>	3085	2867	2070
<b>Species (mole fraction)</b>			
<b>H<sub>2</sub>O</b>	-	0.394	0.394
<b>CO<sub>2</sub></b>	-	0.116	0.134
<b>CO</b>	-	0.127	0.112
<b>N<sub>2</sub></b>	-	0.089	0.095
<b>H<sub>2</sub></b>	-	0.068	0.055
<b>OH</b>	-	-	0.055
<b>HCl</b>	-	0.187	0.191
<b>Al<sub>2</sub>O<sub>3</sub></b>	-	0.019	0.019

#### 4.6.1 Plume Flow Field

In the present study, lower CPU times as well as similar plume field profiles obtained for non-aluminized solid propellant case without radiation in the CFD solver led to the use of CFD solver without radiation in the aluminized solid propellant case. Therefore, ANSYS FLUENT without radiation was used to predict plume profiles for aluminized propellant. Grid resolution (Figure 4.17), ANSYS FLUENT solver parameters (Table 4.16) and boundary types (Table 4.17) used in aluminized case were taken the same as those of non-aluminized case. Plume axial and radial lengths were taken as 1m. ANSYS FLUENT was executed until steady state on 16 parallel processors (AMD 1333MHz with 3 GB RAM).  $\text{Al}_2\text{O}_3$  particles were assumed to be spherical and all to have the same diameter, 5 micron [90].  $\text{Al}_2\text{O}_3$  particles were taken as inert and were solved as discrete

phase in ANSYS FLUENT. Particles and gases were assumed to be in local thermodynamic equilibrium. Boundary conditions for nozzle exit and freestream used in this study are given in Table 4.21 and Table 4.15, respectively.

Comparisons between temperature, axial velocity, Mach number, H<sub>2</sub>O mole fraction and CO<sub>2</sub> mole fraction profiles and CO mole fraction profiles predicted by ANSYS FLUENT along the centerline from nozzle exit are illustrated in Figure 4.31 for non-aluminized and aluminized propellant cases. As can be seen from the figures, Al<sub>2</sub>O<sub>3</sub> particle affects the plume flow field. This is considered to be due to fact that temperature at nozzle exit for aluminized case was taken as higher than that of non-aluminized case. Moreover, particles in the plume decrease the velocity of plume.

Fields of temperature, H<sub>2</sub>O mole fraction CO<sub>2</sub> mole fraction, CO mole fraction and Al<sub>2</sub>O<sub>3</sub> concentration fields for aluminized propellant are demonstrated in Figure 4.32- Figure 4.36, respectively.

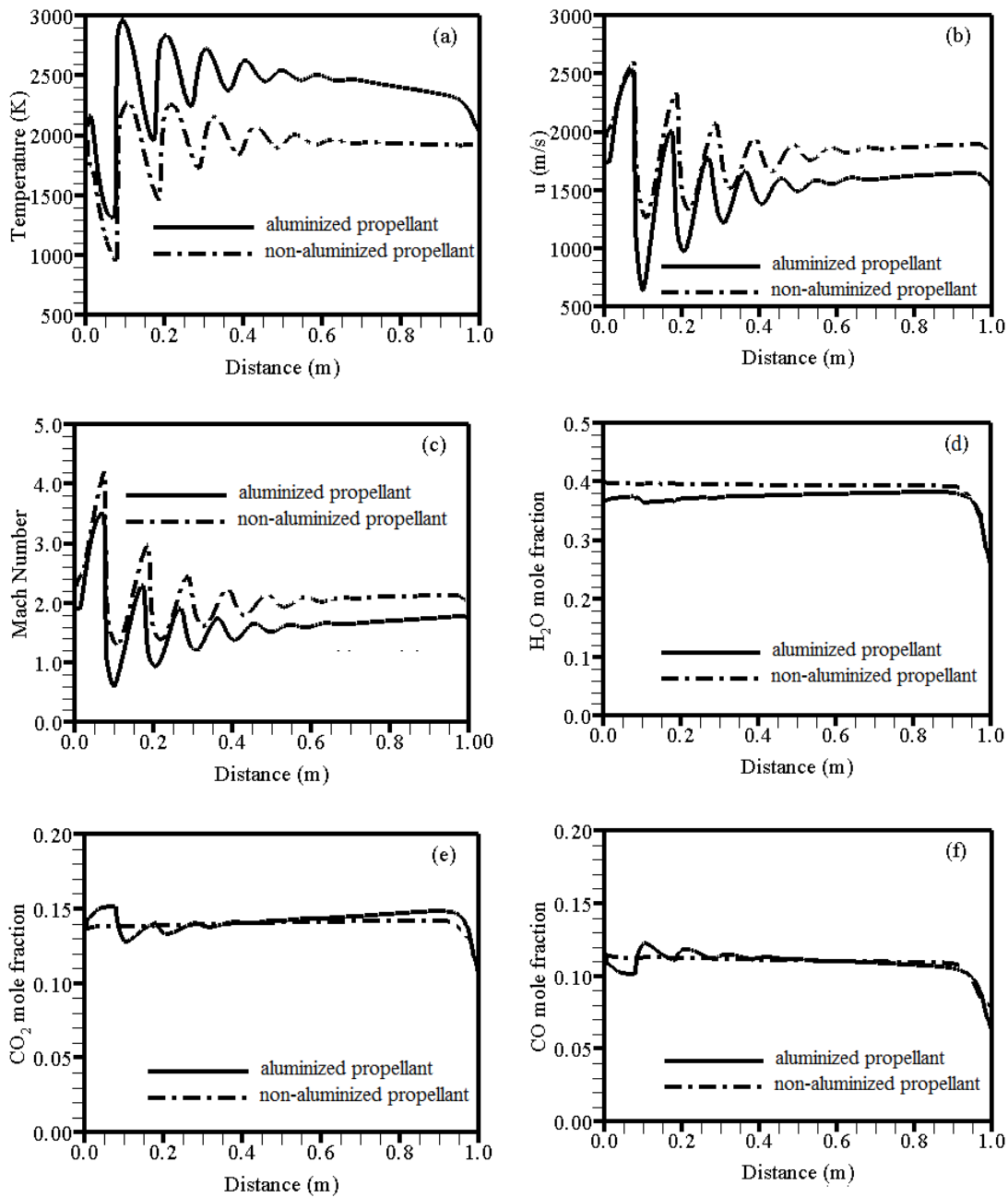


Figure 4.31. Profiles along centerline from nozzle exit for non-aluminized and aluminized propellant cases (a) temperature (b) axial velocity (c) Mach number (d)  $H_2O$  mole fraction (e)  $CO_2$  mole fraction (f)  $CO$  mole fraction



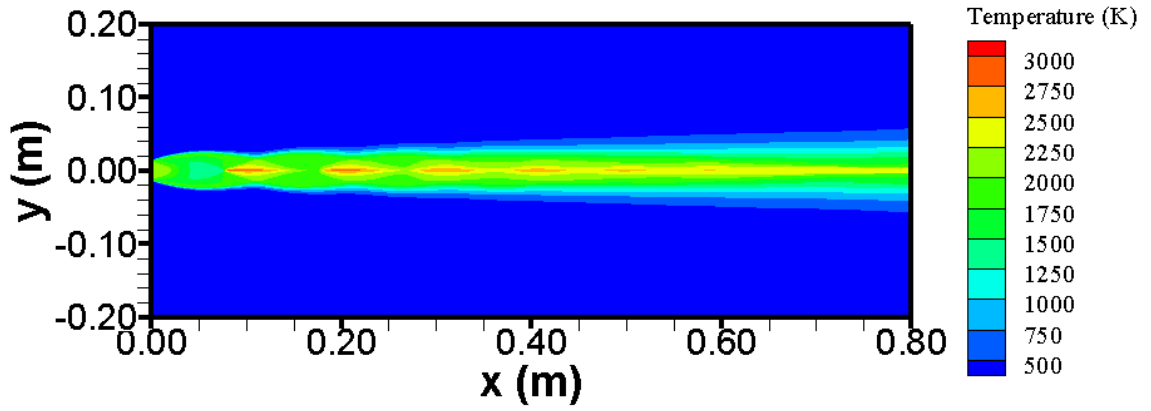


Figure 4.32. Temperature field of plume for aluminized propellant case

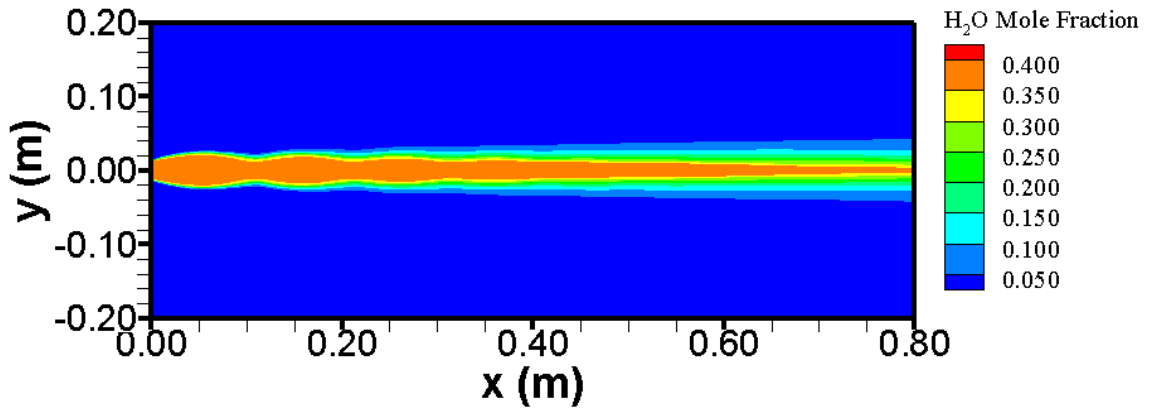


Figure 4.33. H<sub>2</sub>O mole fraction field of plume for aluminized propellant case

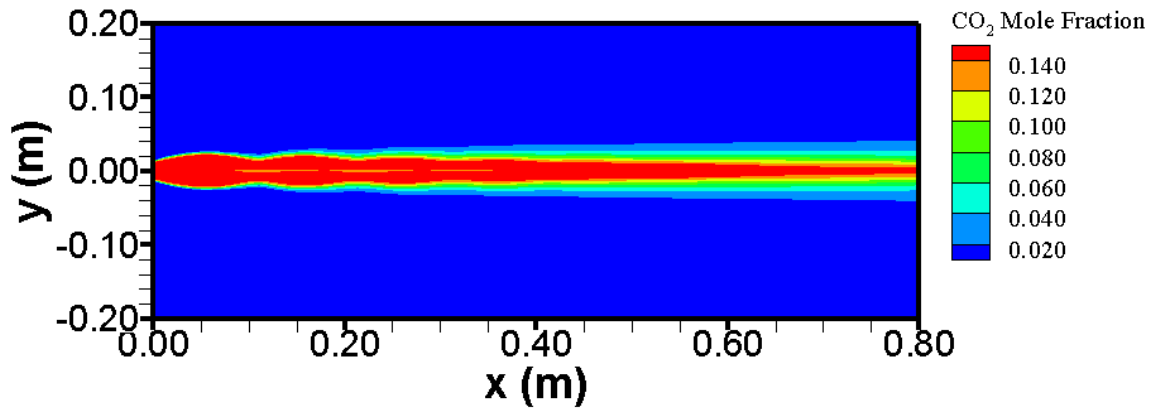


Figure 4.34. CO<sub>2</sub> mole fraction field of plume for aluminized propellant case

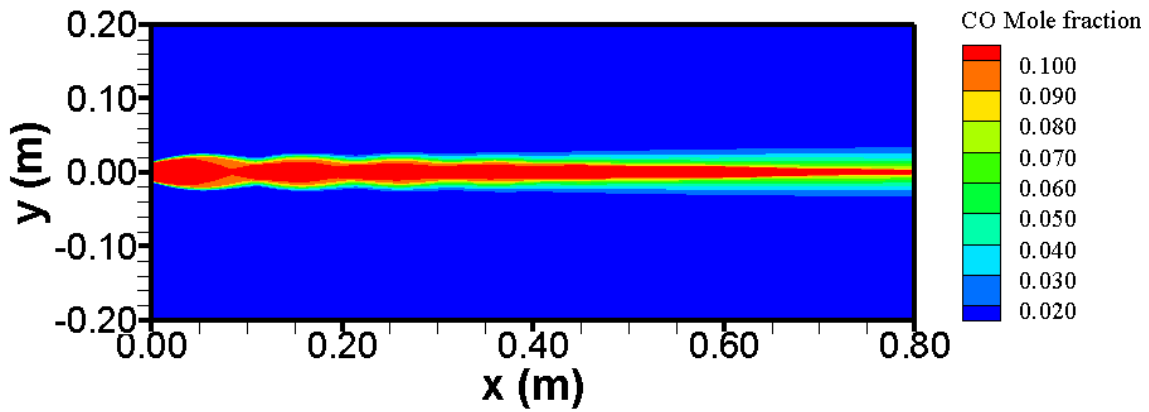


Figure 4.35. CO mole fraction field of plume for aluminized propellant case

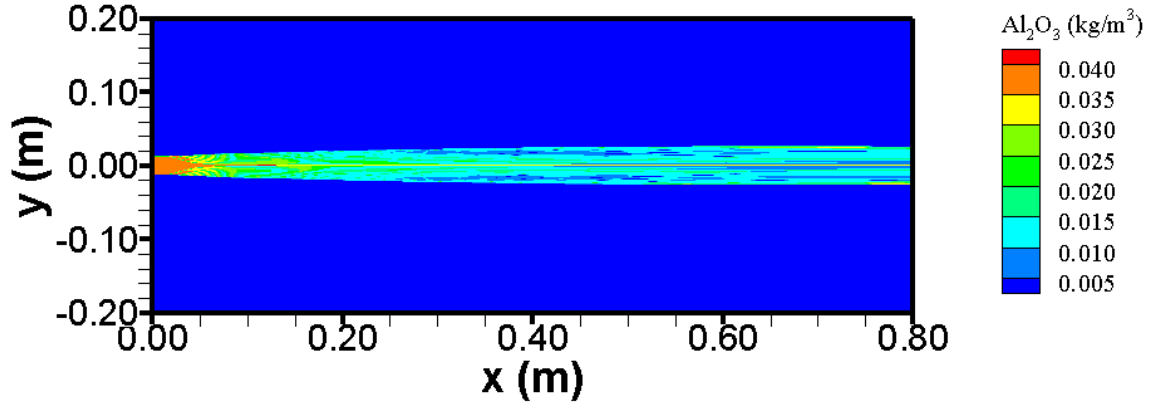


Figure 4.36.  $\text{Al}_2\text{O}_3$  concentration field of plume for aluminized propellant case

#### 4.6.2 Plume IR Radiation

For aluminized propellant case, radiation code based on DOM with SNBCK and Mie Theory was used to predict plume radiation.  $S_6$  angular quadrature scheme and  $30 \times 30 \times 100$  grid resolution were utilized. SNB parameters provided by Riviere and Soufiani [64] were used for SNBCK calculation. Radiative properties of  $\text{Al}_2\text{O}_3$  particles are obtained by using BHMIE code [66] and the scattering phase function is approximated by the Henyey-Greenstein function [44] with the asymmetry factor obtained from Mie theory (seen in section 3.2). These particles are assumed to be non-absorbing, non-emitting and scattering with a constant refractive index of  $m=1.74$  due to fact that real part of the refractive index,  $n$ , is not dependent on wavenumber and temperature; and imaginary part of refractive index is much smaller than real part of that (see in section 1.3.3). Input data for the radiation code such as temperature and gas concentration was obtained by using CFD solver given in the section 4.5.1. 2D input data obtained by CFD solver was transported to 3D input data and coarser grid was utilized for radiation code compared to that of CFD due to the nature of radiation transport [89].

Simulations were carried out on a personal computer with Intel® Xeon® 3.76 GHz processor having 16.0 GB of RAM.

Figure 4.37 shows the source spectral radiant intensity for non-aluminized and aluminized cases. As can be seen from the figure, predictions of aluminized propellant case are found to be 61% higher than those of non-aluminized propellant case. This is considered to result from the use of higher temperature profiles and radiative properties of particles under aluminized propellant case.

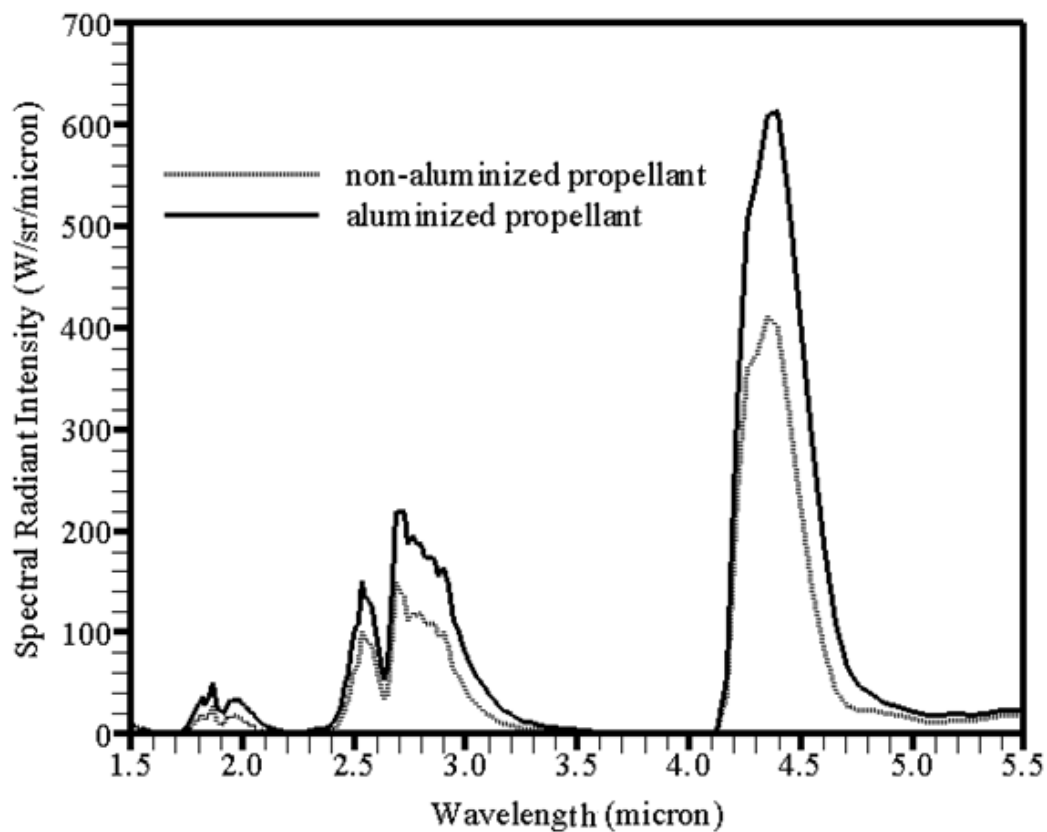


Figure 4.37. Source spectral radiant intensity for non-aluminized and aluminized propellant cases

## CHAPTER 5

### CONCLUSIONS

Plume radiation is the predominant part of plume signature which is essential for detection and tracking of rockets. For evaluation of plume radiation, plume flow field is firstly computed by solving governing equations of mass, momentum, energy, chemical species and radiant energy to provide input data for the radiation code. Then plume radiation is calculated by solving RTE in the plume containing non-homogenous non-grey absorbing-emitting scattering medium. Both CFD solver and the radiation code necessitate accurate and CPU efficient solution methods for RTE and radiative property estimation.

To select the RTE solver for CFD solver and the radiation code, the predictive accuracy and computational efficiency of popular RTE solvers, namely, DOM, P<sub>1</sub> and IDA were first investigated by applying the methods to four cubical test problems containing grey absorbing-emitting-scattering media and comparing their predictions with benchmark solutions available in the literature. It was found that DOM produces more accurate results with significantly less CPU times. Therefore, DOM was selected as RTE solver for both CFD solver and the radiation code.

To select radiative property estimation technique for CFD solver and the radiation code, a test case of 0.3 MWt ABFBC freeboard containing CO<sub>2</sub>, H<sub>2</sub>O and fly ash particles with a size distribution, was utilized. MOL of DOM was used as RTE solver in this study due to fact that the method is based on DOM and predictions of MOL solution of DOM with GG and MOL solution of DOM with SLW are already available in the literature. However, solutions of MOL solution of DOM with SNBCK for particle laden combustion gases in freeboard of fluidized bed combustors are not available to date. For

this purpose, a three-dimensional radiation code based on the MOL solution of DOM with SNBCK and geometric optics approximation was developed. Predictive accuracy and computationally efficiency of MOL solution of DOM coupled with different radiative property estimation techniques (GG, SLW and SNBCK models) were assessed by applying them to the prediction of incident radiative fluxes along the freeboard walls of a 0.3 MWt ABFBC and comparing their predictions with measurements generated previously from two runs one without and the other with recycle. Freeboard was treated as a three-dimensional rectangular enclosure containing a grey/non-grey, absorbing-emitting-isotropically scattering medium. Radiative properties of particles were evaluated by using geometric optics approximation. A comparative study was also provided between the source term distributions predicted by MOL solution of DOM with GG, SLW and SNBCK along the centerline of the freeboard for both runs. SLW was selected as radiative property estimation technique for CFD solver due to fact that it produces accurate solutions with less CPU times and SNBCK was chosen as radiative property estimation technique for the radiation code as it is highly accurate and wavelength dependent technique.

SLW was then implemented to CFD solver. The accuracy of predictions of the radiation sub-code (DOM with SLW) of ANSYS FLUENT was tested by comparing its predictions with those of MOL solution of DOM with SLW as well as those of RT with SNB available in the open literature. ANSYS FLUENT with SLW was found to provide accurate and CPU efficient solutions for input data to the radiation code.

Radiation code based on DOM with SNBCK for gas and Mie Theory for particles was developed to predict plume radiation. The accuracy of the radiation code was assessed by applying the method to homogenous  $\text{H}_2\text{O-N}_2\text{-Al}_2\text{O}_3$  mixture under both isothermal and non-isothermal conditions and validating against reference solution available in the literature. Developed radiation code was found to be in excellent agreement with this benchmark solution.

CFD solver, ANSYS FLUENT, without and with radiation (grey WSGG and SLW) was applied to predict plume field profiles for non-aluminized propellant case in order to investigate the effect of radiation on the input data provided to the radiation code. For this purpose, a non-aluminized solid propellant rocket motor with all data and measurements available in the open literature was selected. Comparisons reveal that CFD solver without radiation provides CPU efficient solution as well as similar plume field profiles.

This was followed by running the radiation code based on DOM with SNBCK for gas containing H<sub>2</sub>O-CO<sub>2</sub> and Mie Theory for particles under non-aluminized propellant case. Sensitivity of the source spectral radiant intensity to the presence of CO was first investigated by comparing the predictions of the radiation code with H<sub>2</sub>O-CO<sub>2</sub> and with H<sub>2</sub>O-CO<sub>2</sub>-CO. CO molecules were found effective on the source spectral radiant intensity in the wavelength range of 4.7 - 5.2 μm. Numerical accuracy and computational economy of the radiation code with respect to angular discretization (S<sub>4</sub>,S<sub>6</sub>,S<sub>8</sub>,T<sub>4</sub>) and spatial discretization (30x30x100 and 30x30x150) were assessed by comparing its predictions of spectral radiant intensity integrated over 1 m of plume lengths with measurements. Comparisons reveal that the use of H<sub>2</sub>O, CO<sub>2</sub> and CO mixture for combustion gases and 30 x 30 x 100 control volumes with S<sub>6</sub> angular quadrature scheme provide accurate and CPU efficient solutions. Atmospheric effect on the plume signature was also investigated. For this purpose, apparent spectral intensities observed horizontally 10 m and 1000 m away from the plume were computed by using atmospheric transmittance obtained from MODTRAN. It was found that apparent spectral intensities observed 1000 m away from the plume significantly decrease compared to those of source spectral intensities due to strong effect of atmospheric absorption.

For aluminized solid propellant case, concentration of Al in the propellant was taken as 4% due to composition of in-house propellant and motor configuration was taken the same as that of non-aluminized case. ANSYS FLUENT without radiation was used to

predict plume profiles for aluminized propellant due to fact that CFD solver without radiation provides lower CPU times and it leads to similar plume field profiles for non-aluminized solid propellant case. It was found that  $\text{Al}_2\text{O}_3$  particle affects the plume flow field due to the fact that temperature at nozzle exit for aluminized case was taken as higher than that of non-aluminized case. This was followed by running the radiation code for aluminized solid propellant case. Comparison between spectral radiant intensity under non-aluminized and aluminized propellant reveals that presence of  $\text{Al}_2\text{O}_3$  particles in the plume increases the source spectral radiant intensity due to higher temperature profiles and radiative properties of particles for aluminized propellant case.

## 5.1 Future Works

For this study;

- Building experimental set up to measure particle size distribution and infrared signature
- Performing experiments in static firing.
- Validation of developed code by using measured data
- Testing developed code at flight conditions

will be the future work for more research.



## REFERENCES

- [1] Pautrizel, J.-B., Roblin, A., Perez, P., and Rialland, V., *Absorption-scattering Coupling for the Infrared Signature of an Aluminized Solid Rocket Motor*, Proceedings of the 6<sup>th</sup> International Symposium on Radiative Transfer, Antalya, Turkey, 13-19 June 2010.
- [2] Davenas, A., *Solid Rocket Propulsion Technology*, 1<sup>st</sup> Edition, Pergamon Press, England, 1993.
- [3] Sutton, G.P. and Biblarz, O., *Rocket Propulsion Elements*, 7<sup>th</sup> Edition, John Wiley & Sons, Canada, 2001.
- [4] Dennis, C.W., *A Study of Rocket Exhaust Particles*, PhD Thesis, Cranfield University, USA, 1996.
- [5] Kayakol, N., *Discrete Transfer and Discrete Ordinates Method for Radiative Heat Transfer in Furnaces*, Ph.D. Thesis, Middle East Technical University, Ankara, Turkey, 1998.
- [6] Selçuk, N., *Evaluation of Flux Models for Radiative Transfer in Rectangular Furnaces*, International Journal of Heat and Mass Transfer, 31, p. 1477-1482, 1988.
- [7] Selçuk, N., *Evaluation of Flux Models for Radiative Transfer in Cylindrical Furnaces*, International Journal of Heat and Mass Transfer, 32, p. 620-624, 1989.
- [8] Selçuk, N., *Evaluation of Spherical Harmonics Approximation for Radiative Transfer in Cylindrical Furnaces*, International Journal of Heat and Mass Transfer, 33, p. 579-581, 1990.
- [9] Modest, M.F., *Modified Differential Approximation for Radiative Transfer in General Three-Dimensional Media*, Journal of Thermophysics, 3, p. 283-288, 1989.

- [10] Modest, M.F., *The Improved Differential Approximation for Radiative Transfer in Multidimensional Media*, Journal of Heat Transfer, 112, p. 819-821, 1990.
- [11] Gerardin, J., Seiler, N., Ruyer, P., Trovalet, L. and Boulet, P.,  *$P_1$  Approximation, MDA and IDA for the Simulation of Radiative Transfer in 3D Geometry for an Absorbing Scattering Medium*, Journal of Quantitative Spectroscopy and Radiative Transfer, 113, p. 140-149, 2012.
- [12] Selçuk, N., and Kayakol, N., *Evaluation of Discrete Ordinates Method for Radiative Transfer in Rectangular Furnaces*, International Journal of Heat and Mass Transfer, 40, p. 213-222, 1997.
- [13] Selçuk, N. and Kayakol, N., *Evaluation of Angular Quadrature and Spatial Differencing Schemes for Discrete Ordinates Method in Rectangular Furnaces, Proceedings of 31<sup>st</sup> National Heat Transfer Conference*, ASME HDT-325(3), p. 151-158, Houston, Texas, 1996.
- [14] Truelove, J. S., *An Evaluation of The Discrete Ordinates Approximation for Radiative Transfer in an Absorbing, Emitting, and Scattering Planar Medium*, HTFS Report No.R8478, 1976.
- [15] Fiveland, W. A., *Discrete Ordinate Methods for Radiative Heat Transfer in Isotropically and Anisotropically Scattering Media*, Journal of Heat Transfer, 109, p. 809-812, 1987.
- [16] Fiveland, W. A., *Discrete-Ordinates Solutions of the Radiative Transport Equation for Rectangular Enclosures*, Journal of Heat Transfer, 106, p. 699-706, 1984.
- [17] Kim, T.-K., and Lee, H., *Effect of Anisotropic Scattering on Radiative Heat Transfer in Two-Dimensional Rectangular Enclosures*, International Journal of Heat and Mass Transfer, 31(8), p. 1711-1721, 1988.

- [18] Truelove, J. S., *Three-Dimensional Radiation in Absorbing-Emitting-Scattering Media Using the Discrete-Ordinates Approximation*, Journal of Quantitative Spectroscopy and Radiative Transfer, 39 (1), p. 27-31, 1988.
- [19] Coelho, P.J., *Numerical Simulation of Radiative Heat Transfer from Non-Gray Gases in Three-Dimensional Enclosures*, Journal of Quantitative Spectroscopy and Radiative Transfer, 74, p. 307-328, 2001.
- [20] Evans, K.F., *The Spherical Harmonics Discrete Ordinate Method for Three-Dimensional Atmospheric Radiative Transfer*, Journal of Atmospheric Science, 55, p. 429-446, 1998.
- [21] Evans, K.F., *SHDOMPPDA: A Radiative Transfer Model for Cloudy Sky Data Assimilation*, Journal of Atmospheric Science, 55, p. 3854-3864, 1998.
- [22] Selçuk, N., Kırbaş, G., and Tarhan T., *Evaluation of Method of Lines Solution of Discrete Ordinates Method and Finite Volume Method in a Planar Medium*, Proceeding of International Conference on Computational Heat and Mass Transfer, pp. 358-364, Gazimağusa, Northern Cyprus, 1999.
- [23] Denison, M.K., *A Spectral Line-Based Weighted-Sum-of-Gray-Gases Model for Arbitrary RTE Solvers*, Ph.D. Thesis, Brigham Young University, Provo, Utah, 1994.
- [24] Taine, J., "A Line-by-line calculations of low-resolution radiative properties of CO<sub>2</sub>-CO-transparent nonisothermal gases mixtures up to 3000 K", Journal of Quantitative Spectroscopy and Radiative Transfer, 30, 371-379, 1983.
- [25] Liu, F., Smallwood, G.J., and Gülder, Ö.L., *Application of Statistical Narrowband Model to Three-Dimensional Absorbing-Emitting-Scattering Media*, Journal of Thermophysics and Heat Transfer, 13 (3), p. 285-291, 1999.

- [26] Cai, G., Zhu, D. and Zhang, X., *Numerical Simulation of the Infrared Radiative Signatures of Liquid and Solid Rocket Plumes*, Aerospace Science and Technology, 11, p. 473-480, 2007.
- [27] Avital, G., Cohen, Y., Gamss L., Kanelbaum, Y., Macales, J., Trieman, B., Yaniv, S., Lev, M., Stricker, J., and Sternlieb, A., *Experimental and Computational Study of Infrared Emission From Underexpanded Rocket Exhaust Plumes*, Journal of Thermophysics and Heat Transfer, 15 (4), p. 377-383, 2001.
- [28] Boischot, A., Roblin, A., Hespel, L., Dubois, I., Prevot, P., and Smithson, T., *Evaluation of Computation Codes for Rocket Plume's Infrared Signature by Using Measurements on a Small Scale Aluminized Composite Propellant Motor*, Targets and Backgrounds XII: Characterization and Representation, Proceedings of SPIE, 6239, 62390M-1, 2006.
- [29] Nelson, H.F., *Influence of Particulates on Infrared Emission From Tactical Rocket Exhaust*, Journal of Spacecraft and Rockets, 21(5), p. 425-431, 1984.
- [30] Caliot, C., Flamant, G., El Hafi, M., and Le Maout, Y., *Assessment of the Single-Mixture Gas Assumption for the Correlated k-Distribution Fictitious Gas Method in H<sub>2</sub>O-CO<sub>2</sub>-CO Mixture at High Temperature*, Journal of Heat Transfer, 130, 104501, 2008.
- [31] Ludwig, C.B., Malkmus, W., Reardon, J.E., and Thomson, J.A.L., "Handbook of infrared radiation from combustion gases", NASA SP-3080, 1973.
- [32] Freeman, G.N., Ludwig, C.B., Malkmus, W., and Reed, R., *Development and Validation of Standardized Infrared Radiation Model (SIRRM)*, AFRPL-TR-79-55, 1979.
- [33] Farmer, R.C., Smith, S.D., and Myruski, B.L., *Radiation from Advances Solid Rocket Motor Plumes*, SECA-FR-94-18, SECA Inc., 1994.

- [34] Duval, R., Soufiani, A. and Taine, J., *Coupled Radiation and Turbulent Multiphase Flow in an Aluminised Solid Propellant Rocket Engine*, Proceedings of Eurotherm 73 on Computational Thermal Radiation in Participating Media, Mons, Belgium, 15-17 Nisan 2003.
- [35] Walters, D.V. and Buckius, R.O., *Normal Spectral Emission from Nonhomogenous Mixtures of CO<sub>2</sub> Gas and Al<sub>2</sub>O<sub>3</sub> Particulate*, Transactions of the ASME Journal of Heat Transfer, 113, p. 174-184, 1991.
- [36] Lyons, R.B., Wormhoudt J., and Gruninger J., *Scattering Radiation by Particles in Low-Altitude Plumes*, Journal of Spacecraft and Rockets, 20(2), p. 189-192, 1983.
- [37] Roblin, A., Baudoux, P.E. and Chervet, P., *UV Missile Plume Signature Model, Targets and Backgrounds XII: Characterization and Representation, Proceedings of SPIE*, 4718, p. 344-355, 2002.
- [38] Witson, M.E., *Handbook of the Infrared Optical Properties of Al<sub>2</sub>O<sub>3</sub>, Carbon, MgO And ZrO<sub>2</sub>*, Volume I, SAMSO-TR-75-131, 1975.
- [39] Ludwig, C.B., Malkmus, W., and Freeman, G.N., *A Theoretical Model for Absorbing, Emitting, and Scattering Plume Radiation*, Proceeding of AIAA 16<sup>th</sup> Thermophysics Conference, 81-1051, Palo Alto, California, 1981.
- [40] Dombrovsky, L.A., *Thermal Radiation of a Two-phase Exhaust Jet*, Thermopedia, 10.1615/thermopedia.000181, 2010.
- [41] Wang, W., Wei, Z., Zhang, Q., Wang, N., and Xiong, Y., *Infrared Radiation Signature of Exhaust Plume from Solid Propellants of Different Energy Characteristics*, Proceeding of AIAA/ASME/SAE/ASEE Joint Propulsion Conference and Exhibit, AIAA 2011-6140, San Diego, California, 31 July-03 August 2011.

- [42] Selçuk, N. and Kırbaş, G., *The Method of Lines Solution of the Discrete Ordinates Method for Radiative Heat Transfer in Enclosures*, Numerical Heat Transfer Part B-Fundamentals, 37, p. 379-392, 2000.
- [43] Ayrancı, I., *The Method of Lines Solution of Discrete Ordinates Method for Radiative Heat Transfer in 3D Rectangular Enclosures Containing Scattering Media*, M.Sc. Thesis, Middle East Technical University, Ankara, Turkey, 2001.
- [44] Modest, M.F., *Radiative Heat Transfer*, 2<sup>nd</sup> Ed., Academic Press, Massachusetts, 2003.
- [45] Schiesser, W.E., *The numerical method of lines in integration of partial differential equations*, 1<sup>st</sup> Ed., Academic Press Inc., p. 8-18, 2003.
- [46] Yucel, A., *Solution of the discrete ordinates equations for a radiatively participating medium by the method of lines*, In: Vichnevetsky R, Knight D, Richter G, Editors. Advances in Computer Methods for Partial Differential Equations VII, New Brunswick: IMACS, p. 834-844. , 1992.
- [47] Selçuk, N., Ayrancı, I. , Gogebakan, Y., *Effect of recycle on radiative heat transfer in the freeboard of a fluidized bed combustor*, Proc. of 18th International Conference on Fluidized Bed Combustion, ASME, FBC2005-78069, May 22-25, Toronto, Ontario, Canada, 2005.
- [48] Selçuk N., and Doner N., *A 3-D Radiation Model for Non-Grey Gases*, Journal Of Quantitative Spectroscopy And Radiative Transfer, 110, p. 184-191, 2009.
- [49] Doner, N., and Selçuk, N., *An Application Of Spectral Line-Based Weighted Sum of Grey Gases (SLW) Model With Geometric Optics Approximation For Radiative Heat Transfer In 3-D Participating Media*, Applied Thermal Engineering, 50, p. 89-93, 2013.
- [50] Marshak, R.E., *Note on the Spherical harmonics Method as Applied to the Milne Problem for a Sphere*, Physical Review, 71, p. 443-446, 1947.

- [51] Carlson, B.G. and Lathrop, K.D., *Transport Theory- the Method of Discrete Ordinates*, Computing Methods in Reactor Physics, ed. H. Greenspan, C.N. Kelber and D. Okrent, Gordon and Breach, New York, 1968.
- [52] El Wakil, N. and Sacadura, J. F., *Some Improvements of Discrete Ordinates Method for the Solution of the Radiative Transport Equation in Multi-Dimensional Anisotropically Scattering Media*, Developments in Radiative Heat Transfer, ASME HTD-Vol. 203, 119-127, 1992.
- [53] Fiveland, W. A., *The Selection of Discrete Ordinate Quadrature Sets for Anisotropic Scattering*, Fundamentals of Radiation Heat Transfer, ASME HTD-Vol. 160, 89-96, 1991.
- [54] Thurgood, C.P., Pollard, A., and Becker, H.A., *The  $T_N$  Quadrature Set for the Discrete Ordinates Method*, Journal of Heat Transfer, 117, p. 1068-1070, 1995.
- [55] FLUENT 6.2 User's Guide.
- [56] Leckner, B., *Spectral and total emissivity of water vapor and carbon dioxide*, Combustion and Flame, 19, p. 33-48, 1978.
- [57] Denison, M.K., Webb B.W., *A spectral line-based weighted-sum-of-grey-gases model for arbitrary RTE solvers*, ASME Journal of Heat Transfer 115, p. 1004-1012 , 1993.
- [58] Denison, M.K., Webb, B.W., *An absorption-line blackbody distribution function for efficient calculation of total gas radiative heat transfer*, Journal of Quantitative Spectroscopy and Radiative Transfer, 50, p. 499-510, 1993.
- [59] Rothman, L.S., Gamache, R.R., Tipping, R.H., Rinsland, C.P., Smith, M.A.H., Benner, D.C., Devi, V.M., Flaud, J.-M., Camy-Peyret, C., Perrin, A., Goldman, A., Massie, S.T., Brown, L.R., *The hitran molecular database: editions of 1991 and 1992a*, Journal of Quantitative Spectroscopy and Radiative Transfer, 48, p. 469-507, 1992.

- [60] Denison, M.K., Webb, B.W., *Development and application of an absorption line blackbody distribution function for CO<sub>2</sub>*, International Journal of Heat and Mass Transfer, 38, p. 1813-1821, 1995.
- [61] Denison, M.K., Webb, B.W., *The spectral line-based weighted sum of grey gases model for H<sub>2</sub>O/CO<sub>2</sub> mixtures*, ASME Journal of Heat Transfer, 117, p. 788-792, 1995.
- [62] Liu, F., Smallwood, G.J., and Gülder, Ö.L., *Application of the Statistical Narrow-band Correlated-k Method to Non-grey Gas radiation in CO<sub>2</sub>-H<sub>2</sub>O Mixtures: Approximate Treatments of Overlapping Bands*, Journal of Quantitative Spectroscopy and Radiative Transfer, 68, p. 401-417, 2001.
- [63] Soufiani, A. and Taine, J., *High Temperature Gas Radiative Property Parameters of Statistical Narrow-band Model for H<sub>2</sub>O, CO<sub>2</sub>, CO, and Correlated-k Model for H<sub>2</sub>O and CO<sub>2</sub>*, International Journal of Heat and Mass Transfer, 40, p. 987-991, 1997.
- [64] Riviere P. and Soufiani, A., *Updated Band Model Parameters for H<sub>2</sub>O, CO<sub>2</sub>, CH<sub>4</sub>, and CO Radiation at High Temperature*, International Journal of Heat and Mass Transfer, 55 (13-14), p. 3349-3358, 2012.
- [65] Lacis, A.A. and Oinas, V.A., *A Description of the Correlated k Distribution Method for Modeling Nongray Gaseous Absorption, Thermal Emission, and Multiple Scattering in Vertically Inhomogeneous Atmospheres*, Journal of Geophysical Research, 96, p. 9027-9063, 1991.
- [66] Bohren, C.F. and Huffman, D.R., *Absorption And Scattering Of Light By Small Particles*, 1<sup>st</sup> Ed., John Wiley & Sons Inc, USA, 1983.
- [67] Ozen G. and Selçuk N., *Performance Of DOM and IDA With Different Angular Discretization Methods in 3-D Absorbing- Emitting-Scattering Media*, International Journal of Thermal Science, 65, p. 104-110, 2013.



- [68] Tan, Z.-M. and Hsu, P.-F., *Transient Radiative Transfer in 3-D Homogeneous and Non-homogenous Participating Media*, Journal of Quantitative Spectroscopy and Radiative Transfer, 73, p. 181-194,2002.
- [69] Kim, S.H. and Huh, K.Y., *A New Angular Discretization Scheme of the Finite Volume Method for 3-D Radiative Heat Transfer in Absorbing, Emitting and Scattering Media*, International Journal of Heat and Mass Transfer, 43, p. 1233-1242, 2000.
- [70] Altaç, Z. and Tekkalmaz, M., *Exact Solution of Radiative Transfer Equation for Three-Dimensional Rectangular, Linearly Scattering Medium*, Journal of Thermophysics and Heat Transfer, 25, p. 228-238, 2011.
- [71] Ozen, G. and Selçuk N., *Sensitivity of Radiation Modeling to Property Estimation Techniques in the Dilute zone of Lignite-Fired Bubbling Fluidized Bed Combustors (BFBCs)*, Combustion Science and Technology 186, p. 684-697, 2014.
- [72] Selçuk, N., Gogebakan, Y., Harmandar, H., Altindag, H., *Effect of recycle on combustion and emission characteristics of high sulfur lignite*, Combustion. Science and Technology, 176 , p. 959-975, 2004.
- [73] Kozan, M. , Selçuk, N., *Investigation of radiative heat transfer in freeboard of a 0.3 MWt AFBC test rig*, Combustion. Science and Technology, 153, p. 113-126, 2000.
- [74] Harmandar, H., *Effect of Recycling on the Performance of Bubbling Fluidized Bed Combustors*, Master Thesis, Middle East Technical University, 2003.
- [75] Viskanta, R., Ungan, A., Mengüç, M. P., *Predictions of radiative properties of pulverized coal and fly-ash polydispersions*, ASME Paper, No.81-HT-24, 1981.
- [76] Selçuk, N., Batu, A. , Ayranci, I., *Performance of method of lines solution of discrete ordinates method in the freeboard of a bubbling fluidized bed combustor*, Journal of Quantitative Spectroscopy and Radiative Transfer, 73, p. 503-516, 2002.

- [77] Johansson R., Andersson K., Leckner B., and Thunman H., *Models for gaseous radiative heat transfer applied to oxy-fuel conditions in boilers*, International Journal of Heat and Mass Transfer, 53 , p. 220-230, 2010.
- [78] Smith, T. F. , Shen, Z. F. , and Friedman J. N., *Evaluation of Coefficients for The Weighted Sum Of Gray Gases Model*, ASME Journal of Heat Transfer, 104, p.602–608, 1982.E
- [79] Hjartstam, S., Johansson, R., Andersson, K., and Johnsson, F., *Computational Fluid Dynamics Modeling Of Oxy-Fuel Flames: The Role of Soot And Gas Radiation*, Energy Fuels, 26, p. 2786–2797,2012.
- [80] Stefanidis, G. D. , Van Geem, K. M. , Heynderickx, G. J. , and Marin G. B. , *Evaluation of High-Emissivity Coatings in Steam Cracking Furnaces Using A Non-Grey Gas Radiation Model*, Chemical Engineering Journal, 137, p. 411–421, 2008.
- [81] Yin, C., Johansen, L. C. R. , Rosendahl, L. A., and Kær, S. K., *New Weighted Sum of Gray Gases Model Applicable to Computational Fluid Dynamics (CFD) Modeling of Oxy-Fuel Combustion: Derivation, Validation, And Implementation*, Energy Fuels, 24, p. 6275–6282, 2010.
- [82] Yin, C., Rosendahl, L. A., and Kær, S. K., *Chemistry and Radiation in Oxy-Fuel Combustion: A Computational Fluid Dynamics Modeling Study*, Fuel, 90, p. 2519–2529, 2011.
- [83] Yin, C., *Nongray –Gas Effects In Modeling of Large-Scale Oxy-Fuel Combustion Processes*, Energy Fuels, 26, p. 3349–3356, 2012.
- [84] Nakod, P. , Krishnamoorthy, G., Sami, M., and Orsino, S., *A Comparative Evaluation of Gray and Non-Gray Radiation Modeling Strategies in Oxy-Coal Combustion Simulations*, Applied Thermal Sciences, 54, p. 422-432, 2013.

- [85] Porter, R., Liu, F., Pourkashanian, M., Williams, A., Smith, D., *Comparative Evaluation of Gray And Non-Gray Radiation Modeling Strategies in Oxy-Coal Combustion Simulations*, Journal of Quantitative Spectroscopy and Radiative Transfer, 111, p. 2084–2094, 2010.
- [86] Liu F., Numerical solutions of three-dimensional non-grey gas radiative transfer using the statistical narrow-band model, Transactions of ASME, 121, p.200–203, 1999.
- [87] Gordon, S., and McBride, B.J., *Computing Thermodynamic and Transport Properties*, NASA Technical Briefs, 17 (7), 1993.
- [88] Cousins, J.M., *Calculation of Conditions in an Axisymmetric Rocket Exhaust Plume: The REP3 Computer Program*, Propellants, Explosives, and Rocket Motor Establishment Technical Report No. 218, Defence Research Information Center, Station Square House, St. Mary Cray, Orpington, Kent, United Kingdom, BR5 3RE, 1982.
- [89] Uygur, A.B., *A Non-iterative Pressure Based Algorithm for the Computation of Reacting Radiating flows*, Ph.D. Thesis, Middle East Technical University, Ankara, Turkey, 2007.
- [90] Laredo, D., and Netzer, D.W., “*The Dominant Effect of Alumina on Nearfield Plume Radiation*”, Journal of Quantitative Spectroscopy and Radiative Transfer, 50(5), p. 511-530, 1993.



## APPENDIX A

### ORDINATES AND WEIGHTS FOR $S_N$ AND $T_N$ APPROXIMATIONS

In this study,  $S_N$  and  $T_N$  angular quadrature schemes were used. The ordinates and weights for various orders of  $S_N$  approximation are presented in Table A.1. The ordinates and weights for  $T_4$  quadrature set are presented in Table A.2.

Table A.1 Discrete ordinates for the  $S_N$  approximation for 3-D geometry

Order of Approximation	Ordinates			Weights
	$\mu_m$	$\zeta_m$	$\xi_m$	$w_m$
$S_2$	0.5000000	0.7071068	0.5000000	3.1415927
$S_4$	0.2958759	0.2958759	0.9082483	1.0471976
	0.2958759	0.9082483	0.2958759	1.0471976
	0.9082483	0.2958759	0.2958759	1.0471976
$S_6$	0.1838670	0.1838670	0.9656013	0.3219034
	0.1838670	0.6950514	0.6950514	0.7252938
	0.6950514	0.1838670	0.6950514	0.7252938
	0.1838670	0.9656013	0.1838670	0.3219034
	0.6950514	0.6950514	0.1838670	0.7252938
	0.9656013	0.1838670	0.1838670	0.3219034
$S_8$	0.1422555	0.1422555	0.9795543	0.3424718
	0.1422555	0.5773503	0.8040087	0.1984568
	0.5773503	0.1422555	0.8040087	0.1984568
	0.1422555	0.8040087	0.5773503	0.1984568
	0.5773503	0.5773503	0.5773503	0.9234358
	0.8040087	0.1422555	0.5773503	0.1984568
	0.1422555	0.9795543	0.1422555	0.3424718
	0.5773503	0.8040087	0.1422555	0.1984568
	0.8040087	0.5773503	0.1422555	0.1984568
	0.9795543	0.1422555	0.1422555	0.3424718
$S_{10}$	0.9809754	0.1372719	0.1372719	0.0944411
	0.8523177	0.1372719	0.5046889	0.148395
	0.8523177	0.5046889	0.1372719	0.148395
	0.7004129	0.1372719	0.7004129	0.0173701
	0.7004129	0.5046889	0.5046889	0.1149972
	0.7004129	0.7004129	0.1372719	0.0173701
	0.5046889	0.1372719	0.8523177	0.148395
	0.5046889	0.5046889	0.7004129	0.1149972
	0.5046889	0.7004129	0.5046889	0.1149972
	0.5046889	0.8523177	0.1372719	0.148395
	0.1372719	0.1372719	0.9809754	0.0944411
	0.1372719	0.5046889	0.8523177	0.148395
	0.1372719	0.7004129	0.7004129	0.0173701
	0.1372719	0.8523177	0.5046889	0.148395
0.1372719	0.9809754	0.1372719	0.0944411	

Table A.2 Discrete ordinates for the  $T_4$  approximation for 3-D geometry

Order of Approximation	Ordinates			Weights
	$\mu_m$	$\zeta_m$	$\xi_m$	$w_m$
$T_4$	0.5773503	0.5773503	0.5773503	0.1552105
	0.9901475	0.0990148	0.0990148	0.0526558
	0.0990148	0.0990148	0.9901475	0.0526558
	0.0990148	0.9901475	0.0990148	0.0526558
	0.9428090	0.2357022	0.2357022	0.0880364
	0.2357023	0.2357022	0.9428090	0.0880364
	0.2357023	0.9428090	0.2357022	0.0880364
	0.8616404	0.1230915	0.4923660	0.0995716
	0.8616404	0.4923660	0.1230915	0.0995716
	0.1230915	0.4923660	0.8616404	0.0995716
	0.4923660	0.1230915	0.8616404	0.0995716
	0.4923660	0.8616404	0.1230915	0.0995716
	0.1230915	0.8616404	0.4923660	0.0995716
	0.6804138	0.2721655	0.6804138	0.1320254
	0.2721655	0.6804138	0.6804138	0.1320254
	0.6804138	0.6804138	0.2721655	0.1320254





## CURRICULUM VITAE

### PERSONAL INFORMATION

**Surname, Name:** ÖZEN, Güzide

**Nationality:** Turkish (TC)

**Date and Place of Birth:** 15-04-1983, İzmit

**Marital Status:** Married

**Phone:** + 90 312 210 4395

### PERSONAL INFORMATION

Degree	Institution	Year of Graduation
M.Sc.	Chemical Engineering, METU	2008
B.Sc.	Chemical Engineering, METU	2006

### PUBLICATIONS

#### Journal Articles

1. **Ozen G.**, and Selçuk N. “Sensitivity of radiation modeling to property estimation techniques in the freeboard of lignite-fired bubbling fluidized bed combustors (BFBCs)”, *Combustion Science and Technology* ,Volume 186, Issue 4-5, Pages 684-697, 2014

2. **Ozen G.**, and Selçuk N. “Performance of DOM and IDA with different angular discretization methods in 3-D absorbing-emitting-scattering media”, International Journal of Thermal Sciences, Volume 65, Pages 104-110,2013.

### **Conference and Symposium Proceedings**

1. **Ozen G.**, Aydin F. and Selçuk N. “Radiative Heat Transfer in the Dilute Zone of An Air-Fired CFBC And Its Oxy-Fired Retrofit”, 9th Mediterranean Combustion Symposium, Rhodes, Greece, June 7-11, 2015.
2. **Ozen G.**, and Selçuk N. “Sensitivity of radiation modeling to property estimation techniques in the freeboard of lignite-fired BFBCs”, 8th Mediterranean Combustion Symposium, Çeşme, Turkey, September 8-13, 2013.
3. **Ozen G.**, and Selçuk N. “DOM and IDA T<sub>4</sub> for Radiative Transfer in 3-D Absorbing-Emitting-Scattering Media”, Eurotherm 95, Computational Thermal Radiation in Participating Media IV, Nancy, France, April 17-20, 2012.
4. **Aydin G.**, Kulah G. and Selçuk N. “Radiative-convective Model for One-dimensional Longwave Clear Sky Atmosphere” Eurotherm 83, Computational Thermal Radiation in Participating Media , Lisbon, Portugal, April 15-17, 2009.